

A NOVEL MESOSCALE MODELING OF FRACTURE IN NUCLEAR FUELS

A Dissertation

by

MOHAMMED GOMAA EID FARAG ABDOELATEF

Submitted to the Graduate and Professional School of
Texas A&M University
in partial fulfillment of the requirements for the degree of

DOCTOR OF PHILOSOPHY

Chair of Committee,	Karim Ahmed
Committee Members,	Raymundo Arróyave
	Ibrahim Karaman
	Lin Shao
	Pavel V. Tsvetkov
Head of Department,	Ibrahim Karaman

August 2022

Major Subject: Materials Science and Engineering

Copyright 2022 Mohammed Abdoelatef

ABSTRACT

Nuclear fuels power all the commercial carbon-free energy plants and contribute to the fight against climate change. A comprehensive understanding of the fracture behavior of nuclear fuels during normal and transient conditions is still lacking. In this work, we developed a novel Multiphysics mesoscale model that could predict the fracture in different nuclear fuels under various conditions by employing the phase-field modeling of fracture. This work introduces both (1) An experimental study to understand the fuel fracturing behavior of sintered UO_2 pellets when exposed to thermal shock, and (2) A Multiphysics phase-field fracture model capable of simulating this process. The model could successfully capture the formation and evolution of cracks in UO_2 fuel pellets due to a thermal shock without any ad hoc or a priori assumptions of cracking size, site, thickness, or morphologies. The model was able to capture the overall fracture trends of the corresponding experimental data. Moreover, the model further improved and utilized multi-set order parameters that allowed the simulation of the concurrent crack propagation and microstructure evolution. The new model technique is then validated and employed in an evolved nuclear-grade graphite microstructure to determine the effect of such heterogeneity on the formation and propagation of the cracks along with the variations in the materials' mechanical properties. This new technique advances the fundamental understanding of nuclear fuel behavior under normal and transient conditions and provides a predictive modeling tool for deriving physics-based criteria for the fracture behavior of the current and the new nuclear fuel designs.

ACKNOWLEDGEMENTS

I would like to thank my committee chair, Prof. Karim Ahmed, and my committee members, Prof. Raymundo Arróyave, Prof. Ibrahim Karaman, Prof. Lin Shao, and Prof. Pavel V. Tsvetkov for their guidance and support throughout the course of this research.

Thanks also go to my friends, colleagues and the department faculty and staff for making my time at Texas A&M University a great experience. Finally, thanks to my parents and siblings for their encouragement and to my wife, Taghred Essa and children (Khaled, Lareen, and Murad) for their patience and love.

CONTRIBUTORS AND FUNDING SOURCES

Contributors

This work was supervised by a dissertation committee consisting of Professor Karim Ahmed (advisor) and Professors Raymundo Arróyave, and Ibrahim Karaman of the Department of Materials Science and Engineering, Texas A&M University, and Professors Lin Shao, and Pavel V. Tsvetkov of the Department of Nuclear Engineering, Texas A&M University.

Funding Sources

The authors for this work would like to acknowledge the support from the U.S. Department of Energy NEUP program under award agency numbers DE-NE0009134 at Texas A&M University and DE-NE-0008979 at Texas A&M University through a subcontract from the University of Wisconsin- Madison (0000001085). Portions of this research made use of Idaho National Laboratory computing resources which are supported by the Office of Nuclear Energy of the U.S. Department of Energy and the Nuclear Science User Facilities under Contract no. DE-AC07-05ID14517.

NOMENCLATURE

UO ₂	Uranium dioxide
TRISO	TRi-structural ISotropic particle fuel.
HBS	High Burn-up Structure
NPPs	Nuclear Power Plants
LEFM	Linear Elastic Fracture Mechanics
EPFM	Elasto-Plastic Fracture Mechanics
LWRs	Light Water Reactors
PKA	Primary Knock-on Atom
DPA	Displacement Per Atom
LWRs	Light Water Reactors
AGR	Advanced Gas Reactor
SENT	Single-Edge Notch Tensile
RVE	Representative Elementary Volume
INL	Idaho National Laboratory
FCML	Texas A&M University's Fuel Cycle and Materials Laboratory
DEM	Discrete Element Method
CZM	Cohesive Zone Method
X-FEM	Extended Finite Element Method

TABLE OF CONTENTS

	Page
ABSTRACT	ii
ACKNOWLEDGEMENTS	iii
CONTRIBUTORS AND FUNDING SOURCES.....	iv
NOMENCLATURE	v
TABLE OF CONTENTS	vi
LIST OF FIGURES.....	viii
LIST OF TABLES	xiv
CHAPTER I INTRODUCTION	1
1.1 Motivation and Objectives.....	1
1.2 Contribution to Research	6
1.3 This work Layout.....	8
CHAPTER II TECHNICAL BACKGROUND.....	9
2.1 Phase Field Modeling of Fracture.....	12
2.1.1 The phase-field modeling of fracture governing equations	12
2.1.2 The equilibrium profile in One-Dimensional analysis.....	14
2.1.3 Critical stress and strain analysis in One-Dimensional solution.....	16
2.1.4 Allen–Cahn-type evolution equations to a phase field model of fracture.....	22
2.2 Thermal Fracture in sintered UO ₂ Pellets	26
2.3 The Experimental work of thermal shocks induced fracture in UO ₂	29
2.3.1 Experimental methods.....	31
2.3.2 Experimental procedure	33
2.4 Fracture heterogeneity in TRISO Buffer layer	36
CHAPTER III PHASE FIELD MODEL DEVELOPMENT.....	44
3.1 Phase-Field modeling of fracture due to thermal shock in UO ₂	47
3.2 A novel formulation of phase-field modeling to simulate the co-formation of fracture and heterogenous microstructure evolutions.	52

3.2.1 The Novel Model’s evolution equations	58
CHAPTER IV RESULTS AND DISCUSSION.....	60
4.1 Benchmarking Test Cases.....	62
4.1.1 An elliptical cavity in an infinite domain.....	62
4.1.2 An elliptical cavity in a finite domain.....	64
4.1.3 Model validation based on Nuclear-grade graphite material parameters	67
4.2 Experimentally validated Multiphysics modeling of fracture induced by thermal shocks in Sintered UO ₂ Pellets	69
4.2.1 Thermal shocking experimental results of UO ₂ Sintered fuel Pellet	69
4.2.2 Model results, validations, and discussion.....	71
4.3 Evaluation of fracture behaviors in porous materials: One-particle analysis.	83
4.3.1 Effect of porosity shapes and volume fractions on stress distributions.	83
4.3.2 Effect of porosity shapes and volume fractions on fracture behaviors.	86
4.4 Multi-set Order parameter Novel Phase-field modeling of Fracture: Two- particles-system assessments.	87
4.4.1 Static two-particles analysis.....	87
4.4.2 Simulating the concurrent formation of cracks and microstructure evolution	90
4.5 Evaluation of fracture behaviors in porous materials: Multi-particles case	93
CHAPTER V CONCLUSIONS	96
5.1 Future Directions	98
CHAPTER VI WORKS CITED.....	99

LIST OF FIGURES

	Page
Figure 1 Schematics illustrate the spatial-temporal scales of the Irradiation damage process, where the radiation knock-on atoms (a) lead to a range of defects (b-c). The point defects (d) relax into local defect structures (e). These local defects act as preferable nucleation sites for voids (f-g). Eventually, the evolving and clustering of these voids ends up by a macroscopic swelling in the material component (h) [13].....	2
Figure 2 An influence of a crack.....	10
Figure 3 Schematic illustrations of the elliptical crack-tip curvature, ρ	10
Figure 4 Schematic illustration of irradiation damage [50].....	11
Figure 5 An illustration of the Irradiation-Induced Embrittlement process in Ferritic Steels, Reactor Pressure vessel (PV). The figure shows the ductile-to-brittle transition temperature (DBTT) and the Upper Shelf Energy (USE) reduction [51].	11
Figure 6 An illustration of the crack profile solution in 1-D case that shows the influences of the characteristic length scale parameters l_0 on the smeared crack region.	15
Figure 7 One dimensional homogenous Stress-Strain Curve for different length scale (l_0) while the geometric function and the degradation functions are $\alpha\eta d = \eta d^2$ & $g\eta d = (1 - \eta d)^2$, respectively.	19
Figure 8 One dimensional homogenous behavior of order parameter ηd vs. strain for different length scale (l_0) while the geometric function and the degradation functions are $\alpha\eta d = \eta d^2$ & $g\eta d = (1 - \eta d)^2$, respectively.	19
Figure 9 A 1-D homogeneous solution to investigate the phase-field order parameter Vs. Strain (left) and stress-strain curves (right). In this investigation, we illustrate the difference in implementing the crack density as quadratic function vs. quadratic and cubic degradation functions. Here, we implemented the characteristic length scale with a constant value ($l_0= 0.25$). The cubic degradation function is associated with higher homogenous stress, decreasing the computational cost due to the flexibility of selecting higher l_0	21
Figure 10 Generalized crack profile in 1D, β is constant [53].	24

Figure 11 Plot of variation in hoop stress in fresh LWR fuel as a function of radial position during ramping to full power [19] [57].	27
Figure 12 Plot of expected temperature profile during quenching after achieving a spatially uniform high temperature in the pellet [19] [57].	30
Figure 13 the pellets were cut into three parts which included two axial cuts and one radial cut to observe the fracture occurring in the samples. Note that shaded in blue is the contact area introduced to the cold bath (1/6 of the total pellet surface area). (For interpretation of the references to color in this figure legend, the reader is referred to the web version of this article.) [19].	31
Figure 14 (left) Insertion of insulation and pellet U6-71B attached to the thermo- couple into the capsule. (right) Solidworks rendering of the placement of the pellet in the capsule [19].	32
Figure 15 (a) Temperature readings of thermocouples from a pellet submersion experiment of a UO_2 pellet. Note that, the step changes seen in the plot are due to malfunction of thermocouples in the salt bath at the presented temperature. After reaching the appropriate temperature the sample was then quenched into the cold bath, hence the sudden and smooth drop. (b) Hirox image of a successfully cracked UO_2 pellet [19].	33
Figure 16 An illustration of the TRISO-layers that are coating the fuel kernel [59].	36
Figure 17 Micrographs images of TRISO particle. The left side shows the cracked particle, while the right side shows a zoom-in cross-sectional of the TRISO layers [59].	37
Figure 18 The frequent occurrence of fracture in buffer layers for UCO and UO_2 -based fuel as reported by the AGR-2 [22].	39
Figure 19 Color-coded events of buffer fracture occurred in (a) UCO-based and (b) UO_2 -based TRISO particle as reported in AGR-2 [22].	40
Figure 20 University of Wisconsin TRISO Particles SEM analysis: a) hexagonal array of polished TRISO particles, b) Slice and View of TRISO particle, with various investigated regions denoted by I, II, III, and IV.	41
Figure 21 University of Wisconsin image processing and data analysis: a) distribution of pore sizes resulting from intensity-based segmentation and deep learning segmentation methods, b) volume fractions of pore volume ranges resulting from the two segmentation methods, c) example of intensity-based segmentation result (pores – green, buffer – purple), d) unsegmented SEM image, e) example of deep learning segmentation result.	41

Figure 22 The Phase-field damage variable (c) spatial distribution in 1D	50
Figure 23 Schematic illustration of this work phase-field approach for modeling nuclear fuel pellet cracking. $\eta d = 1$ indicating fully damaged state and $\eta d = 0$ intact state.....	53
Figure 24 An illustration of the novel phase-field variables used to describe the fracture microstructure. For left and right screenshots, the second phase particle is shown in red, the intact matrix in blue, while the crack or the damaged regions are presented in white. The middle screenshot shows the stress distributions on the loading direction (Y-axis); note that the red color is the high-stress regions while the blue refers to the less-stress areas (in middle screenshot). ..	54
Figure 25 Elliptical hole in 2D infinite solid under tension. Point A is representing the maximum stress at the crack tip [94].....	62
Figure 26 The model expectation well agreed with the stress concentration factor (K_I) calculation as expected by Inglis [4].	63
Figure 27 A schematic illustration of the stress concentration builds up (and effect) near the crack tip in the case of (a) infinite plate and (b) finite plate [94].....	64
Figure 28 The analytical solution of the finite plate boundaries affects the stress near the crack tip, as shown in Eq 4.2, mainly the Secant term. Note that Eq. 2.46 [94] seen in this Figure is the Eq. 4.2 seen in text.....	65
Figure 29 The model simulations well aggregated with the analytical solutions presented in Eq 4.2, particularly the Secant term with a bit deviation from $a/w \sim 0.6$. But the behavior trend remained similar. The figure also shows how the stress is highly concentrated at the crack tip.	66
Figure 30 Specimen geometry and boundary conditions along with the model parameters for the SENT test [23].....	67
Figure 31 Brittle fracture propagation of Mode I in a single-edge notch tensile case using the phase-field fracture model. The left column is the work by P. Chakraborty et al., [23]., while the right column is this work simulation. (a&b) stress-strain along loading direction, (c&d) final configuration colored by the damage order parameter.	68
Figure 32 The experimental snapshots of various specimens' microstructures reveal various porosity (number density and sizes) distributions. Some porosities have a few micrometers size, or even less, while bigger ones take ellipsoidal shapes. These larger pores have a size of several tens of micrometers [19]. ...	70

- Figure 33 Experimental snapshots of various microstructures reveal various porosity (number density and sizes) distributions as well as subsequent fracture of the pellet. Some porosities are a few micrometers in size or even less, while bigger ones take ellipsoidal shapes. These larger pores have a size of several tens of micrometers. [19]..... 71
- Figure 34 The temperature evolution of the pellet outer surface and inner center points. Note that the counter timer in the experiment plot starts after the preheating process at approximately 430 s. The snapshots in the simulation plot show the temperature distribution (colored mapped from $-10\text{ }^{\circ}\text{C}$, dark blue to $750\text{ }^{\circ}\text{C}$ dark red) at the initial and mid-time steps. The agreement of the temperature distribution and evolution between the model and the experiment results verified the basic model parameter selection [19]. 73
- Figure 35 Snapshots of selected test cases simulations present the effect of different G_c and different contact areas on the formation and evolutions of the cracks induced by thermal shock in UO_2 fuel pellets. The first two rows show the cracks behaviors based on $G_c = 10\text{ MPa}\cdot\text{mm}$ and the last two rows at $G_c = 30\text{ MPa}\cdot\text{mm}$. The first and third rows are simply a single line contact area, while the second and fourth ones are established on a wider contact area, almost $1/6$ of the actual experiment contact area [19]. 76
- Figure 36 Snapshots of selected test cases simulations manifest the effect of G_c values, with the case of actual contact area, on the formation and evolutions of the cracks induced by thermal shock in UO_2 fuel pellet. The damage shape evolutions with $G_c = 10\text{ MPa}\cdot\text{mm}$ was seen in the first row. While the elected evolution with $G_c = 80\text{ MPa}\cdot\text{mm}$, which was found to be well-matched with the experimental results, is presented in the last row. The second and third rows show the simulations with $G_c = 30\text{ MPa}\cdot\text{mm}$ and $G_c = 50\text{ MPa}\cdot\text{mm}$, respectively [19]. 77
- Figure 37 Comparison of final crack patterns induced by thermal shock between this work experiment observations after the thermal shock testing (upper), and (lower) the elected model simulation (colored by the fractured order parameter field distribution). The model could capture the formation and evolution of primary radial cracks. As seen, there are two major (longer) radial cracks that formed immediately on the pellet circumferential boundary after the instantaneous drop in the outer temperature (thermal shock). Moreover, the simulated crack thickness was found to be similar to the experimental observation, as seen in left column. Minor differences between the model and the experiment results were noticed (such as the middle crack shown in the model simulations). These differences can be attributed to the absence of accounting for the effect of underlying microstructure (e.g., size

and morphology of pores and grains) in the current model; overcoming such limitations would be the focus of future studies [19]. 79

Figure 38 Snapshots illustrate the stresses formation and evolution before and after the cracks initiation and propagation for (upper) hoop stresses (lower) radial stress—the evaluation forms from left to right. The left column represents the stresses formation right after the instantaneous drop in temperature, while the right column shows the stresses evolution at the mid of the simulation time [19]. 80

Figure 39 Evolution of elastic strain energy and the formation and growth of the local fracture energy based on fine mesh and length scale parameter of 10^{-3} mm for the elected simulation case; see Figure 37. The elastic strain energy increases with increasing the temperature difference between the inner center and the outer surface (see Figure 34). The cracks immediately initiated on the pellet outer surface at about 10^{-2} s, right after the instantaneous drop in temperature. The elastic strain energy rate decreases with generating new fracture faces [19]. 81

Figure 40 An illustration of the good agreement results while comparing the model-new formation (MOOSE-mesh) with the classical phase-field fracture models [28] [29] that use external meshes with pre-defined holes (Gmesh) at different volume fractions (different Rs). The deviations started to be noticed with a $\sim +80\%$ volume fraction which is acceptable in all of our cases of studies. 84

Figure 41 Snapshots illustrate the studies void shapes, ηp (see first row) and the cracking shape (see second row). Note that the damage order parameter (ηd) is mapped by red color. Note that the applied load is in YY-direction. This Figure’s snapshots only show a certain volume fraction (30%) but this study investigates various volume fraction, see Figures 42 & 43. 85

Figure 42 An illustration of the single-particle shape and orientation effect on the stresses building up in a nuclear-grade graphite system. The Figure shows how the vertical ellipse shape (parallel to the applied load direction, stress_{yy}) could withstand better. All the particle shapes related to maximum stress degrade with volume fraction increases. 85

Figure 43 An illustration of the single-particle shape and orientation effect on the cracking behavior in a nuclear-grade graphite system. The Figure shows how the vertical ellipse shape (parallel to the applied load direction, stress_{yy}) could withstand better. Increasing the volume fraction will lead to faster cracks for all the shapes. 86

Figure 44 Snapshots of a two-particles (voids) nuclear-grade graphite system show how the stress builds up on the voids' inner and outer boundaries when they get closer in distance.	88
Figure 45 Snapshots of a two-particles (voids) nuclear-grade graphite system show how the stress builds up on the voids' inner and outer boundaries when they get touched (coalescence).....	89
Figure 46 Two voids coalescence and the stresses building up concurrently, watch the evolutions from left to right.....	90
Figure 47 Snapshots illustrate the model's capabilities in capturing the preferable cracking nucleation sites without any ad hoc and the stress distribution concurrently with the voids coalescence.	91
Figure 48 The stress-strain response under uniaxial loading with a magnified snapshot at the onset of unloading (i.e., cracking) points.	92
Figure 49 A typical representative volume element along with the utilized model parameter to simulate the H-451, nuclear-grade graphite [23].	93
Figure 50 work by P. Chakraborty et al., [23] . The left side is the damaged configurations while the right side is the stress-strain response under uniaxial loading of the representative volume element.....	94
Figure 51 Snapshots of the cracking initiation and evolutions in a porosity microstructure similar to the INL investigated case [23], see Figure 50. Once a crack starts, the Damage intensification remains confined within the damage regions resulting in an observed recovery in strength values as seen in the zoomed-in part of the stress-strain curve. Then the stress dropped sharply once the microstructure fully cracked, see the last snapshot on the right.	95

LIST OF TABLES

	Page
Table 1 Various combinations of geometric crack functions $\alpha\eta d$ and energetic degradation functions $g\eta d$ along with the corresponding critical stress σ_c and strains ϵ_c [52].	20
Table 2 The submersion times and temperatures of each experiment [19].	34
Table 3 Sintering profiles and associated calculated densities for various experiments [19].	34
Table 4 The data used to define the model required parameter for this work simulations [19].	73
Table 5 Detailed description of simulation test case script for the results provided in this section. 45 total simulations were run according to obtain the well-match G_c [19].	75
Table 6 The nuclear-grade graphite materials' properties similar to [23].	84

CHAPTER I

INTRODUCTION

1.1 Motivation and Objectives

Life and modern technology improve with better utilization of materials. The industrial revolution in the nineteenth century resulted in an enormous engineering application to facilitate the human life. In history, several catastrophic accidents due to a material fracture took place [1, 2], which caused significant losses in life and property. Investigating these failure phenomena led to the development of Fracture Mechanics as a new branch of science [3]. The successful design of any engineering structure that operates in harsh environments for a long time (such as Nuclear Fuels) requires understanding different modes of failure and degradation mechanisms. The modeling endeavors to understand the fundamentals of fracture behaviors started nearly 100-years ago when Inglis (1913) [4] studied the elliptical holes in a tension strip; this study shed light on the severity of a crack in a structure. Griffith in 1920 [5] investigated the propagation of cracks in glass and developed the most acceptable model for crack growth driven by lowering the system total energy. Griffith's work did not predict the failure load given only the crack growth. Thus, Irwin in 1948 [6] extended Griffith's work to the ductile high strength materials; this gave birth to the field of Linear Elastic Fracture Mechanics (LEFM) [7]. Irwin's model focused more on the crack tip instead of the crack itself. Combining Griffith and Irwin's work, the LEFM introduced the most fundamental parameters in the fracture mechanics field such as the Stress Intensity Factor (SIF) [8] and the Energy Release Rate (G_c) [9]. For other materials that behave non-linearly, LEFM fails, and the Elasto-Plastic

Fracture Mechanics (EPFM) [10] works better by accounting for the plastic deformation near to the crack-tip.

It is very complicated to model the fracture behavior in engineering materials [11, 12]. Still, the situation is much worse with irradiation damage, particularly while studying the fracture in nuclear fuels as recently demonstrated by L.D. McClenny, M.I. Butt, M.G. Abdoelatef et al. [12]. To perform such analyses, it requires understanding all the interactions from the single atom on the femtosecond scale up to the engineering scale, where things evolved over the years or even decades. A simple representation of the entire multi-scale picture of radiation damage is illustrated in Figure 1 [13], highlighting the mesoscale simulation (MSS) range, which is the scale of interest in this work contribution.

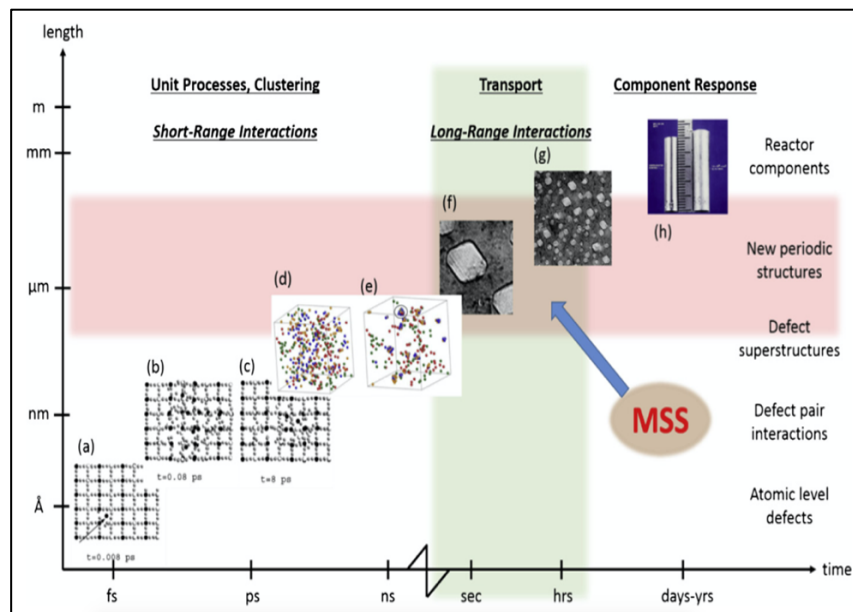


Figure 1 Schematics illustrate the spatial-temporal scales of the irradiation damage process, where the radiation knock-on atoms (a) lead to a range of defects (b-c). The point defects (d) relax into local defect structures (e). These local defects act as preferable nucleation sites for voids (f-g). Eventually, the evolving and clustering of these voids ends up by a macroscopic swelling in the material component (h) [13]

This work developed a Novel Multiphysics Mesoscale model that could predict the fracture in nuclear fuel by utilizing the phase-field approach [14 – 16], particularly the phase-field modeling of fracture . Understanding the fracture behavior in nuclear fuels would expanding the utilization of the current fleet of Nuclear Power Plants (NPPs) and enhancing the new Advanced Gas Reactor (AGR) technology. Thus, ensuring the sustain of the largest source of carbon-free electricity production (i.e., nuclear power) in the United States and world widely [17, 18]. UO₂ Fuel fracturing impacts the associated thermo-mechanical properties during normal and transient operation. Since UO₂ has a very low thermal conductivity, a large thermal gradient can build up (Soret effect) with a mass gradient leading to the initiation of pores. In as fabricated unirradiated LWR fuel, volumetric heating from fission is mostly spatially uniform (except on the pellet periphery). As burnup increases, self-shielding effects result in higher volumetric heat generation around the perimeter of the fuel pellets [12]. The heat is transferred radially outward from the fuel pellet, across the fuel-cladding gap, through the cladding, and finally into the coolant where it converts aqueous water into gaseous steam.

In this work, a coupled experimental and computational approach was utilized to investigate thermal fracture in UO₂. First, to induce fracture in UO₂ pellets, the pellets were submerged in molten salts and heated to a temperature in the range of (589– 676 °C). Then these pellets were subjected to a rapid temperature decrease to mimic accidents-like transients. Second, the computational model was used to simulate, reproduce, and interpret the experimental data. The UO₂ pellets used for this study were manufactured at Texas A&M University’s Fuel Cycle and Materials Laboratory (FCML) using powder

metallurgical methods and sintering to produce cylindrical UO_2 fuel pellets of approximately 9–10 mm in height and 10–11 mm diameter each. Fuel pellets of varying density, diameter, and heights were used in the thermal shocking experiments. The model could successfully capture the formation and evolution of cracks in UO_2 fuel pellets due to a thermal shock without any ad hoc or a priori assumptions of cracking size, site, thickness, or morphologies [19]. This work demonstrates that joint experimental and computational efforts are able to advance the understanding of thermal fracture in the primary fuel source for existing and future NPPs.

In the same manner, the improvements of the newly advanced nuclear reactors is fully depending on better utilization of TRISO fuel that is performing well but usually fail due to the stochastic tearing behavior in the buffer layer [20 – 22]. This work introduces a novel phase-field modeling formulations that established the correlation between the TRISO buffer layer (~ implementing nuclear-grade graphite parameters) porosity (number density, shape, sizes, volume fraction, and distribution) and the fracture strength. The model's new formations were benchmarked against several test cases and demonstrated well agreements. The current enhancements in our model define the porosity as a phase-field variable and represented the fracture with other phase-field order-parameter for the first time in this field. Moreover, the model further improved and utilized multi-set order parameters that allowed the simulation of the concurrent crack propagation and microstructure evolution. The model is then employed in an evolved nuclear-grade graphite microstructure to determine the effect of such heterogeneity on the formation and propagation of the cracks along with the variations in the materials' mechanical properties.

The model then shows the right outcomes compared to the Idaho National Laboratory (INL) previous work [23]. This is a significant improvement compared to the other models in literature that usually use an external mesh with a pre-defined porosity. This would reveal the mystery behind the interactions between the pores, grain boundaries and the cracks that are yet to be understood [24, 25 – 27].

Here, we utilized the phase-field modeling approach [14 – 16] to model the fracture [24, 28 – 29] behavior in nuclear fuels. Although, in literature, there are several valuable techniques to capture different fracture behaviors numerically. Some of these successful methods are the discrete element method (DEM), the extended finite element method (X-FEM) [30, 31], and the cohesive zone method (CZM) [32, 33]. Nevertheless, these methods are usually associated with a high computational cost and the cracking interfaces are not directly simulated. In X-FEM, the cracks are typically defined as discrete discontinuities that ease the brittle fracture simulations in polycrystalline material [34]. While the CZM approach applies a traction-separation method that indicates various fracture behaviors [35, 36]. Both methods (i.e., X-FEM and CZM) struggle to track the complex fracture evolutions. Moreover, the CZM shows mesh-dependent issues since the crack's representations are usually limited to the boundaries of the elements [24]. In comparison, the phase-field fracture modeling uses a length scale parameter that is assigned to control the damage band while the discrete fracture surfaces are represented through a diffused damage field. This intelligent method successfully simulates the complicated crack patterns and topologies such as branching and coalescence [37 – 40]. Moreover, the phase-field modeling of fracture can explicitly track the initiations of the

cracks' interfaces through the evolution of the phase-field order parameter (i.e., the damage variable) by minimizing the total energy of the system that is composed of elastic and fracture energies. This approach was first applied in the late of 1990s by Francfort [41] and Bourdin [42]. Recently, it has been employed to investigate various fracture behaviors in brittle [38, 40, 43] and nuclear materials [23]. In the last few years, it was employed to investigate fracture behaviors in UO_2 , as well [19, 21].

1.2 Contribution to Research

Compared with other phase-field fracture models, our Multiphysics model formulation was validated against experimental measurements and showed well agreements as discussed in [19]. In comparison with other studies which thoroughly investigated the fracture, our model was able to predict the cracks' initiation rate, size, shape, thickness, and morphology in addition to the spatial stresses formations, distributions, and evolutions throughout the whole system domain. These generalization capabilities in our model relax many assumptions employed by other models in the literature. The energy release rate, \mathcal{G}_c (or equivalently fracture toughness) is microstructure- and size-dependent, and its value is unknown for UO_2 and other nuclear fuels. Its value is difficult to estimate both from experiments and first-principles simulations. Lower-scale, first-principles simulations are limited to small sizes and cannot evaluate the actual value for a realistic microstructure. Even experimental studies cannot extract this number directly. They usually utilize either finite-element simulations or employ a few limiting analytical expressions from the linear elastic fracture mechanics to derive this value from their data [44, 45]. Here, a set of \mathcal{G}_c and contract area (the part of

the fuel pellet in direct contact with the cold bath) were able to capture the overall fracture trend of the corresponding experimental data. In fact, we believe that the phase-field fracture employed here presents a new method for calculating the energy release rate \mathcal{G}_c /fracture toughness.

Furthermore, for the first time, we employed a multi-set order parameters to describe the concurrent crack formation and propagation along with microstructure evolution including second phase particles formation and evolution (e.g., coalescence). The verified model was first applied to study the stress distribution around voids boundaries in a static two-particle domain, then applied to a heterogeneous nuclear-grade graphite system to determine the effect of void coalescence on the fracture behaviors that changes the effective toughness of the materials; hence influences the mechanical properties. This is a considerable improvement compared with other models found in literature, which usually utilize an external mesh with a pre-defined porosity/hole. Our new technique allows studying microstructure evolutions and their influences on fracture behavior. This would reveal the mystery behind the interaction between the underlying microstructure, second phase particles, and cracks that are yet to be understood [24 – 27].

These novel combinations would simulate the hypothetical behavior of fracture due to the irradiations (i.e., embrittlement effect) where the gaps/cracks might nucleate at the surface of the pores and then join the pores themselves or propagating along the grain boundaries or might be hindered [46, 47]. Of course, it is impossible to simulate such complicated phenomena with the current approaches in literature because all of their mechanics-based methods use a pre-defined porous mesh, where the porosity will never

evolve. Our novel model, tightly coupled cracking with porosity, allows the near-real physics simulations for the first time in the field.

1.3 This work Layout

First, the technical background of nuclear fuel fracture and the experiment method and procedure of the thermal shock induced fracture in the UO_2 are reviewed in Chapter II. This work model formulations were summarized in Chapter III. The validated model results to simulate the fracture in both UO_2 and the Nuclear-grade graphite were presented in Chapter IV in which the test cases for benchmarking the model were conducted first. Lastly, the main work findings were summarized in Chapter V along with the future direction's discussions.

CHAPTER II

TECHNICAL BACKGROUND

The strength of the materials approach does not anticipate the presence of a crack that can significantly decrease the structural strength and reliability. With the existence of a flaw size (a), the Fracture Toughness replaces the strength of materials, see Figure 2. For Linear-Elastic Fracture Mechanics (LEFM), the fracture toughness (K_{IC}) of material is determined from the Stress Intensity Factor (SIF, K_I), while the J-integral (energy required to grow a crack) determines the fracture toughness for the Elastic-Plastic Fracture cases. For a structure that contains a crack into it (see figure 3), the fracture mechanics is about understanding how/when the crack becomes critical to transfer the structure from being stable to unstable and it turns out that we can use the below equation to describe the system [7, 11, 48].

$$K_I = Y\sigma\sqrt{\pi a} \quad \text{Eq 2.1}$$

Where K_I is the SIF, note that K_{IC} is the critical SIF or the fracture toughness (a material's property), the specific value of the SIF when the crack became unstable, the letter “I” stands for “mode I” of failure, opening mode. Also, in Eq 2.1, “ a ”, is the crack size, σ is the stress (depends on the design or the application), and Y is a geometric function of the sample size and the size of the crack.

Cracks might form or initiate on the sample surface (see figure 2) or inside (see figure 3). The crack-tip curvature (ρ) is determining the max stress at the crack-tip and hence the crack propagations, this is illustrated in Figure 3 and Eq 2.2 in which the K_t is the stress concentration factor at the crack-tip.

$$K_t = \frac{\sigma_{max}}{\sigma_0} \approx 2 \sqrt{\frac{a}{\rho}} \quad \text{Eq 2.2}$$

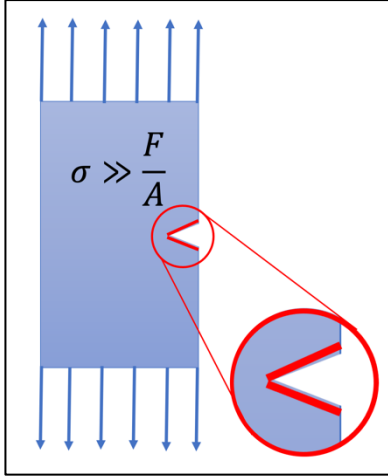


Figure 2 An influence of a crack.

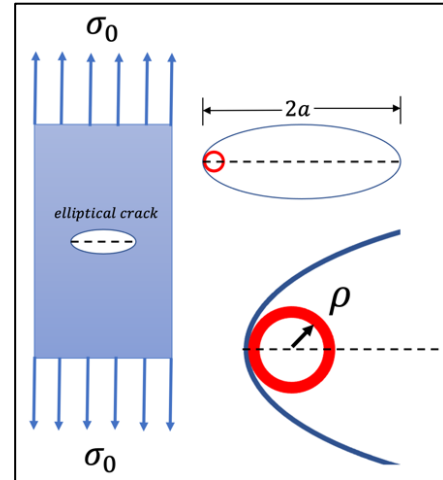


Figure 3 Schematic illustrations of the elliptical crack-tip curvature, ρ .

With irradiation, the fracture behavior becomes much more complicated. The primary mechanism of irradiation damage [49] is illustrated schematically in Figure 4 [50], in which the green particle represents a neutron or any heavy-ion that is of high enough energy to cause atomic displacement. The very first event where this particle (green particle in figure 4) strikes the perfect crystal (the array of white circles in Figure 4) is called the “primary knock-on atom” or PKA then that particle and the release PKA hit more and more atoms resulting in what is so-called a “Damaged Cascade” leaving behind various types of defects. The severity of damage could be quantified by using a criterion called “DPA” or Displacement Per Atom that measures how many times every atom in the system has been displaced. In the same scope, one of the biggest challenges to the nuclear power plants is the embrittlement effect on the reactor pressure vessel (PV).

The PV is the main component that determines the reactor lifetime. Figure 5 [51] illustrates how the pressure vessels can get brittle at room temperature due to radiation damage, where the upper shelf energy (USE) decreases, causing less energy absorption capabilities.

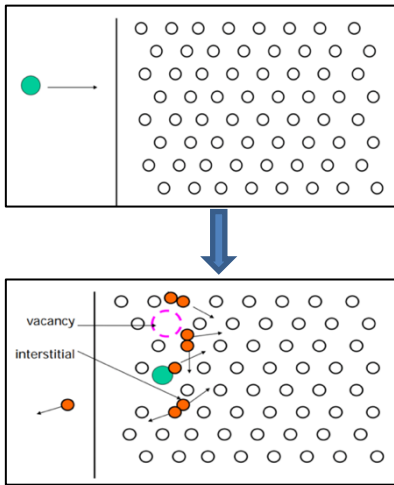


Figure 4 Schematic illustration of irradiation damage [50].

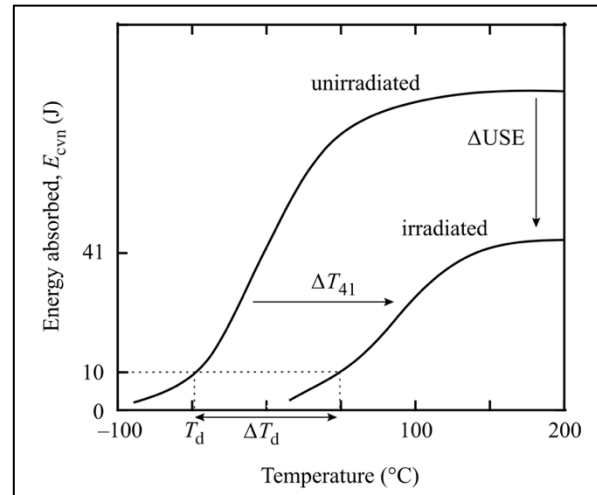


Figure 5 An illustration of the Irradiation-Induced Embrittlement process in Ferritic Steels, Reactor Pressure vessel (PV). The figure shows the ductile-to-brittle transition temperature (DBTT) and the Upper Shelf Energy (USE) reduction [51].

The following subsections in this chapter were designed first to explain, in detail, the technical background related to the phase-field modeling of fracture that was utilized to simulate this work cases of studies. Second, we described this work experimental study that was conducted to understand the fuel fracturing behavior of sintered UO_2 pellets when exposed to thermal shock. These experimental works were utilized to validate our model results. The detailed technical backgrounds presented in this chapter are crucial to interpreting this work model formations and results.

2.1 Phase Field Modeling of Fracture

Here we shall introduce the detailed formation of the phase-field modeling of fracture and illustrate the implantation of the brittle fracture case. This modeling approach aims to evolve the displacement field and the cracks set/surfaces by minimizing the system's total free energy, which is generalized to Griffith's theory [5]. A detailed description of the phase-field modeling of fracture governing equations was presented first then tailgated by the crack equilibrium profile analysis in 1-D. The analytical calculations of the expected critical stress and strains were also derived in the 1-D case. Finally, the phase-field model parameters, such as the gradient energy coefficient (κ) and the surface energy (γ), were evaluated at the end. More details about the model's history and developments are presented in Chapter III.

2.1.1 The phase-field modeling of fracture governing equations

The crack propagations in phase-field modeling of fracture took place due to the competition between the stored and surface energies. The system total free energy can be described as:

$$F_{\text{total}} = \Psi_{\text{stored}} - \Psi_{\text{external}} + \Psi_{\text{surface}} \quad \text{Eq 2.3}$$

While the Ψ_{external} , is the external potential energy denoted as :

$$\Psi_{\text{external}} = \int_{\Omega} b^* \cdot \mathbf{u} \, dV + \int_{\partial\Omega_t} t^* \cdot \mathbf{u} \, dA \quad \text{Eq 2.4}$$

Here, b^* and t^* are the macroscopic body force and boundary tractions, respectively. $\partial\Omega_t$ is the Neumann boundary. Considering the smeared nature of the crack in the phase field modeling, the stored energy functional Ψ_{stored} is given by:

$$\Psi_{\text{stored}}(\mathbf{u}, \eta_d) = \int_{\Omega} \Psi(\epsilon(\mathbf{u}), \eta_d) dV \quad \text{Eq 2.5}$$

The surface energy can be generalized as :

$$\Psi_{\text{surface}} = \mathcal{G}_c \int_{\Omega} \frac{1}{2l} (\eta_d^2 + l^2 |\nabla \eta_d|^2) dV = \int_{\mathcal{B}} \mathcal{G}_c \gamma(\eta_d, \nabla \eta_d) dV \quad \text{Eq 2.6}$$

Where, \mathcal{B} is the localization band $\mathcal{B} \subseteq \Omega$ over which the crack is smeared. And

$\gamma(\eta_d, \nabla \eta_d)$ is the generalized crack surface density function.

With that, the total free energy of the system could be expressed as follow:

$$F(\mathbf{u}, \eta_d) = \int_{\Omega} \Psi(\epsilon(\mathbf{u}), \eta_d) dV + \mathcal{G}_c \int_{\Omega} \frac{1}{2l} (\eta_d^2 + l^2 |\nabla \eta_d|^2) dV - \int_{\Omega} \mathbf{b}^* \cdot \mathbf{u} dV - \int_{\partial \Omega_t} \mathbf{t}^* \cdot \mathbf{u} dA \quad \text{Eq 3.8}$$

The displacement and the damage phase-field order parameter (\mathbf{u}, η_d) are determined by solving the following minimization argument.

$$(\mathbf{u}(\mathbf{x}), \eta_d(\mathbf{x})) = \text{Arg}\{\min F(\mathbf{u}, \eta_d)\} \quad \text{subject to } \eta_d \geq 0, \quad \eta_d \in [0,1] \quad \text{Eq. 2.7}$$

It worth noting that, the constitutive relation for the mechanical stresses, that is obtained by thermodynamic reasoning [52], is defined as:

$$\sigma = \frac{\partial \Psi}{\partial \epsilon} \quad \text{Eq. 2.8}$$

To obtain the governing equations, we derived the first derivative of the total free energy functional, as presented below:

$$\delta F = \int_{\Omega} \sigma \delta \epsilon \, dV + \int_{\mathcal{B}} \frac{\partial \Psi}{\partial \eta_d} \delta \eta_d \, dV + \int_{\mathcal{B}} \mathcal{G}_c \left(\frac{\partial \gamma}{\partial \eta_d} \delta \eta_d + \frac{\partial \gamma}{\partial \nabla \eta_d} \cdot \delta \nabla \eta_d \right) \, dV \quad \text{Eq. 2.9}$$

$$- \int_{\Omega} b^* \cdot \delta \mathbf{u} \, dV - \int_{\partial \Omega_t} t^* \cdot \delta \mathbf{u} \, dA$$

The stationary condition of the total free energy functional i.e., $\delta F = 0$ for $\delta \eta_d > 0$ and $\delta F > 0$ for $\delta \eta_d = 0$, gives the rise to the following governing equations:

$$\text{On mechanics side} \begin{cases} \nabla \cdot \sigma + b^* = 0 & \text{in } \Omega \\ \sigma \cdot n = t^* & \text{on } \partial \Omega_t \end{cases} \quad \text{Eq. 2.10a}$$

$$\text{on phase - field} \begin{cases} \underbrace{-g'(\eta_d) \frac{\partial \Psi}{\partial g}}_{\text{Crack driving force}} - \underbrace{\mathcal{G}_c \left(\frac{\partial \gamma}{\partial \eta_d} - \nabla \cdot \left(\frac{\partial \gamma}{\partial \nabla \eta_d} \right) \right)}_{\text{Crack resistance}} = 0, \eta_d > 0 \text{ in } \mathcal{B} \\ \underbrace{-g'(\eta_d) \frac{\partial \Psi}{\partial g}}_{\text{Crack driving force}} - \underbrace{\mathcal{G}_c \left(\frac{\partial \gamma}{\partial \eta_d} - \nabla \cdot \left(\frac{\partial \gamma}{\partial \nabla \eta_d} \right) \right)}_{\text{Crack resistance}} < 0, \eta_d = 0 \text{ in } \mathcal{B} \end{cases} \quad \text{Eq. 2.10b}$$

2.10b

2.1.2 The equilibrium profile in One-Dimensional analysis

In this study, we utilized a quadratic function for both: surface density function, $\gamma(\eta_d, \nabla \eta_d)$ and Degradation function $g(\eta_d)$ due to its numerical stability [52]. By applying the minimization conditions $\left(\frac{\partial \gamma(\eta_d, \nabla \eta_d)}{\partial \eta_d} \right)$ to the aforementioned crack surface density function, $\gamma(\eta_d, \nabla \eta_d) = \frac{1}{2l} (\eta_d^2 + l^2 |\nabla \eta_d|^2)$ that leads to an ordinary differential equation (ODE) with the form:

$$\frac{1}{l_0} \eta_d(x) - l_0 \eta_d''(x) = 0 \quad \text{Eq. 2.11}$$

The solution of this ODE gives the rise to the crack phase-field $\eta_d(x)$ equilibrium profile.

For a better representation of the phase-field regulation we consider a smeared crack at

$x = 0$ in 1-D, the following exponential equation is the solution of the ODE represented in Eq. 2.11 and satisfying these conditions: $\eta_d(x = 0) = 1$, $\eta_d(x) \rightarrow 0: x \rightarrow \pm\infty$. This was first represented by Miehe et al. [28, 29]:

$$\eta_d(x) = \exp\left(-\frac{|x|}{l_0}\right) \quad \text{for } -\infty < x < \infty \quad \text{Eq. 2.12}$$

l_0 is the characteristic length scale that determine the cracked smeared region. The influences of l_0 and Eq. 2.12 were represented in the crack equilibrium profile, see Figure 6 [52].

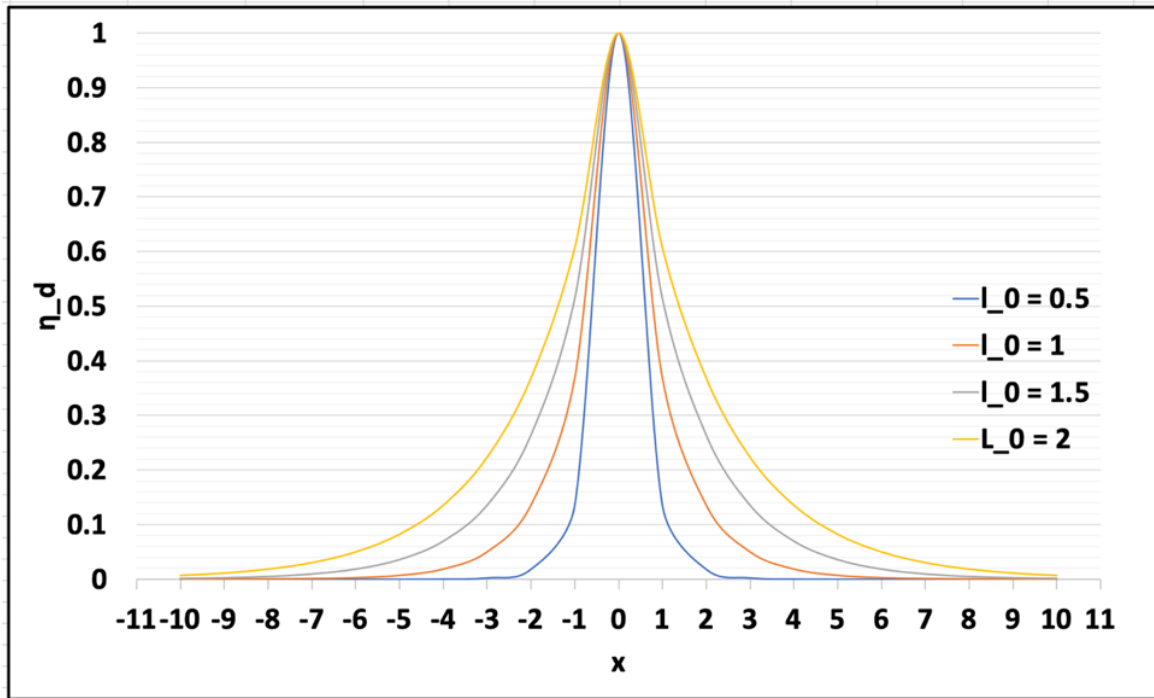


Figure 6 An illustration of the crack profile solution in 1-D case that shows the influences of the characteristic length scale parameters l_0 on the smeared crack region.

2.1.3 Critical stress and strain analysis in One-Dimensional solution

Here, we shall introduce a detailed analytical result of the Phase-Field fracture model in 1-D. We considered a softening bar in uniaxial traction. This bar has a length of $2L$ in which position $x \in [-L, L]$. The bar is loaded at both ends thus, the displacement \mathbf{u} increased in both opposite directions. To define the state equilibrium of the bar we assumed $\sigma_x = 0$, the stress-strain relation is defined as $\sigma = g(\eta_d) E_0 \epsilon$, where E_0 is the young's modulus, ϵ is the strain. Thus, all the following set of equations are holds for this 1-D analysis:

$$\sigma = g(\eta_d) E_0 \epsilon \quad \text{Eq. 2.13a}$$

$$\sigma_x = 0 \quad \text{Eq. 2.13b}$$

$$-g'(\eta_d) \frac{\partial \Psi}{\partial g} - \mathcal{G}_c \left(\frac{\partial \gamma}{\partial \eta_d} \right) = 0 \quad \text{Eq. 2.13c}$$

For the sake of generalization and to apply the analytical methods for different combinations of degradation functions $g(\eta_d)$ and geometric crack function $\alpha(\eta_d)$, in this work we used $\alpha(\eta_d) = \eta_d^2$. Thus, surface function density $\gamma(\eta_d, \nabla \eta_d)$ can be defined as:

$$\gamma(\eta_d, \nabla \eta_d) = \frac{1}{c_0} \left[\frac{1}{l_0} \alpha(\eta_d) + \iota_0 |\nabla \eta_d|^2 \right] \quad \text{Eq. 2.14}$$

where, c_0 is a scaling parameter = 2. With that, the generalized form of the Eq. 2.13c is redefined as:

$$\frac{\mathcal{G}_c}{c_0} \left[\frac{1}{l_0} \alpha'(\eta_d) - 2\iota_0 \eta_d''(x) \right] + \frac{1}{2} g'(\eta_d) E_0 \epsilon^2 = 0 \quad \text{Eq. 2.15}$$

For simplicity, let's introduce a monotonically increasing function $\omega(\eta_d) = \frac{1}{g(\eta_d)} - 1$,

thus the general formulation of the degradation function would be defined as:

$$g(\eta_d) = \frac{1}{1+\omega(\eta_d)} \quad \text{Eq. 2.16a}$$

$$g'(\eta_d) = -g^2(\eta_d) \omega'(\eta_d) < 0 \quad \text{Eq. 2.16b}$$

sub Eq 2.16b into Eq. 2.15 leads to:

$$\frac{g_c}{c_0} \left[\frac{1}{\iota_0} \alpha'(\eta_d) - 2\iota_0 \eta_d''(x) \right] = \frac{1}{2} g^2(\eta_d) \omega'(\eta_d) E_0 \epsilon^2 \quad \text{Eq. 2.17}$$

Sub Eq. 2.16a into Eq. 2.17, then:

$$\frac{2E_0 g_c}{c_0} \left[\frac{1}{\iota_0} \alpha'(\eta_d) - 2\iota_0 \eta_d''(x) \right] = \sigma^2 \omega'(\eta_d) \quad \text{Eq. 2.18a}$$

$$\sigma^2 \omega'(\eta_d) - A_0 [\alpha'(\eta_d) - 2\iota_0^2 \eta_d''(x)] = 0 \quad , \text{ where } A_0 = \frac{2E_0 g_c}{\iota_0 c_0} \quad \text{Eq. 2.18b}$$

Assuming a homogenous solution i.e., the strain field are uniformly distributed along the bar. Thus, the identity $\eta_d''(x) = 0$, then :

$$\sigma = \sqrt{A_0 \frac{\alpha'(\eta_d)}{\omega'(\eta_d)}}, \quad \epsilon = \frac{1}{E_0} \sqrt{-A_0 \frac{\alpha'(\eta_d)}{g'(\eta_d)}}, \quad \mathbf{u} = \epsilon L = \frac{L}{E_0} \sqrt{-A_0 \frac{\alpha'(\eta_d)}{g'(\eta_d)}} \quad \text{Eq. 2.19}$$

Here we assume a quadratic geometric crack function and quadratic degradation function in which $\alpha(\eta_d) = \xi \eta_d + (1 - \xi) \eta_d^2$, $c_0 = 2$, & $g(\eta_d) = (1 - \eta_d)^2$.

Thus $\alpha'(\eta_d) = 2(1 - \xi) \eta_d + \xi$ and $\omega'(\eta_d) = \frac{2}{(1 - \eta_d)^3}$, by sub into Eq. 2.19 it turns

into:

$$\sigma = \sqrt{\frac{E_0 g_c}{c_0 \iota_0} (2(1 - \xi) \eta_d + \xi)(1 - \eta_d)^3} \quad \text{Eq. 2.20}$$

2.1.3.1 Quadratic crack surface density and strain degradation functions

For a quadratic geometric crack function and quadratic degradation function in which $\alpha(\eta_d) = \eta_d^2$, $c_0 = 2$, & $g(\eta_d) = (1 - \eta_d)^2$, the critical crack phase-field η_{d_c} is solved as $\left. \frac{\partial \sigma}{\partial \eta_d} \right|_{\eta_{d_c}} = 0$. Thus,

$$\left[g(\eta_{d_c})g''(\eta_{d_c}) - 2g'(\eta_{d_c})^2 \right] \eta_{d_c} = g'(\eta_{d_c}) \cdot g(\eta_{d_c}) \quad \text{Eq. 2.21a}$$

$$\text{sub } g(\eta_{d_c}) = (1 - \eta_{d_c})^2$$

$$\left[(1 - \eta_{d_c})^2 \cdot 2 - 2 \left(2 \left((1 - \eta_{d_c}) \right) \right)^2 \right] \eta_{d_c} = 2(1 - \eta_{d_c})(1 - \eta_{d_c})^2 \quad \text{Eq. 2.21b}$$

This leads to $\eta_{d_c} = \frac{1}{4}$, by substituting in Eq. 3.21, then:

$$\sigma_c = \frac{3}{16} \sqrt{\frac{3E_0 G_c}{l_0}} \quad \text{and} \quad \epsilon_c = \sqrt{\frac{G_c}{3E_0 l_0}} \quad \text{Eq. 2.22}$$

Figures 7 and 8 are presenting the homogenous stress-strain behavior and the phase-field order parameter η_d vs. strain, respectively. In these figures we used a unity value for both G_c and E_0 for simplicity. It worth noting that, these two figures illustrate the decreasing of the maximum stress due to an increasing in l_0 values. Someone can observe that once $l_0 \xrightarrow{\text{tends to}} 0$, $\sigma \xrightarrow{\text{tends to}} \infty$ that is consistent with the Griffith expectations [5]. An assessment of various combinations of geometric, degradations functions were presented in detail by Wu et al., [52] and summarized in Table 1 [52].

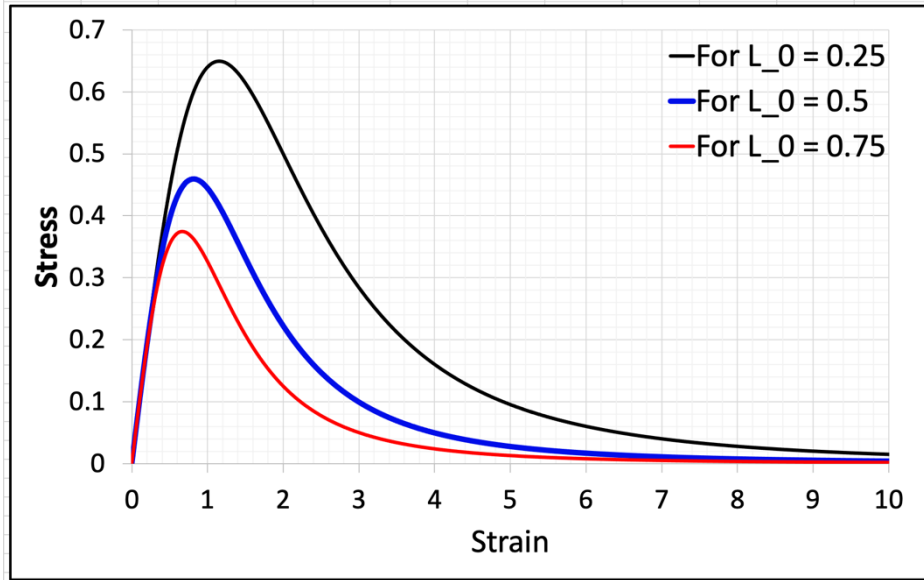


Figure 7 One dimensional homogenous Stress-Strain Curve for different length scale (l_0) while the geometric function and the degradation functions are $\alpha(\eta_d) = \eta_d^2$ & $g(\eta_d) = (1 - \eta_d)^2$, respectively.

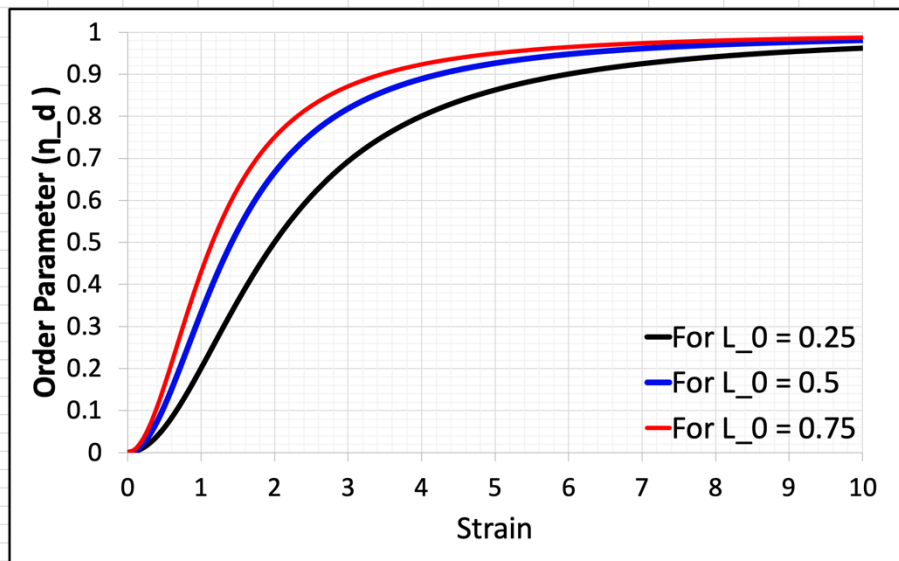


Figure 8 One dimensional homogenous behavior of order parameter η_d vs. strain for different length scale (l_0) while the geometric function and the degradation functions are $\alpha(\eta_d) = \eta_d^2$ & $g(\eta_d) = (1 - \eta_d)^2$, respectively.

Table 1 Various combinations of geometric crack functions $\alpha(\eta_d)$ and energetic degradation functions $g(\eta_d)$ along with the corresponding critical stress σ_c and strains ϵ_c [52].

$\alpha(\eta_d)$	$g(\eta_d)$	σ_c	ϵ_c
η_d^2	$(1 - \eta_d)^2$	$\frac{3}{16} \sqrt{\frac{3E_0 G_c}{l_0}}$	$\sqrt{\frac{G_c}{3E_0 l_0}}$
η_d^2	$3(1 - \eta_d)^2 - 2(1 - \eta_d)^3$	$\frac{27}{250} \sqrt{\frac{30E_0 G_c}{l_0}}$	$\sqrt{\frac{10G_c}{27E_0 l_0}}$
η_d^2	$4(1 - \eta_d)^3 - 3(1 - \eta_d)^4$	$\frac{128}{243} \sqrt{\frac{2E_0 G_c}{3l_0}}$	$\frac{9}{16} \sqrt{\frac{2G_c}{3E_0 l_0}}$
η_d	$(1 - \eta_d)^2$	$\sqrt{\frac{2E_0 G_c}{8l_0}}$	$\sqrt{\frac{3G_c}{8E_0 l_0}}$

2.1.3.2 Quadratic crack density function and cubic strain degradation function

Similarly, here we are implementing a mix of a quadratic crack density function $\alpha(\eta_d) = \eta_d^2$ and cubic degradation function $g(\eta_d) = 3(1 - \eta_d)^2 - 2(1 - \eta_d)^3$, second row in Table 1. In this case, the critical crack phase-field $\eta_{d,c}$ is also solved

based on $\left. \frac{\partial \sigma}{\partial \eta_d} \right|_{\eta_{d,c}} = 0$, this leads to a $\eta_{d,c} = 0.1$ and:

$$\sigma_c = \frac{27}{250} \sqrt{\frac{30E_0 G_c}{l_0}} \quad \& \quad \epsilon_c = \sqrt{\frac{10G_c}{27E_0 l_0}} \quad \text{Eq. 2.23}$$

with a distinguished two regions:

1) Elastic stage, where $\epsilon \leq \bar{\epsilon}$, in which the is the elastic strain limit and $\bar{\epsilon} = \sqrt{\frac{G_c}{3E_0l_0}}$,

thus: $\sigma = E_0\epsilon$ as $\eta_d = 0$

2) Inelastic region, $\epsilon \geq \bar{\epsilon}$, here: $\sigma = \left(\frac{G_c}{l_0}\right)^2 \left(\frac{9E_0\epsilon^2 - 2G_c/l_0}{27E_0^2\epsilon^5}\right)$ with $\eta_d = 1 - \frac{G_c}{3E_0l_0\epsilon^2}$

Figure 9 illustrates the comparison between both quadratic functions and the set of quadratic crack density with cubic degradation functions. This shows the near-to-homogeneous stress-strain curve of cubic function is almost linear in elastic before the damage starts. Furthermore, the maximum homogeneous stress is higher than the corresponding quadratic value, which results in a larger characteristic length scale for the same critical stress and thus decreases the computational cost [40].

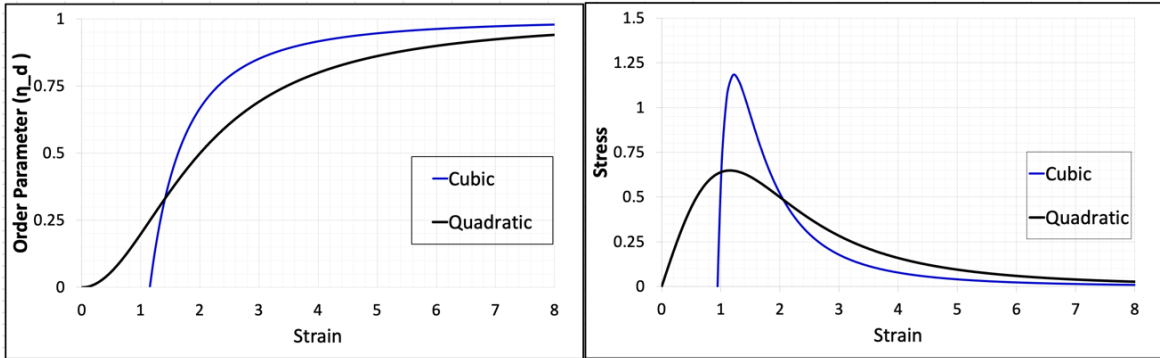


Figure 9 A 1-D homogeneous solution to investigate the phase-field order parameter Vs. Strain (left) and stress-strain curves (right). In this investigation, we illustrate the difference in implementing the crack density as quadratic function vs. quadratic and cubic degradation functions. Here, we implemented the characteristic length scale with a constant value ($l_0 = 0.25$). The cubic degradation function is associated with higher homogenous stress, decreasing the computational cost due to the flexibility of selecting higher l_0 .

2.1.4 Allen–Cahn-type evolution equations to a phase field model of fracture

To avoid crack healing, a history variable H is required that is representing the maximum energy density over the time interval (t). Thus,

$$H = \max_t(\Psi^+)$$

Now, the total free energy is redefined as:

$$\begin{aligned} F_{\text{total}} &= g(\eta_d) H + \Psi^- + \frac{g_c}{c_0} \left[\frac{1}{l_0} \alpha(\eta_d) + l_0 |\nabla \eta_d|^2 \right] \\ F_{\text{total}} &= \underbrace{f_{\text{elastic}} + f_{\text{fracture}}}_{f_{\text{local}}} + \frac{g_c l_0}{c_0} |\nabla \eta_d|^2 \end{aligned} \quad \text{Eq 2.24}$$

Where,

$$\begin{aligned} f_{\text{elastic}} &= g(\eta_d) H + \Psi^- \\ f_{\text{fracture}} &= \frac{g_c l_0}{c_0} \alpha(\eta_d) \end{aligned} \quad \text{Eq 2.25}$$

The evolution equation for the phase field damage parameter follows the Allen-Cahn equation, such that:

$$\dot{\eta}_d = -L \frac{\delta F_{\text{total}}}{\delta \eta_d} \quad \text{Eq 2.26}$$

The total free energy first derivative with respect to the damage parameter (η_d) is:

$$\frac{\partial F_{\text{total}}}{\partial \eta_d} = g'(\eta_d) H + \frac{g_c l_0}{c_0} \alpha'(\eta_d) \quad \text{Eq 2.27}$$

The total free energy second derivative with respect to the damage parameter (η_d) is:

$$\frac{\partial^2 F_{\text{total}}}{\partial^2 \eta_d} = g''(\eta_d) H + \frac{g_c l_0}{c_0} \alpha''(\eta_d) \quad \text{Eq 2.28}$$

Thus, the Allen–Cahn-type evolution equation to this phase field model of fracture is:

$$\dot{\eta}_d = -L \frac{\delta F_{\text{total}}}{\delta \eta_d} = -L \left(g'(\eta_d) H + \frac{g_c l_0}{c_0} \alpha'(\eta_d) - \nabla \cdot \kappa \nabla \eta_d \right) \quad \text{Eq 2.29}$$

Or

$$\dot{\eta}_d = -L \frac{\delta F_{total}}{\delta \eta_d} = -L \left(g'(\eta_d) \frac{\partial \psi^+}{\partial \eta_d} + \frac{G_c l_0}{c_0} \alpha'(\eta_d) - \nabla \cdot \kappa \nabla \eta_d \right) \quad \text{E 2.30}$$

Where, L is the Allen-Cahn mobility and equals to the inverse of viscosity, while the gradient coefficient (κ) can be evaluated as:

$$\kappa = \frac{2G_c l_0}{c_0} \quad \text{Eq 2.31}$$

To evaluate the crack surface energy (γ); by considering an equilibrium case in which the driving force vanish. Thus, we start by rewriting Eq 2.30 as:

$$\frac{\dot{\eta}_d}{L} = -g'(\eta_d) \frac{\partial \psi^+}{\partial \eta_d} + \kappa \nabla^2 \eta_d \quad \text{Eq 2.32}$$

The energy of the crack surfaces as defined by Levitas et al. [53], is the excess energy with respect to the bulk materials and is related to the energy release rate ($G_c = 2\gamma$) [54] and the surface tension ($2\gamma = \int_{-\infty}^{+\infty} \sigma_{st} d\Omega$) [53]. With that and similar to [53], the Allen-Cahn equation in one-dimensional case can be expresses as:

$$\frac{\partial \psi^+}{\partial \eta_d} = \frac{d}{d\eta_d} \left(\frac{2\gamma}{d} \alpha(\eta_d) \right) = \kappa \frac{d^2 \eta_d}{dx^2} \quad \text{Eq 2.33}$$

Here, “ d ” is the initial distance between two plans forming crack surfaces and related to the aforementioned characteristic length scale (l_0). Thus, we might introduce a new parameter “ A ”, that is depending on the crack surface energy in which, $A(\gamma) = \frac{2\gamma}{d}$.

It worth noting that, this one-dimensional analysis is considered along the X-axis that is along the direction normal to the crack surface. Thus,

$$\frac{d^2 \eta_d}{dx^2} = \frac{d\eta'_d}{dx} = \frac{d\eta'_d}{d\eta_d} \frac{d\eta_d}{dx} = \frac{d\eta'_d}{d\eta_d} \eta'_d = \frac{1}{2} \frac{d(\eta'_d)^2}{d\eta_d} \quad \text{Eq 2.34}$$

Then,

$$\frac{d}{d\eta_d} \left(\frac{2\gamma}{d} \alpha(\eta_d) \right) = \frac{\kappa}{2} \frac{d(\eta'_d)^2}{d\eta_d} \quad \text{Eq 2.35}$$

By integrating over $d\eta_d$, then:

$$\frac{\kappa}{2} \eta'_d{}^2 = \frac{2\gamma}{d} \alpha(\eta_d) \quad \text{Eq 2.36}$$

By implementing a boundary condition for η_d , in which $\eta_d(\pm\infty) = \eta'_d(\pm\infty) = 0$, one can obtain the generalized expression for the crack surface profile as :

$$\eta_d = \frac{3}{2} \left(1 - \left(-1 + \frac{2}{1 + (2 - \sqrt{3}) e^{-\sqrt{\frac{12\gamma}{\kappa d} |x|}}} \right)^2 \right) \quad \text{Eq 2.37}$$

This generalized crack surface profile is shown in Figure 10. Note that, this equation is the generalized form of the crack surface profile that was derived in Eq 2.12 and in Figure 6. Once Eq 2.36 is generalized for the multidimensional case, this leads to an interesting description of the gradient energy ($\psi^\nabla = A(\gamma) \alpha(\eta_d)$), in which the gradient energy is equal to the excess of the local energy.

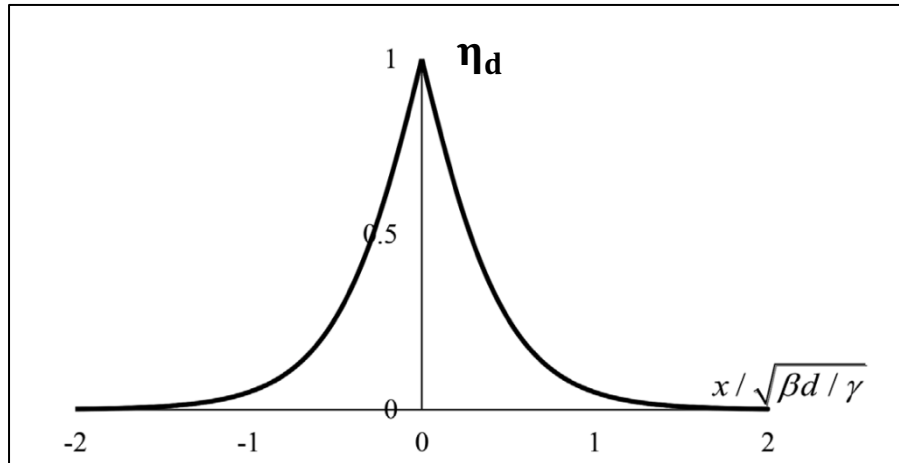


Figure 10 Generalized crack profile in 1D, β is constant [53].

It worth noting that the surface energy (ψ^{surf}) is defined as the excess of the strain-independent energy while considering the intact region [53]. Thus, and by utilizing equation Eq 2.36, the surface energy can be evaluated as:

$$\psi^{\text{surf}} = 2\gamma = 2A(\gamma) \int_{-\infty}^{+\infty} \alpha(\eta_d) dx = 4A(\gamma) \int_{-\infty}^0 \alpha(\eta_d) dx \quad \text{Eq 2.38}$$

To be consistent with the definition, we might need to integrate only over the range of the damage parameter (η_d), Thus:

$$\psi^{\text{surf}} = 4A(\gamma) \int_0^1 \alpha(\eta_d) \frac{dx}{d\eta_d} d\eta_d \quad \text{Eq 2.39}$$

From Eq 2.35, $\frac{d\eta_d}{dx} = \sqrt{\frac{4\gamma\alpha(\eta_d)}{\kappa d}}$, while $A(\gamma) = \frac{2\gamma}{d}$. Hence, Eq 2.39 can be written as:

$$\psi^{\text{surf}} = 4A(\gamma) \int_0^1 \alpha(\eta_d) \frac{dx}{d\eta_d} d\eta_d = 2\sqrt{2A(\gamma) \kappa} \int_0^1 \sqrt{\alpha(\eta_d)} d\eta_d \quad \text{Eq 2.40}$$

Note that, the term $\int_0^1 \sqrt{\alpha(\eta_d)} d\eta_d$ is a constant since it's a finite integration over an interpolation function, hence $Y = \int_0^1 \sqrt{\alpha(\eta_d)} d\eta_d$ is a constant number. Also, the gradient coefficient (κ) that is introduced in Eq 2.31 can be generalized to, $\kappa = \frac{\gamma d}{4Y^2}$.

Reference [53] evaluated these parameters for different geometrical functions.

2.2 Thermal Fracture in sintered UO₂ Pellets¹

Most commercial nuclear power plants in U.S. and worldwide use UO₂ as fuel. Despite downsides with high-thermal strains due to poor thermal conductivity, UO₂ is still the primary choice for Light Water Reactors (LWRs) due to its high melting point (2865 °C), lack of phase changes up to its melting point (unlike metallic fuels), good corrosion resistance, and fission product retention [19]. Fuel fracturing impacts the thermo-mechanical properties of UO₂ during normal and transient operation. Since UO₂ has a very low thermal conductivity [55], a range thermal gradient can build up (Soret effect) with a mass gradient leading to the initiation of pores.

In as-fabricated unirradiated LWR fuel, volumetric heating from fission is mostly spatially uniform (except on the pellet periphery). As burnup increases, self-shielding effects result in higher volumetric heat generation around the perimeter of the fuel pellets [12, 56]. The heat is transferred radially outward from the fuel pellet, across the fuel-cladding gap, through the cladding, and finally into the coolant where it converts aqueous water into gaseous steam. During reactor operation, nuclear fuels experience swelling and form voids and bubbles, which may cause the pellet to fracture at higher temperatures. Fuel fracturing may occur when the fuel is thermally shocked, or a rapid decrease in temperature as a result of the thermo-mechanical stress incurred by the grain boundaries

¹ Reprinted with permission from Elsevier "Experimentally validated Multiphysics modeling of fracture induced by thermal shocks in Sintered UO₂ Pellets" by L. D. McClenny, M. I. Butt, M. Goma Abdoelatef, M. J. Pate, K. L. Yee, R. Harikrishnan, D. Perez-Nunez, W. Jiang, L. H. Ortega, S. M. McDevitt and K. Ahmed, 2022. , Journal of Nuclear Materials. Copyright [2022] by Journal of Nuclear Materials.

of the material and varies depending on density, porosity, chemical composition, and microstructural state. Non-uniform thermal expansion in the fuel pellet causes compressive stresses in the center and tensile stresses on the exterior. This hoop stress as a function of radial position is pictured in Figure 11. It can be observed from the plot that radial cracking occurs as the tensile hoop stress surpasses the tensile strength of the fuel due to increasing power [57].

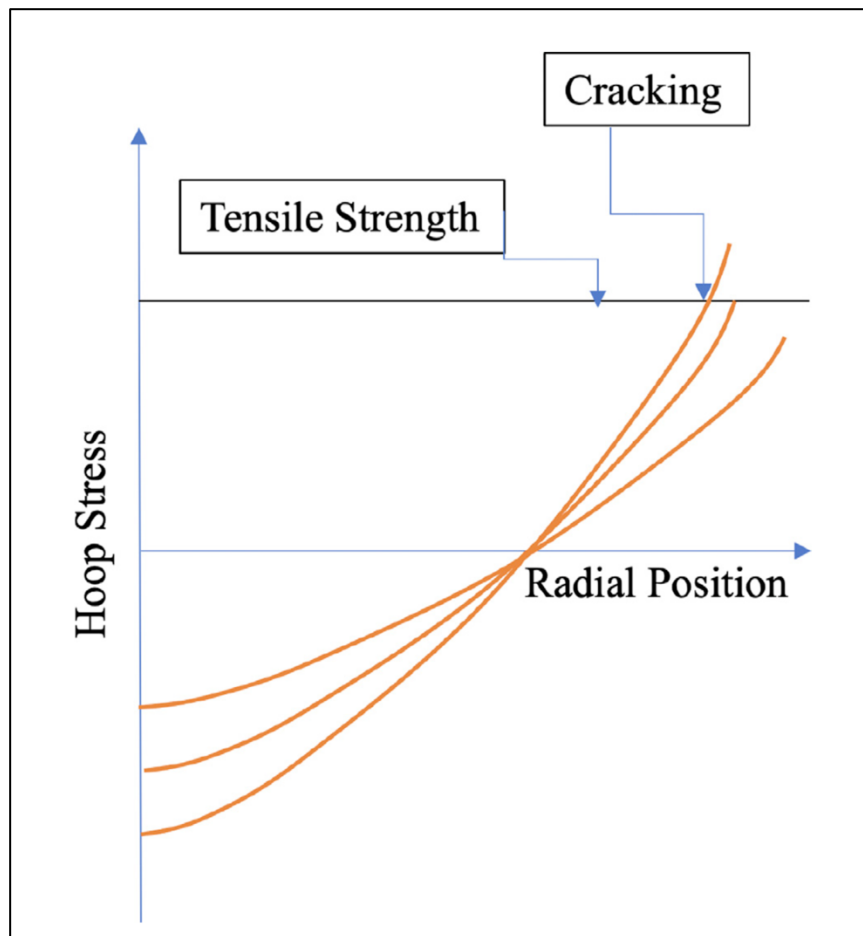


Figure 11 Plot of variation in hoop stress in fresh LWR fuel as a function of radial position during ramping to full power [19, 57].

The tensile strength of UO_2 is about 150 MPa and fracture initiation is expected to occur when the hoop stress surpasses this value [57]. In this work, a coupled experimental and computational approach was utilized to investigate thermal fracture in UO_2 . First, to induce fracture in UO_2 pellets, the pellets were submerged in molten salts and heated to a temperature in the range of (589– 676 °C). Then these pellets were subjected to a rapid temperature decrease to mimic accidents-like transients. Second, the computational model was used to simulate, reproduce, and interpret the experimental data. More details about this work experiment were illustrated in [19]. This work experimental results were used to validate our Phase-Field model of fracture in UO_2 , as demonstrated here, in the result section.

2.3 The Experimental work of thermal shocks induced fracture in UO_2 ²

Fuel fracturing in LWRs is a well expected occurrence during reactor operation, however, limited experimental data with varying configurations (such as high-burnup fuel) of fracture initiation and propagation of UO_2 fuel pellets exists. Since replication of a LWR environment for a fuel pellet is difficult due to the temperature profile being a result of a combination of volumetric fission heating and coolant heat removal, few have taken on this challenge [57]. With this limited data availability, novel modeling approaches cannot be implemented with certainty. This work results would add upon current literature data that allow further investigations for radial relocation, pellet-cladding mechanical interactions, and fragmentation phenomena to benefit fuel performance objectives in LWRs. To fulfill this requirement for further experimental validation, fuel fracturing experiments were carried out that subject the fuel to a temperature profile that allows for an observation of the cracking propagation and emphasizes fuel cracking rather than any unrelated phenomena.

As part of a three-component experimental study focused on different heating methods of UO_2 fuel, the purpose of this particular experiment was to slowly heat a fuel pellet contained in a metal tube assembly to a high temperature and subsequently quench said tube in a cold bath designed to insulate the top and bottom portions of the cylindrical pellet to generate a radial heat flux [19, 57]. Figure 12 displays an expected temperature

² Reprinted with permission from Elsevier "Experimentally validated Multiphysics modeling of fracture induced by thermal shocks in Sintered UO_2 Pellets" by L. D. McClenny, M. I. Butt, M. Gomma Abdoelatef, M. J. Pate, K. L. Yee, R. Harikrishnan, D. Perez-Nunez, W. Jiang, L. H. Ortega, S. M. McDevitt and K. Ahmed, 2022. , Journal of Nuclear Materials. Copyright [2022] by Journal of Nuclear Materials.

profile of the quenching process when cooling from a spatially uniform high temperature. The UO_2 pellets used for this study were manufactured at Texas A&M University's Fuel Cycle and Materials Laboratory (FCML) using powder metallurgical methods and sintering to produce cylindrical UO_2 fuel pellets of approximately 9–10 mm in height and 10–11 mm diameter each. Fuel pellets of varying density, diameter, and heights were used in the thermal shocking experiments.

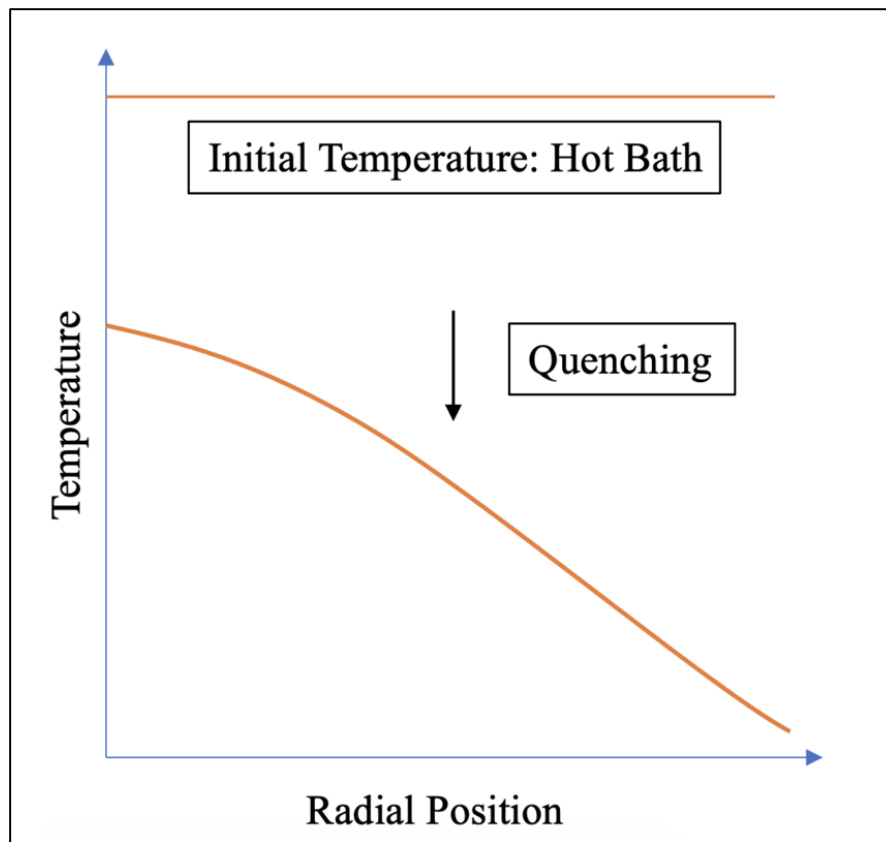


Figure 12 Plot of expected temperature profile during quenching after achieving a spatially uniform high temperature in the pellet [19] [57].

2.3.1 Experimental methods

Experimental data has been collected on fuel fracturing of sintered UO_2 pellets by thermally shocking them in high-temperature conditions (~ 700 °C ternary carbonate salt) and subsequently in sub-zero conditions (-10 °C in water or 1:1 ethylene glycol:water). More detail about the experimental procedures can be found in [19] and Ortega et al [58]. Here, we present Multiphysics computational modeling approaches and additional experimental results, extending the work performed by Ortega et al. [58] and adding supplemental discussion. The

experimental set-up consists of a UO_2 pellet resting on a ceramic cylinder, which is inserted into a copper tube in a sealed Swagelok assembly. Insulation is placed on one side of the fuel pellet to increase thermal conductivity through the copper on one side. It is worth noting that the surface side area introduced to the cold bath (quenching) is $1/6$ of the total pellet surface area; a “contact area” will refer to this area throughout the following discussions, see Figure 13 (for a schematic illustration).

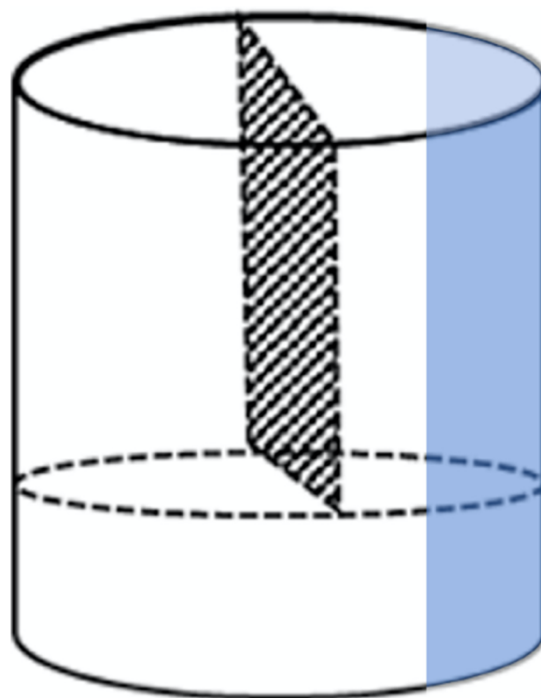


Figure 13 the pellets were cut into three parts which included two axial cuts and one radial cut to observe the fracture occurring in the samples. Note that shaded in blue is the contact area introduced to the cold bath ($1/6$ of the total pellet surface area). (For interpretation of the references to color in this figure legend, the reader is referred to the web version of this article.) [19]

The tube assembly is constructed inside of a helium-filled glovebox in order to reduce the oxidation rate of the fuel pellet, see Figure 14. A successful experiment is one that manages to induce fracture in the pellet as a result of the sudden temperature decrease from the heating in the hot salt bath to quenching in the cold bath. The thermal shock tests were characterized using two thermocouples attached to the assembly, one attached to the top of the pellet, and one attached to the out-side of the tubing to measure the temperature difference across the boundary. The inner thermocouple (0.3" diameter) is placed into a small divot drilled into the pellet and sealed with high temperature cement while the outer thermocouple is held in place using a hose clamp.



Figure 14 (left) Insertion of insulation and pellet U6-71B attached to the thermocouple into the capsule. (right) Solidworks rendering of the placement of the pellet in the capsule [19].

Figure 15 (b) shows an optical microscope image of a successfully cracked sample next to an example of temperature data from the same experiment, Figure 15 (a). Note the rapid decrease in temperature as the sample is quenched in the cold-water bath.

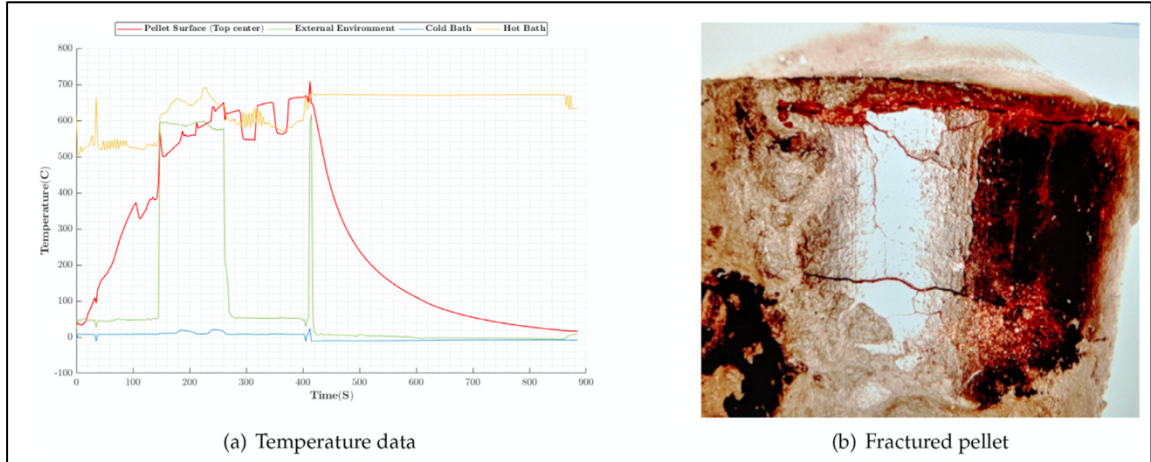


Figure 15 (a) Temperature readings of thermocouples from a pellet submersion experiment of a UO_2 pellet. Note that, the step changes seen in the plot are due to malfunction of thermocouples in the salt bath at the presented temperature. After reaching the appropriate temperature the sample was then quenched into the cold bath, hence the sudden and smooth drop. (b) Hirox image of a successfully cracked UO_2 pellet [19].

2.3.2 Experimental procedure

The capsule was submerged in the molten salt bath until the pellet's temperature reached equilibrium with that of the salt bath, about 11 min on average. A sample experimental temperature profile (which did result in fracture) collected via the LabVIEW software suite is shown in Figure 15 (a). The step shifts noticed in this figure exist due to the malfunction of thermocouples in the salt bath at the given temperature. Once approaching the proper temperature, the sample quenched into the cold bath, hence the sudden and smooth drop. Upon reaching the desired temperature, the capsule was removed

from the hot bath and immediately submerged into the cold bath. The capsule remained there until it cooled down to around room temperature.

Table 2 [19] shows the times and temperatures for each experiment. For select experiments, temperature data for the heating process was inaccurate as depicted with an asterisk in Table 3 [19]. However, upon removing the capsule, temperature readings stabilized with minimal variation. This malfunction in thermocouple readings may be caused by an interaction between the copper capsule and the molten salt bath. In the experiments that resulted in fracture which are primarily discussed in the main body of this contribution, physically compromised experiments were omitted from study.

Table 2 The submersion times and temperatures of each experiment [19] .

Pellet ID	Hot Bath Temp (°C)	Capsule Hot Bath Time (min)	Highest Pellet Temp (°C)	Cold Bath Temperature (°C)	Capsule Cold Bath Time (min)	Lowest Pellet Temp (°C)
U6-71B*	640	6	640	-10	7	35
U6-40*	670	7	667	-11	8	17
U2-25*	635	8	600	-9	8	0
U4-53C	700	9	662	-9	15	0
U4-42	559	10	586	4	10	25
U5-15A	683	11	676	5	12	10
U2-49	712	26	669	5	14	10

Table 3 Sintering profiles and associated calculated densities for various experiments [19]

Pellet ID	Mass (g)	Density (g/cc)	Sintering Profile
U6-71B	9.05	8.75	30 min at 350°C, 10 min at 1800°C
U6-40	9.29	9.82	30 min at 350°C, 12 hr at 1700°C, 5 hr cool down to 25°C
U2-25	9.41	9.79	30 min at 350°C, 8 hr at 1700°C, 5 hr cool down to 25°C
U4-53C	9.08	10.11	24 hr at 1790°C
U4-42	9.16	10.31	325 bakeout, 18 hr at 1675 °C
U5-15A	9.17	10.38	325 bakeout, 24 hr at 1790 °C
U2-49	9.11	10.04	325 bakeout, 3 hr at 1700 °C

The capsules were left in the fume hood for at least 24 h before they were opened, and the pellets were subsequently examined via aided and unaided means. Each pellet was imaged with an optical microscope for micro-level fracturing as well as unassisted user observation for macro-level fracture. The pellets that showed signs of cracking were placed into epoxy resin, sectioned, and polished for further imaging in the scanning electron microscope (SEM).

2.4 Fracture heterogeneity in TRISO Buffer layer

TRi-structural ISOtropic (TRISO) particle fuel includes Uranium Carbide (UCO) or Uranium Dioxide (UO₂) as a fuel kernel. The kernel is covered by four layers: Pyrocarbon buffer layer (buffer), an inner Pyrocarbon layer (IPyC), a SiC layer, and an outer Pyrocarbon layer (OPyC), as shown schematically in Figure 16 [59] and micrographically in figure 17 [59]. TRISO particles are super small in sizes (with ~ 500 microns in diameter) yet very robust. These fuel particles usually dispersed into larger spheres called “pebbles” to power both types of Advanced Reactors, molten salt-cooled [60] and high-temperature gas reactors [61]. Compared to the current nuclear reactors’ fuels, TRISO shows an excellent residence to the irradiation, oxidation, corrosion, and the high temperatures conditions [62]. TRISO fuel was first developed in the United States and the United Kingdom in the 1960s with Uranium Dioxide fuel [63].

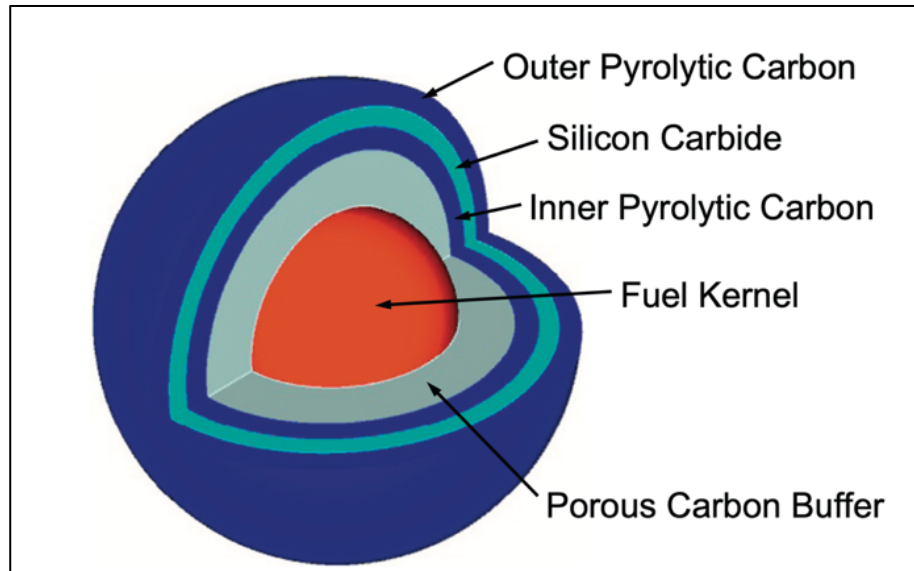


Figure 16 An illustration of the TRISO-layers that are coating the fuel kernel [59].

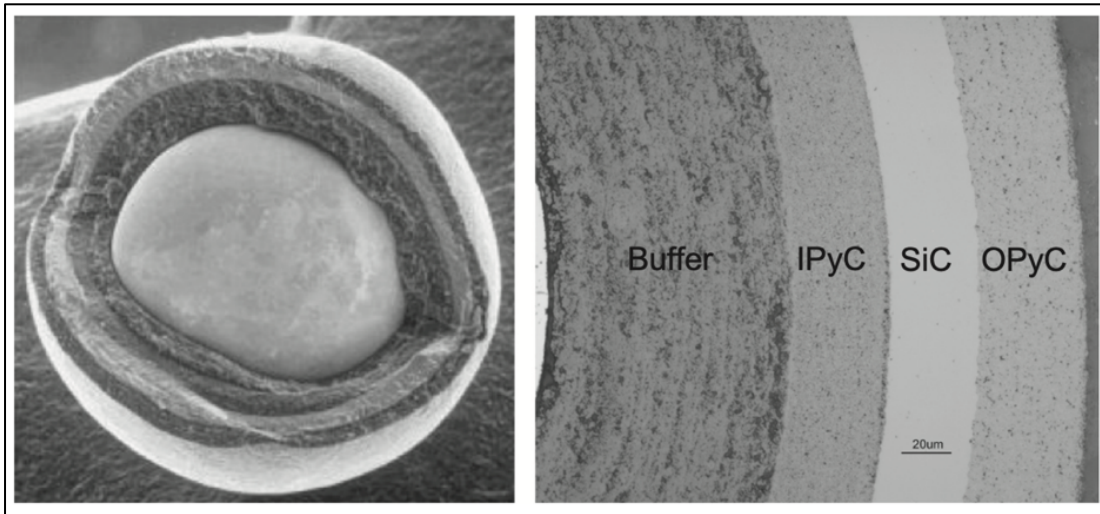


Figure 17 Micrographs images of TRISO particle. The left side shows the cracked particle, while the right side shows a zoom-in cross-sectional of the TRISO layers [59].

In 2009, Advanced Gas Reactor (AGR) testing of TRISO fuel based on UCO kernel introduced worldwide record by reaching nearly 19% maximum burnup throughout a three-year test at Idaho National Laboratory (INL). This record is approximately double the former record established by the Germans in the 1980s and is triple times the burnup values that are currently operated by the light-water reactors—demonstrating the TRISO excellent capability [20].

Albeit the outstanding performance that has been confirmed, AGR-1 [20] [21] and AGR-2 [22] observed TRISO particles failures due to the buffer layer behaviors under irradiation. TRISO Buffer layer has a lower density with higher porosity to maintain the fission gases. Under irradiation, buffer inward densification phenomena take place, which leads to buffer tearing, i.e., full, or partial buffer-IPyC debonding. Moreover, the buffer fracture happens while the fuel kernel swells outward. As illustrated in AGR-1, the

TRISO particles that exhibit buffer fracture was found more frequent with partial buffer-IPyC debonding [20] [21]. This stochastic behavior of buffer tearing, and buffer fracture inspired this work to utilize the phase-field approach to illustrate a mechanistic understanding of buffer (i.e., pores microstructure) behavior under various loading. The Buffer tearing depends on the stress that is developed in the buffer during irradiation. Moreover, the stress state inside the buffer is expected to be heterogeneous since the buffer microstructure and the related mechanical properties are also heterogeneous [6].

AGR-1 [21] examined 981 particles, 61.1% showed full buffer-IPyC debonding, while 33.5% exposed partial debonding, and 5.4% had no debonding. In AGR-2 [22], 538 particles were examined; 60% exhibited full debonding, 40% partial, and only one particle held no buffer-IPyC debonding. These results manifested similar rates of buffer fracture, 23% and 20%, in AGR-1 and AGR-2, respectively, yet fewer IPyC fractures in AGR-2. The statistics of buffer tearing of AGR-1 and AGR-2 particles implies the significant effect of the spatial heterogeneity of buffer microstructure, i.e., the porosity effects.

In AGR-2 [22], The UCO-based kernels show higher occurrences of fracture in the buffer layer than the UO₂-based, as seen in Figure 18. The factors contributing to this observation are not explicit but the differences in radiation-induced kernel swelling rates between UO₂ and UCO might be one of the reasons due to the higher burnup in the UCO-based fuel.

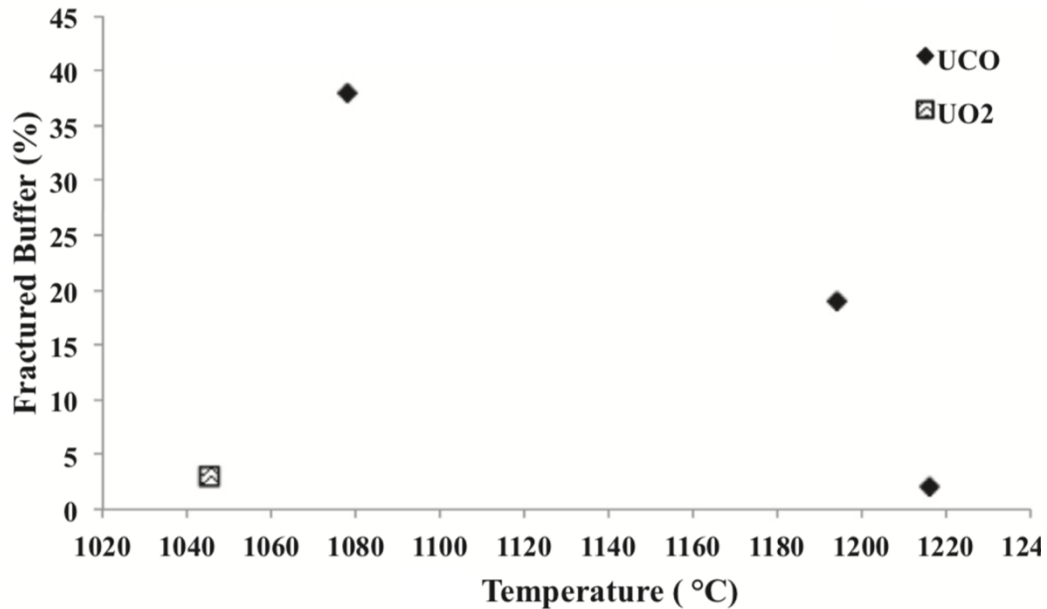






Figure 18 The frequent occurrence of fracture in buffer layers for UCO and UO₂-based fuel as reported by the AGR-2 [22].

Surprisingly, In AGR-2, Figure 19 shows a more significant occurrence of buffer fractures in the bottom half of the fuel cross-section. These exciting outcomes could be due to a temperature gradient within the fuel particle during irradiation. The thermal analyses of the AGR-2 irradiation experiment indicate that radial temperature gradients could exceed 100 °C, and axial gradients may come closer to 300 °C. These multiple dimensions of heterogeneity and complexity make it a tremendous challenge to fully understand the buffer fracture mechanisms.

ABf	
Af	
ABi	
Ai	

Ai: Densification radially inward and intact
Af: Densification inward and fractured

ABi: Densification inward and intact with localized bonding to IPyC
ABf: Densification inward with fractures in non-bonded regions

Bi: Outward densification and intact buffer
Bf: Outward densification, fractured buffer

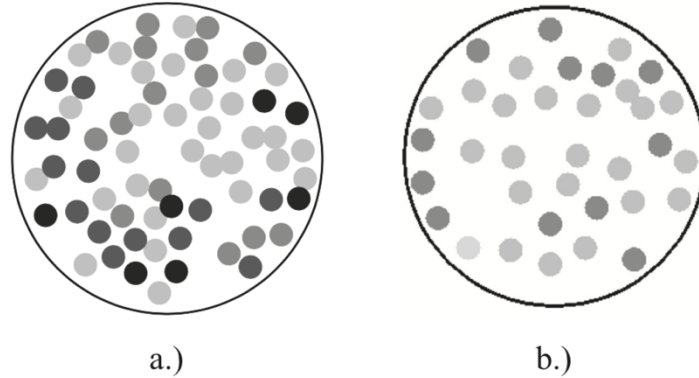


Figure 19 Color-coded events of buffer fracture occurred in (a) UCO-based and (b) UO₂-based TRISO particle as reported in AGR-2 [22].

After thoroughly analyzing the statistics of TRISO behaviors reported in AGR-1 and AGR-2 experiments [20 – 22], we had a collaboration with two experimental groups from University of Wisconsin (Yongfeng Zhang, Ramathan Thevamaran, Kumar Sridharan, and Claire Griesbach) and Oak Ridge National Laboratory (Tyler Gerczak) to obtain high-resolution volumetric data of the buffer layer porous microstructure. See Figure 20 for the University of Wisconsin TRISO Particle SEM images. To analysis this experiment, a deep learning model was built and trained using the experimental data set and applied to the whole image stack.

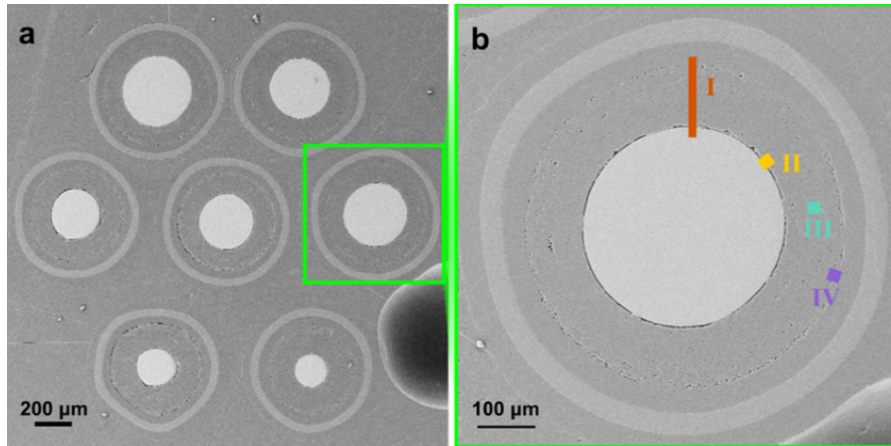


Figure 20 University of Wisconsin TRISO Particles SEM analysis: a) hexagonal array of polished TRISO particles, b) Slice and View of TRISO particle, with various investigated regions denoted by I, II, III, and IV.

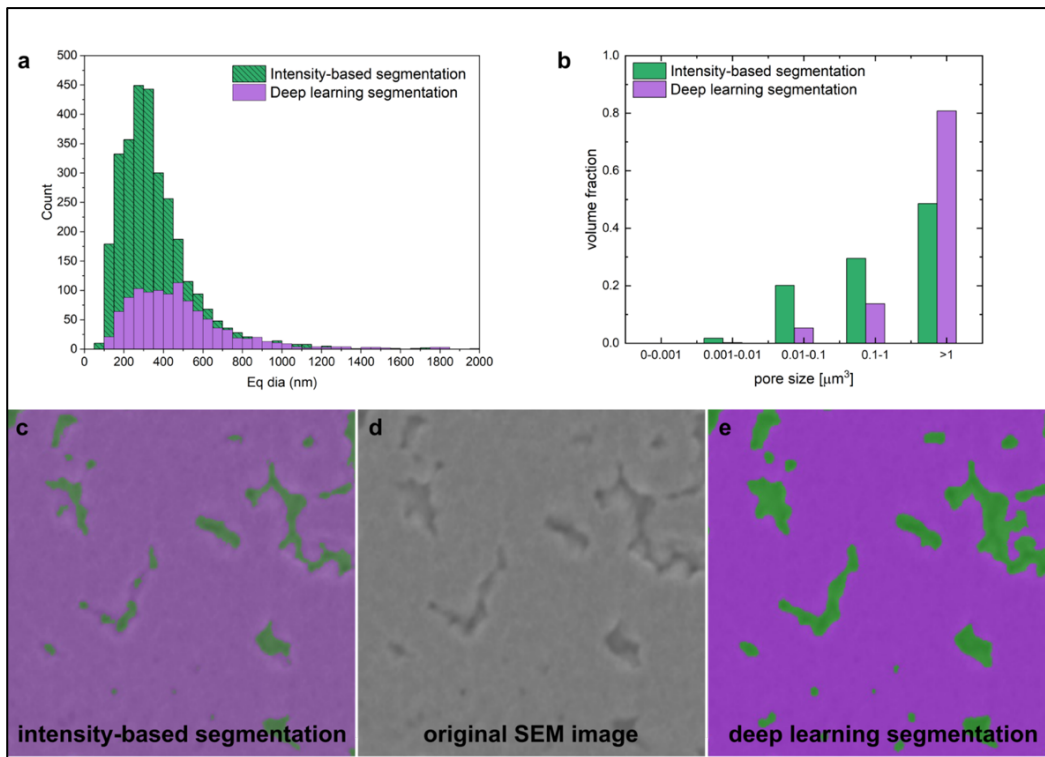


Figure 21 University of Wisconsin image processing and data analysis: a) distribution of pore sizes resulting from intensity-based segmentation and deep learning segmentation methods, b) volume fractions of pore volume ranges resulting from the two segmentation methods, c) example of intensity-based segmentation result (pores – green, buffer – purple), d) unsegmented SEM image, e) example of deep learning segmentation result.

Large differences are apparent in the porosity quantification data resulting from the two segmentation methods. Looking at the segmentation results in an example area Figure 21 (c-e), the deep learning segmentation method clearly does a better job at capturing the entire pore area, regardless of contrast changes within the pore. These differences propagate into the volumetric porosity data: the number and volume fraction of small pores are significantly higher for the intensity-based segmentation, Figure 21 (a, b) because large pores are artificially broken into smaller pores due to contrast gradients within the pore. The total volume fraction of pores is also much lower for the intensity-based segmentation (10.8%) than the deep learning segmentation (19.3%). This is due to regions within large pores being misidentified as the buffer. Through this analysis, the UW team have determined that the deep learning segmentation method will be more consistent and accurate in characterizing the porosity in their data sets.

After carefully studying the results from AGR-1 & AGR-2 experiments [20 – 22] and the insights from our collaborators' experiments, as seen above, we designed our mesoscale investigations, presented in this work, to understand the fundamental influences of the pores microstructure on building up the stresses that later lead to fracture in the buffer layer to utilize the TRISO fuel better. In this work, we are focusing on five critical factors of porosity microstructure, the size, shape, number density, spatial distribution, and volume fractions. Understanding the effect of these factors on the buffer fracture would answer many fundamental concerns about buffer fracture behavior. To that aim, the Phase-field fracture model developed by this work was first utilized to simulate the stress evolutions (later the fracture) in nuclear-grade graphite due to the porosity microstructure

heterogeneity. Similar approaches have been applied to determine the fracture stress of porous polycrystalline UO_2 [24] and nuclear-grade graphite [23]. Later the same procedure will be applied for the TRISO-buffer layer by tuning the corresponding material parameters. As mentioned earlier, for the first time, this work novel model defined the porosity as a phase-field variable and represented the fracture with other phase-field order-parameter. This is a significant improvement compared to the other models in the literature that usually use an external mesh with a pre-defined porosity.

CHAPTER III

PHASE FIELD MODEL DEVELOPMENT

The phase-field [14 – 16] is a fundamental approach that has been utilized widely by the computational materials science and engineering community to investigate various microstructure evolutions, such as solidification, grain growth, and phase transformations [64 – 68]. Since 2009, the phase-field has been adopted in the nuclear materials community; successfully simulates the irradiation effects [69 – 71]. This work developed a Novel Multiphysics Mesoscale model that could predict the fracture in nuclear fuel by utilizing the phase-field modeling of fracture [24, 28 – 29, 72]. The phase field modeling of fracture shows the right prediction of the propagation of a pre-existing crack according to Griffith' criterion [54]. This work model was utilized to simulate the thermal shock-induced fracture in UO_2 and the fracture behavior in the Nuclear-grade graphite (later, the TRISO buffer layer) due to the change in porosity microstructures. In Section 3.1, we modified the phase-field models of fracture presented in literature [24, 28 – 29], and coupled the revised version to the heat conduction model to simulate the fracture in UO_2 due to thermal shock. The Novel Formation of the model to simulate the concurrent microstructure evolution with fracture formation, for the first time, is detailed in Section 3.2. The model Novel formations were validated analytically and tested against previous INL work for nuclear-grade graphite. In comparison with other phase-field modeling of fracture [24, 28 – 29], which usually utilize an external mesh with a pre-defined porosity, our new method permits investigating microstructure changes and their effects on fracture behavior concurrently. On the one hand, the crack might be blunt due to the pores

interactions resulting in the material's toughness enhancement. On the other hand, the material will be less stiff or weaker due to increased pores volume fraction. This work Novel model would resolve the mystery behind this complicated behaviors that are yet to be understood [24 – 27].

As mentioned earlier, the attempts to model fracture started a ~100-years ago by Griffith [5] who states that “*crack growth will occur, when there is enough energy available to generate new crack surfaces*”, see Eq 3.1. later, Irwin in 1948 [6] extended the theory to the stress criterion and introduced the Stress Intensity Factor (SIF). Many years later, Francfort and Marigo [41] devolved a variational interpretation and introduced an energy functional that contains the displacement field and unknown crack field ($E(\mathbf{u}, \Gamma_{crack})$), see Eq 3.2. The minimization of this $E(\mathbf{u}, \Gamma_{crack})$ will be equivalent to Griffith’s problem. But this formula (Eq 3.2) is very hard to treat, since Γ itself is unknown. A major step forward came in the year of 2000, when Bourdin et al. [42] introduced a regularization process similar to the image processing technique presented by Mumford and J. Shah in 1989 [73]. Thus, instead of having a discrete crack field (Eq 3.2, and Figure 23.a) we ended-up by a continuous crack field (Eq 3.3, and Figure 23.b). Note that, the regularization technique utilized in Eq 3.3 was first introduced by Ambrosio and Tortorelli in 1990 [74]. It worth noting that, comparing with Eq 3.2, the integration in Eq 3.3 is a volume integral thus an introduction of a new length scale (l) is mandate. Note that, once $l \xrightarrow{tends} 0$, Eq 3.3 turns to Eq 3.1, Griffith work. This numerical length scale (l) in the

gradient damage/phase-field models is related to the material length scale and might be not only a purely numerical parameter such that $(l = \frac{K_{Ic}^2}{\sigma_c^2})$.

$$\mathcal{G}_c = -\frac{\partial \psi}{\partial a} = \frac{\partial S}{\partial a} \quad \text{Eq 3.1}$$

$$F(\mathbf{u}, \Gamma_{crack}) = \int_{\Omega} \psi(\epsilon(\mathbf{u})) dx + \mathcal{G}_c \int_{\Gamma} d\Gamma \quad \text{Eq 3.2}$$

$$F(\mathbf{u}, \eta_d) = \int_{\Omega} g(\eta_d) \psi(\epsilon(\mathbf{u})) dx + \mathcal{G}_c \int_{\Omega} \frac{1}{2l} (\eta_d^2 + l^2 |\nabla \eta_d|^2) d\Omega, \quad 0 \leq \eta_d \leq 1 \quad \text{Eq 3.3}$$

Where, \mathcal{G}_c is the fracture energy (material parameter), and $\frac{\partial \psi}{\partial a}$ is the energy release with existing crack (a), while the $\frac{\partial S}{\partial a}$ is the energy consumption to create a new surface. The displacement field is denoted by (\mathbf{u}) , strain energy by (ϵ) , while (Ω) and (Γ) are the volume and crack surface, respectively, see Figure 23 for more illustration of Ω and Γ . Note that, $g(\eta_d)$ is the degradation function. To make sure that the crack will happen under tension not compression, the strain energy $\psi(\epsilon(\mathbf{u}))$ splits into $\psi(\epsilon(\mathbf{u}))^+$ and $\psi(\epsilon(\mathbf{u}))^-$; only the $\psi(\epsilon(\mathbf{u}))^+$ part introduced to the degradation function $g(\eta_d)$, this method was first introduced by Amor et al. in 2009 [75] and Miehe et al. [28 – 29].

3.1 Phase-Field modeling of fracture due to thermal shock in UO_2^3

The UO_2 is a fluorite ceramic structure, thus holding a cubic elastic symmetry. This part of the model modified the phase-field models fracture presented in literature [24, 28 – 29], and coupled the revised version to the heat conduction model to simulate the fracture in UO_2 due to thermal shock. Here, our model decomposes the strain energy into two parts, one contributes to fracture (tensile, ψ_{elastic}^+), and the other (compression, ψ_{elastic}^-) does not, similar to [28 – 29, 75]. To do so, we chose the strain spectral decomposition method, introduced by Miehe et al. [28 – 29], rather than various decomposition methods [76 – 77] due to the better performance for brittle materials [24]. To keep this simple, we refer the reader to [24] for more details about the strain spectral decomposition scheme. Consequently, in this model, the elastic energy will be released in a fracture energy manner, as:

$$F_{\text{total}} = \Psi_{\text{elastic}} - \Psi_{\text{external}} + \Psi_{\text{fracture}} \quad \text{Eq 3.4}$$

$$F_{\text{total}} = \Psi_{\text{elastic}} - \Psi_{\text{external}} + \mathcal{G}_c \int_{\Omega} \gamma_{\text{crack}} \, d\Omega \quad \text{Eq 3.5}$$

Where, Ω is the system domain, \mathcal{G}_c the critical energy release rate, γ_{crack} is a geometrical discontinuous function to represent the crack topology, in which $\gamma_{\text{crack}} = 1$ represent a fully crack surface, and $\gamma_{\text{crack}} = 0$ means an intact materials zone. Note that, here we ignored the interfacial energy (f_{int}) since we used a pre-defined mesh in this case

³ Reprinted with permission from Elsevier "Experimentally validated Multiphysics modeling of fracture induced by thermal shocks in Sintered UO_2 Pellets" by L. D. McClenny, M. I. Butt, M. Goma Abdoelatef, M. J. Pate, K. L. Yee, R. Harikrishnan, D. Perez-Nunez, W. Jiang, L. H. Ortega, S. M. McDevitt and K. Ahmed, 2022. , Journal of Nuclear Materials. Copyright [2022] by Journal of Nuclear Materials.

similar to [24]. But this is not a model limitation, and the contribution of the interfacial free energy due to the crack interaction with grain boundaries, second phase particles, and various microstructure evolutions is summarized in the following subsection. Here, we utilized the order parameter (η_d), $\eta_d \in [0,1]$ to smooth this function, such that:

$$\gamma_{\text{crack}} \approx \gamma(\eta_d; l) = \frac{1}{2l} (\eta_d^2 + l^2 |\nabla \eta_d|^2) \quad \text{Eq 3.6}$$

$$\lim_{l \rightarrow 0} \gamma(\eta_d; l) = \gamma_{\text{crack}} \quad \text{Eq 3.7}$$

Here, l is the model length-scale that ensures the diffusion of the crack width. To smooth this discontinuous function (γ_{crack}), the so-called degradation function is usually applied to the elastic energy in a way that Eq. 5 would be modified as:

$$F_{\text{total}} = \Psi_{\text{elastic}} - \Psi_{\text{external}} + \mathcal{G}_c \int_{\Omega} \frac{1}{2l} (\eta_d^2 + l^2 |\nabla \eta_d|^2) d\Omega \quad \text{Eq 3.8a}$$

$$F_{\text{total}} = \int_{\Omega} \psi_{\text{elastic}} d\Omega - \int_{\partial\Omega} \psi_{\text{external}} d\Gamma + \mathcal{G}_c \int_{\Omega} \frac{1}{2l} (\eta_d^2 + l^2 |\nabla \eta_d|^2) d\Omega \quad \text{Eq 3.8b}$$

$$F_{\text{total}} = \int_{\Omega} g(\eta_d) \psi_{\text{elastic}}^+ d\Omega + \int_{\Omega} \psi_{\text{elastic}}^- d\Omega + \mathcal{G}_c \int_{\Omega} \frac{1}{2l} (\eta_d^2 + l^2 |\nabla \eta_d|^2) d\Omega \quad \text{Eq 3.8c}$$

Where, Γ_{crack} is the crack set. $g(\eta_d)$ is the degradation function that works to degrade the elastic energy based on the local order parameter. In literature, there are many ways to form this degradation function, here, we used the type of degradation function similar to [24], thus:

$$g(\eta_d) = (1 - \eta_d)^2 (1 - k) + k \quad \text{Eq 3.9}$$

To avoid any numerical issues, we introduced a very small value to k , closer to zero ($k \approx 10^{-6}$); then $g(0) = 1$, and $g(1) = 0$. The total stress in damaged material is defined as:

$$\boldsymbol{\sigma} = \frac{\partial F_{total}}{\partial \boldsymbol{\epsilon}} = ((1 - \eta_d)^2(1 - k) + k) \frac{\partial \psi^+}{\partial \boldsymbol{\epsilon}} + \frac{\partial \psi^-}{\partial \boldsymbol{\epsilon}} = ((1 - \eta_d)^2(1 - k) + k) \boldsymbol{\sigma}^+ + \boldsymbol{\sigma}^- \quad \text{Eq 3.10}$$

Here, we assumed a linear elastic material response of the brittle fracture of UO_2 , thus the strain tensor ($\boldsymbol{\epsilon}$) is defined, in terms of displacement vector (\mathbf{u}), as:

$$\boldsymbol{\epsilon} = \frac{1}{2} (\nabla \mathbf{u} + \nabla \mathbf{u}^T) \quad \text{Eq 3.11}$$

And the stress tensor would be generally expressed as:

$$\boldsymbol{\sigma}_0 = \mathbb{C} \boldsymbol{\epsilon}, \quad \text{Eq 3.12}$$

where \mathbb{C} is the fourth-order elasticity tensor. In this work we assumed a quasi-static system, therefore the equilibrium equations can be obtained by taking the variations of the total internal energy F_{total} , then:

$$\nabla \cdot [((1 - \eta_d)^2 + k) \boldsymbol{\sigma}^+ + \boldsymbol{\sigma}^-] = \mathbf{0} \quad \text{Eq 3.13}$$

Where $\boldsymbol{\sigma}^+$ and $\boldsymbol{\sigma}^-$ are the Cauchy stress as described by [24]. Also, the damage variable field (η_d) evolves to minimize the total free energy of the system according to the famous Allen-Cahn equation, thus:

$$\frac{\partial \eta_d}{\partial t} = -L \frac{\delta F}{\delta \eta_d} = -L \left(-2(1 - \eta_d) H_0^+ + \frac{G_c}{l} \eta_d - G_c l V^2 \eta_d \right) \quad \text{Eq 3.14}$$

L is mobility and H_0^+ is a history variable to prevent the crack healing. More detail on the strain–history functional can be found in Miehe et al. [28 – 29] and Wen et al. [24].

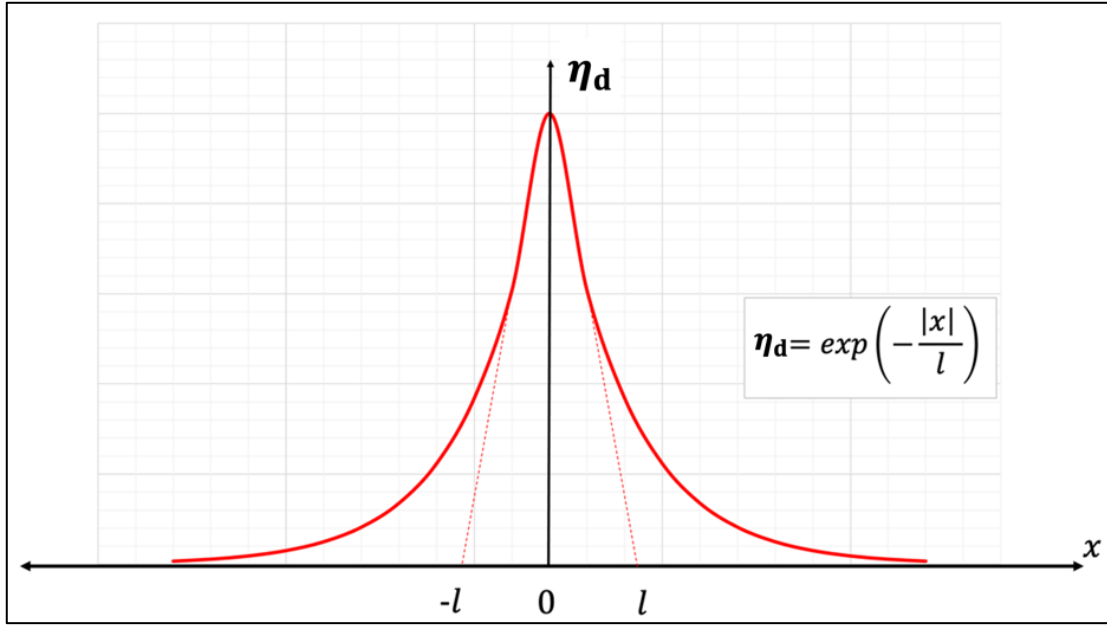


Figure 22 The Phase-field damage variable (c) spatial distribution in 1D

It is worth noting that, a 1-D analysis of the above governing equations predicts the order parameter (η_d) profile as seen in Eq 3.15; this damage profile is presented in Figure 22 for more illustrations.

$$\eta_d = \exp\left(-\frac{|x|}{l}\right) \quad \text{for } -\infty < x < \infty \quad \text{Eq 3.15}$$

In this case analysis, the stress develops and evolves due to the thermal shock. Therefore, we coupled the phase-field fracture model with the heat conduction equation so that the model could simulate the fracture due to thermo-mechanical loading. The temperature variations are the key factors during the thermal sock analysis. The heat conduction was modeled as:

$$k_0 \nabla \cdot \nabla T - \rho C_p \dot{T} + Q = 0 \quad \text{Eq 3.16}$$

where, k_0 denoting the thermal conductivity, T is the temperature, C_p is the heat capacity, ρ is density, and Q is the heat source. The internal stress due to the temperature variations is entirely dependent on the thermal expansion of the system. Thus, the stress tensor (σ_0) will be redefined, and Eq 3.12 will be modified to be:

$$\boldsymbol{\sigma}_0 = \mathbb{C}(\boldsymbol{\epsilon} - \boldsymbol{\alpha}\mathbf{I}(T - T_0)) \quad \text{Eq 3.17}$$

Where, \mathbb{C} and $\boldsymbol{\epsilon}$ are the aforementioned fourth-order elasticity tensor and the strain tensor, respectively. $\boldsymbol{\alpha}$ is denoting the thermal expansion coefficient while T_0 is referring to the reference temperature. Finally, Eqs 3.13-17 are this case modeling governing equations and they were solved simultaneously using the finite element method implemented in the MOOSE framework [78].

3.2 A novel formulation of phase-field modeling to simulate the co-formation of fracture and heterogenous microstructure evolutions.

Most of the phase-field model in literature treating the crack degradation of elastic moduli and hence stress and energy as an elastic heterogeneity like voids [24, 28 – 29, 72]. This way is equivalent to phase-field models of rafting [79 – 80]. In this work novel formulation, we introduced the damage strain in a way equivalent to the introduction of transformation/Eigen strain. This approach is equivalent to how the phase-field treats all types of inclusions or precipitates in classical phase transformations [81 – 83]. It is worth noting that, recently, Han et al. [84] utilized the elastic and plastic strain energies as a driving force to sustain damage evolution for ductile fracture simulations for elastoplastic materials. A recent intensive study for the mechanical and energy properties for the phase-field modeling of fracture was carried out by Yu et al. [85]. These studies struggled with the elastic limit stress; shows a nonlinear change in the stress-strain curves even at the beginning of loading. Tanné et al. [54] examined the crack nucleation in brittle fracture using the variational phase-field models; they illustrated that crack nucleation can be accurately anticipated by minimization of the nonlinear energy and does not require any ad-hoc criteria.

So, with that being said and all things considered– this work employed the phase-field modeling of fracture to simulate the cracks formations and evolutions processes in nuclear fuels. Our model provides a holistic description of the interactions processes of cracks (η_d), the intact region or the Matrix (η_M), and the second-phase particles (η_p). While the notation (c) described the atom concentration of the second phase particle; will

evolve based on the famous Cahn-Hilliard [86], see Figure 23c for better illustrations. Intuitively, our new constitutive equations were developed based on the second law of thermodynamics. In these novel formulations, the total free energy per unit volume is the sum of , elastic strain density, fracture, interfacial, and chemical energies, as:

$$F_{Total} = \Psi_{elastic} - \Psi_{external} + \Psi_{fracture} + f_{interfacial} + f_{chemical} \quad \text{Eq 3.18}$$

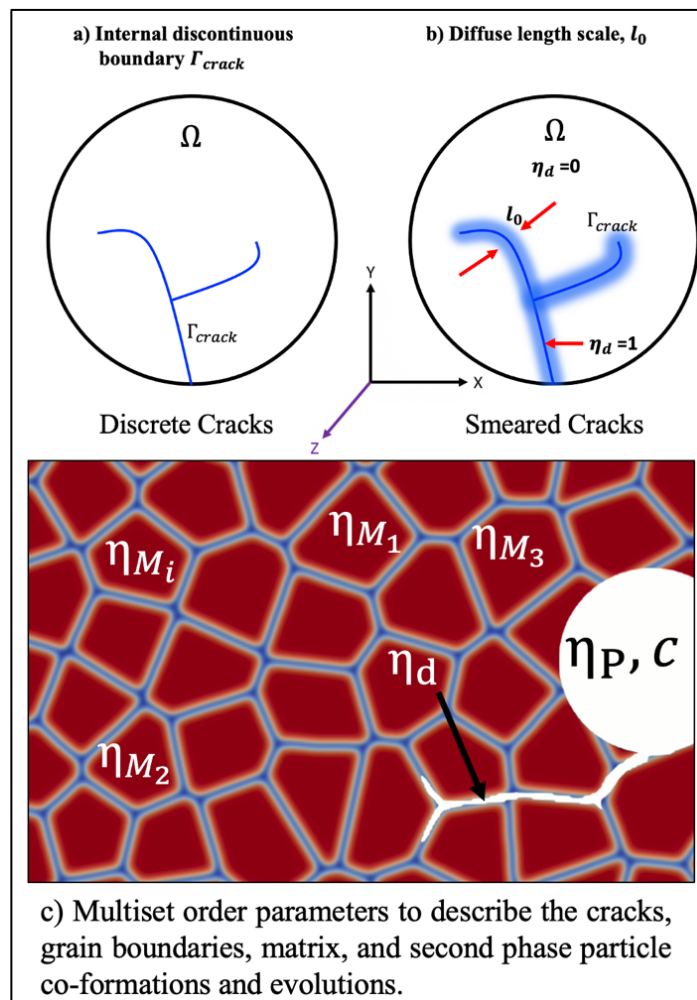


Figure 23 Schematic illustration of this work phase-field approach for modeling nuclear fuel pellet cracking. $\eta_d = 1$ indicating fully damaged state and $\eta_d = 0$ intact state.

Multi set of phase-field order parameters were used to differentiate between the cracked region (η_d), intact matrix (η_M), and the second-phase particles (η_p), see Figure 24c. The fracture kinetics were obtained by solving the evolution equations of the damage order parameter (η_d), Allen-Cahn [87], while the second phase concentration order parameter (c) is evolved based on the Cahn-Hilliard equation [86].

Qualitatively, this model simulates the formations of damaged regions similar to the heterogeneous phase transformation modeling as illustrated by Abdoelatef et al. [12]. These new order parameters and the corresponding distinct phases (damaged region, intact matrix, and the second-phase particle) were illustrated in Figure 24. For all mentioned order parameters, they are equal to 1 inside the related phase, and = 0 everywhere else.

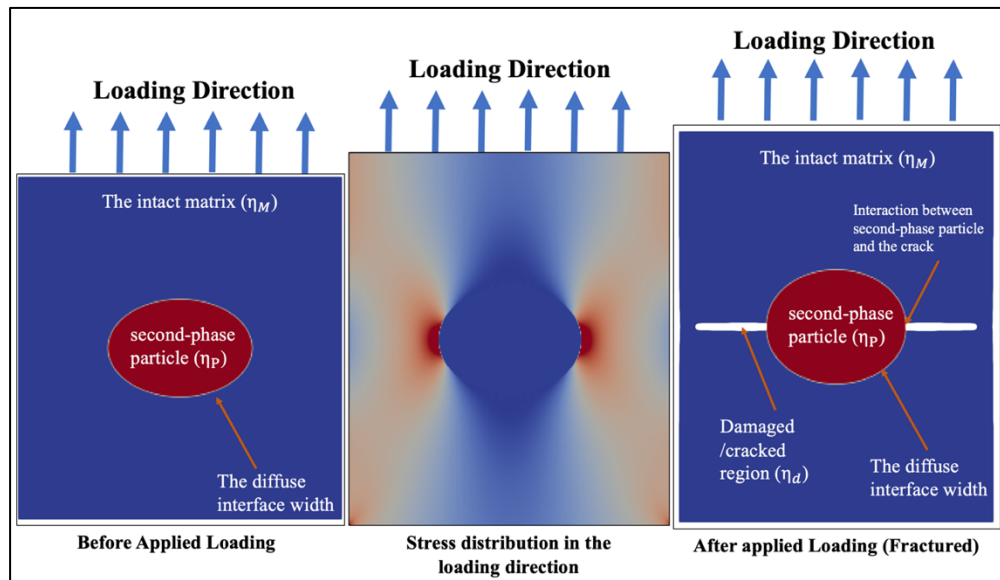


Figure 24 An illustration of the novel phase-field variables used to describe the fracture microstructure. For left and right screenshots, the second phase particle is shown in red, the intact matrix in blue, while the crack or the damaged regions are presented in white. The middle screenshot shows the stress distributions on the loading direction (Y-axis); note that the red color is the high-stress regions while the blue refers to the less-stress areas (in middle screenshot).

This model free energy functional (F_{Total}), that simulates the co-formations of fracture and microstructure evolution, is combined of elastic energy ($\Psi_{elastic}$), external ($\Psi_{external}$), fracture, interfacial (f_{int}) and the thermodynamic chemical ($f_{chemical}$) free energies and constructed as:

$$F_{Total} = \int \left(\begin{array}{l} \Psi_{elastic}(\eta_d, c, \eta_P, \eta_{Mi}) - \Psi_{external} + G_c \frac{1}{2l} (\eta_d^2 + l^2 |\nabla \eta_d|^2) + \\ f_{int}(\eta_{Mi}, \eta_P, \eta_d, \nabla \eta_{Mi}, \nabla \eta_P, \nabla \eta_d) + \\ f_{chemical}(\eta_d, \eta_{Mi}, \eta_P, c) \end{array} \right) dv \quad \text{Eq 3.19}$$

$$f_{int}(\eta_{Mi}, \eta_P, \eta_d, \nabla \eta_{Mi}, \nabla \eta_P, \nabla \eta_d) =$$

$$A \left[\begin{array}{l} 0.25 + 0.25(\sum_i \eta_{Mi}^4 + \eta_P^4 + \eta_d^4) - 0.5(\sum_i \eta_{Mi}^2 + \eta_P^2 + \eta_d^2) \\ + \gamma_M \sum_i \sum_{j>i} \eta_{Mj}^2 \eta_{Mi}^2 + \gamma_{M,d} \eta_d^2 \sum_i \eta_{Mi}^2 \\ + \gamma_P \eta_P^2 (\sum_i \eta_{Mi}^2 + \eta_d^2) + \gamma_d \eta_d^2 (\sum_i \eta_{Mi}^2 + \eta_P^2) \\ + \frac{k_M}{2} (\sum_i |\nabla \eta_{Mi}|^2) + \left(\frac{k_P}{2}\right) \times (|\nabla \eta_P|^2) \end{array} \right] \quad \text{Eq 3.19a}$$

Here, k_M , k_P are the gradient energy coefficients for the matrix and the second-phase particles, respectively. For simplicity, in this work simulations, k_M , and k_P is having the same values ($k_M = k_P = K$). Here, (γ_M), (γ_d) and (γ_P) are the interfacial energies of the intact, the damaged regions, and the second phase particle respectively. ($\gamma_{M,d}$) is the interfacial energy between the matrix and the crack.

In order to define the model chemical free energy, we started by integrating the chemical potential (which is a function of the second-phase particles concentration and the phase-field variables) with respect to the concentration, as follow:

$$\frac{\partial f^{ch}}{\partial c} = \mu(\eta_{Mi}, \eta_P, c) \quad \text{Eq 3.20}$$

Here, we assumed the chemical free energies to have a parabolic relation with respect to the concentration; to do that we formulated the solute concentration (c) as a function of

equilibrium gas concentration (c^{eq}), phase-field variables and the chemical potential (μ).

This expression could be described as follow:

$$c = c^{eq}(\eta_M, \eta_P) + \mu \left[\frac{h_M(\eta_M, \eta_P)}{\epsilon_M} + \frac{h_P(\eta_M, \eta_P)}{\epsilon_P} \right] \quad \text{Eq 3.21}$$

Here, $h_P(\eta_M, \eta_P)$ stands for the second-phase particles fraction, where,

$$[h_M(\eta_M, \eta_P) + h_P(\eta_M, \eta_P)] = 1 \quad \text{Eq 3.22}$$

(ϵ_M), and (ϵ_P) are the free energies parabolic curvatures for the matrix, and the second-phase particles, respectively. The equilibrium concentration of the second-phase particles (c^{eq}) expressed as:

$$c^{eq}(\eta_M, \eta_P) = h_M(\eta_M, \eta_P)c^M + h_P(\eta_M, \eta_P)c^P \quad \text{Eq 3.23}$$

Where, c^M and c^P , are the concentrations in the matrix and the second-phase particles respectively.

By rearrangement the equation 3.20, the chemical potential can be expressed as:

$$\mu(\eta_M, \eta_P, c) = \frac{c - c^{eq}(\eta_M, \eta_P, c)}{\left[\frac{h_M(\eta_M, \eta_P, c)}{\epsilon_M} + \frac{h_P(\eta_M, \eta_P, c)}{\epsilon_P} \right]} \quad \text{Eq 3.24}$$

Thus, the chemical free energy formulated as:

$$f^{ch}(\mu, \eta_M, \eta_P, c) = \frac{[c - c^{eq}(\eta_M, \eta_P, c)]^2}{2\chi \left[\frac{h_M(\eta_M, \eta_P, c)}{\epsilon_M} + \frac{h_P(\eta_M, \eta_P, c)}{\epsilon_P} \right]}, \quad h_p(\eta_M, \eta_P) = \frac{\eta_p^2}{\sum_i \eta_{M_i}^2 + \eta_p^2} \quad \text{Eq 3.25}$$

This chemical free energy form prevents any dependency between the chemical free energy and the interfacial energy.

The generic strain energy density formulated as:

$$\Psi_{\text{elastic}}(c, \eta_p, \eta_d, \eta_{Mi}) = g(\eta_d)\psi_{\text{elastic}}^+ + \psi_{\text{elastic}}^- + Q(\eta_p) + R(\eta_M, \eta_p) \quad \text{Eq 3.26}$$

$$Q(\eta_p) = \frac{1}{2} E \epsilon^2 (\eta_p^3 * (6 \eta_p^2 - 15 \eta_p + 10)) \quad \text{Eq 3.26a}$$

$$R(\eta_M, \eta_p) = \frac{\sum_i \eta_{Mi}^2}{\sum_i \eta_{Mi}^2 + \eta_p^2} \left(\frac{1}{2} G b^2 \right) \rho \quad \text{Eq 3.36b}$$

Here, the first two-terms represent the strain energy of fracture, as discussed in Section 3.1. $Q(\eta_d)$ is the Strain energy associated with the heterogenous microstructure (e.g., matrix and second-phase particle), E is the Young's modulus, and ϵ is the strain. The fourth term, $R(\eta_M, \eta_p)$, is the strain energy associated with dislocation density, where G , and b are the shear modulus and the Burgers vector. while ρ is the dislocation density that utilized to investigate the effects of the non-uniform dislocation density. It worth noting that the model results presented in this work didn't employ $R(\eta_M, \eta_p)$ but this is not a model limitation, and the irradiation effect could be simulated similar to the author earlier work in a high burn-up structure modeling [12]. Moreover, the model can be coupled to the rate theory model [88] to account for the stress evolutions due to the irradiation effect.

3.2.1 The Novel Model's evolution equations

The entire cracking and microstructure co-evolution process is obtained implicitly by solving the coupled system of Allen-Cahn [87] and Cahn-Hilliard [86] diffusion equations along with the principles of irreversible thermodynamics [89]. Thus, this model order parameters evolves as follow:

$$\frac{\partial \eta_d}{\partial t} = -L \frac{\delta F}{\delta \eta_d} = -L \left(-2(1 - \eta_d)H_0^+ + \frac{G_c}{l} \eta_d - G_c l \nabla^2 \eta_d \right) \quad \text{Eq 3.27}$$

Where, H_0^+ is the maximum elastic energy as discussed in Section 3.1

Thus:

$$\begin{cases} \frac{\partial \eta_d}{\partial t} = -L_d \frac{\delta F}{\delta \eta_d} = -L_d \left(\frac{\partial f^{\text{int}}}{\partial \eta_d} + \frac{\partial f^{\text{ch}}}{\partial \eta_d} - 2(1 - \eta_d)H_0^+ + \frac{G_c}{l} \eta_d - G_c l \nabla^2 \eta_d \right) + \xi_d \\ \frac{\partial \eta_p}{\partial t} = -L_p \frac{\delta F}{\delta \eta_p} = -L_p \left(\frac{\partial f^{\text{int}}}{\partial \eta_p} + \frac{\partial f^{\text{ch}}}{\partial \eta_p} - 2(1 - \eta_d)H_0^+ + \frac{G_c}{l} \eta_d - G_c l \nabla^2 \eta_d \right) + \xi_p \\ \frac{\partial \eta_{M_i}}{\partial t} = -L_{M_i} \frac{\delta F}{\delta \eta_{M_i}} = -L_{M_i} \left(\frac{\partial f^{\text{int}}}{\partial \eta_{M_i}} + \frac{\partial f^{\text{ch}}}{\partial \eta_{M_i}} - 2(1 - \eta_d)H_0^+ + \frac{G_c}{l} \eta_d - G_c l \nabla^2 \eta_d \right) \quad \forall i \end{cases}$$

Where, the L_d and L_p are constants related to the damage, and the second-phase particles surface mobilities, respectively. The L_{M_i} is the constant related to the boundary mobility of the matrix. Generally, ξ_α is a stochastic term that facilitate the nucleation of the α -phase. These stochastic terms allow the model to examine other proper paths of evolution within the region of the likely paths in the phase/state space. Notably, in this model, we conducted constant mobility coefficients that are similar to postulate isotropic grain boundaries and second-phase particles surface mobilities. This is not a model limitation since the anisotropic state could be simulated by using the similar approaches applied by the solidification and the grain growth models [89 – 91].

The solute atoms concentrations (or the conserved density field) are evolving according to the Cahn-Hilliard equation [86], e.g.:

$$\frac{\partial c}{\partial t} = \nabla \cdot (M \nabla \mu) + P + \xi_c , \quad \text{Eq 3.28}$$

$$\mu = \frac{\delta F}{\delta c} = \frac{\partial f^{ch}}{\partial c} . \quad \text{Eq 3.29}$$

where, M is the chemical mobility of solute atoms, μ is the gas atoms chemical potential, P is a general term that describes the progress of solute atoms productions due to the deformation (e.g., mechanical deformation, or the irradiation damage), and ξ_c is a stochastic term like the other stochastic terms described above that allows the production of a second phase particles (i.e., bubbles in case of irradiation damage). While the chemical mobility (M) is related to the materials property, therefore it has a direct relation to the diffusivity (D), this relation can be formed as:

$$\frac{\partial^2 f^{ch}}{\partial c^2} M = D \quad \text{Eq 3.30}$$

For the sake of simplicity, the bulk diffusion mechanism was considered to be the only scheme for the gas atoms diffusion. Therefore, the model employed a constant mobility. This is not a model limitation since the other diffusion mechanisms, such as the grain boundary and surface diffusion, can be combined with the model as in the work of the grain growth in porous solids by Ahmed. et al. [92 – 93]

CHAPTER IV

RESULTS AND DISCUSSION

The main objective of this section is to illustrate the model capacities in simulating the near-real cracking phenomena in different nuclear fuels and validating the model results against the conceptual theories and experimental data. We conducted a few test cases in the following subsections to benchmark the model capabilities. Indeed, these theoretical test cases demonstrate the right implementation of the model and the related parameters. Moreover, the model was utilized to simulate the fracture behavior in UO_2 due to thermal shock and validated against our experimental measurements. Notably, We introduced a new combined experimental and computational approach to investigate thermal shock-induced fracture in UO_2 pellets. In contrast to other fracture modeling techniques, our model that employs a phase-field fracture approach can predict the crack nucleation site, growth rate, crack path, size, and morphology given the values of the fracture properties of the material of interest.

The model further enhanced and employed multiset order parameters to capture the complicated interaction between the cracking and nuclear materials' heterogeneous microstructure. Indeed, this is the first time in the computational nuclear materials field to simulate the formation and evolution of cracking and a second phase particle coalescence concurrently. In contrast with other models in the literature that usually use external meshes with pre-defined holes (that will never evolve), our model captured such complicated phenomena because it utilizes a multiset of phase-field order parameters to describe these heterogeneities. These novel capabilities of our model were also validated

against nuclear-grade graphite data and later will be implemented to study the TRISO buffer layer. Notably, the model captured different nuclear materials' cracking kinetics, size, and path morphologies and the effect of the second phase particle sizes, shape, volume fraction, and distribution on the cracking behavior and the related mechanical properties.

4.1 Benchmarking Test Cases

Here, we carried out various 2D test cases to benchmark the model capabilities. We started by testing the model against theoretical elliptical cavity predictions, followed by a quantitative examination of the effect of domain structure and the presence of the crack. Also, the model examines the impact of second phase particle shape, size, and volume fraction on the stress distribution and the cracking behavior. Finally, the model was benchmarked against the nuclear grade graphite data in the literature. The model could successfully capture the well-known theoretical aspects.

4.1.1 An elliptical cavity in an infinite domain

Griffith [5] implied that the difference between the true strengths of brittle materials and theoretical calculations was due to the existence of flaws inside the materials. Moreover, the fracture will never happen unless the stress at the atomic level exceeds the material's cohesive strength [94]. Thus, the flaws must reduce the overall material's strength by enhancing/increasing the stress locally (at the crack tip).

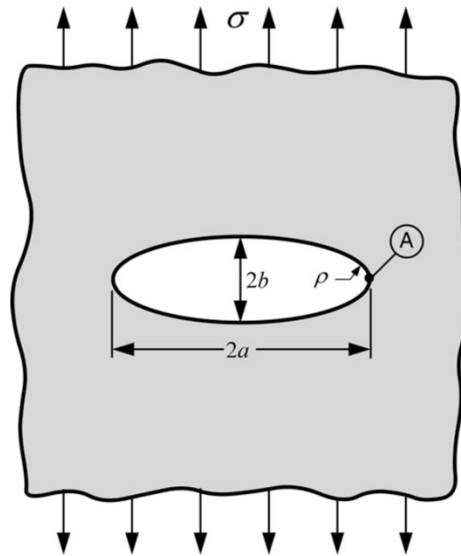


Figure 25 Elliptical hole in 2D infinite solid under tension. Point A is representing the maximum stress at the crack tip [94].

Inglis [4] provided the first evidence for the stress concentration effect of the crack existence by analyzing an elliptical hole in plates. His famous analysis is represented in Figure 25, which contains an elliptical hole introduced to perpendicular stress applied to the ellipse major axis. The ellipse dimensions are $2a$ long and $2b$ wide. The main point here that makes this case infinite is that Inglis didn't consider the influence of the plate boundary. In other words, the plate width and thickness are much larger than $2a$ and $2b$, respectively. The stress at the crack tip is given by:

$$\sigma_A = \sigma \left(1 + \frac{2a}{b} \right) \quad \text{Eq 4.1}$$

The ratio $\frac{\sigma_A}{\sigma}$ is the stress concentration factor, K_I . Note that if $a = b$, this elliptical hole will be circular and $K_I = 3$, which is a well-known result found in many fractures mechanics literature [94].

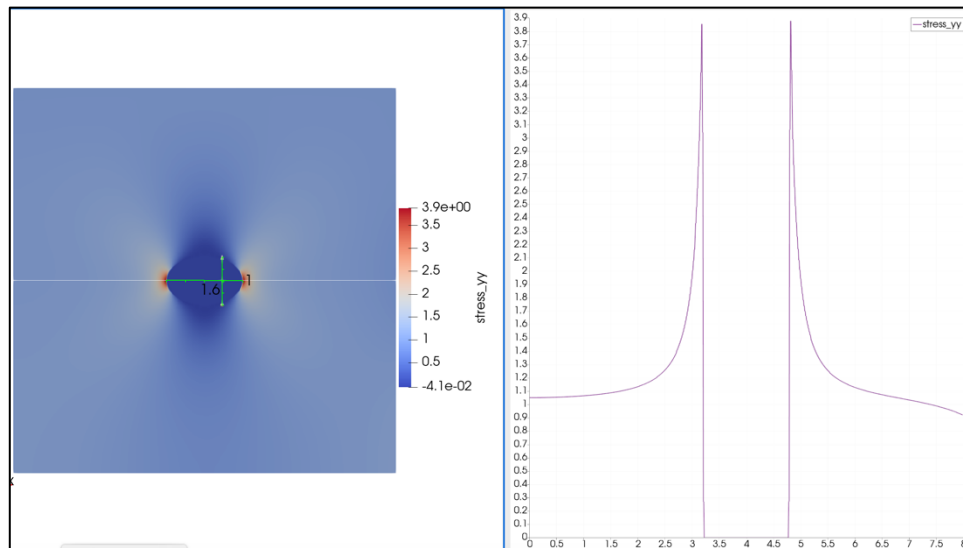


Figure 26 The model expectation well agreed with the stress concentration factor (K_I) calculation as expected by Inglis [4].

Here, we examined our model to capture this theoretical analysis; the domain was constructed to fulfill the infinite conditions. The simulated elliptical hole had $a = 0.8$ and $b = 0.5$ dimensions, with a unity applied stress. The simulation results were well-matched with the theoretical expectations and presented in Figure 26.

4.1.2 An elliptical cavity in a finite domain

If the crack dimensions are minimal compared to the plate dimensions, the external boundary effects will not influence the crack-tip conditions, as illustrated above. But such influences will occur once these dimensions become comparable with the crack size. In such cases, the Inglis stress intensity solution is not applicable.

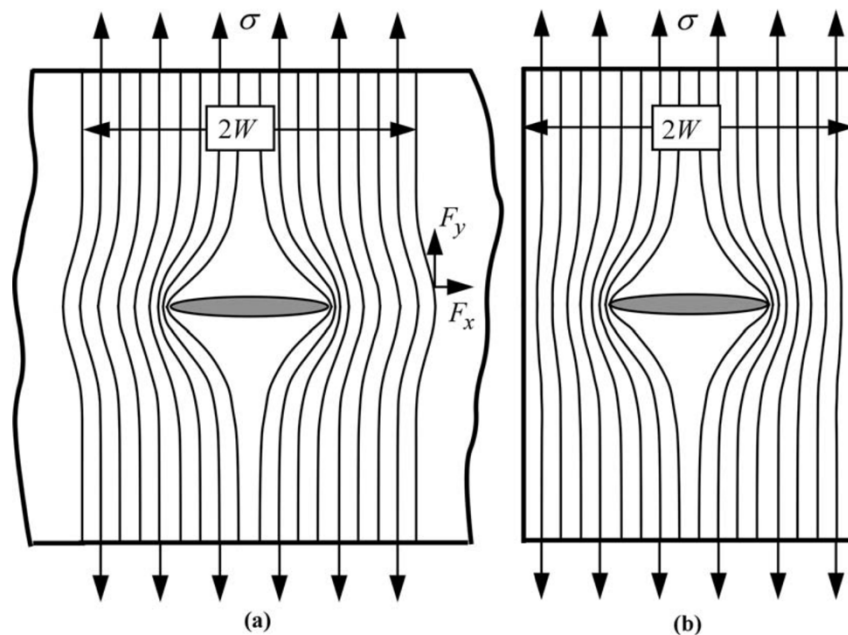


Figure 27 A schematic illustration of the stress concentration builds up (and effect) near the crack tip in the case of (a) infinite plate and (b) finite plate [94].

In this finite test case, we consider a cracked plate subjected to uniaxial tensile stress, see Figure 27. This Figure schematically illustrates the consequence of finite plate width on the crack tip stress distribution (displayed in lines of force). Note that the tensile stress will not be transmitted through a crack (no atoms exist). Hence, the force lines will be shifted near the crack, leading to a local stress concentration. In other words, the finite boundary condition compresses the force lines and results in more elevated stress at the crack tip.

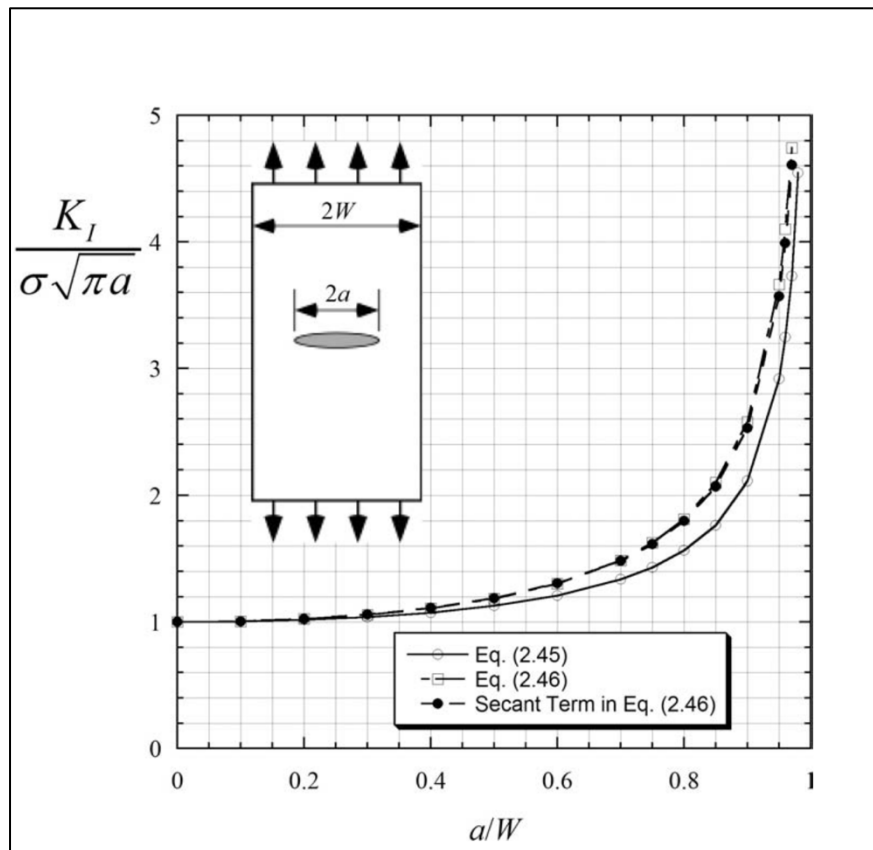


Figure 28 The analytical solution of the finite plate boundaries affects the stress near the crack tip, as shown in Eq 4.2, mainly the Secant term. Note that Eq. 2.46 [94] seen in this Figure is the Eq. 4.2 seen in text.

The finite-element analysis has acquired an accurate and acceptable solution for a crack in a finite plate. Such solutions are usually fitted with a polynomial expression. One of these solutions was conducted by Tada et al. [94 – 95] and presented as:

$$K_I = \sigma\sqrt{\pi a} \left[\sqrt{\sec\left(\frac{\pi}{2W}\right)} \left[1 - 0.025\left(\frac{a}{W}\right)^2 + 0.06\left(\frac{a}{W}\right)^4 \right] \right] \quad \text{Eq 4.2}$$

The influences of the finite width (W), as illustrated in Eq. 4.2 is presented in Figure 28, partially the Secant term of that equation. We compared these analyses with our model simulations, and the well-agreed results are summarized in Figure 29. The model results started to deviate at $\frac{a}{w} \sim 0.6$, but the behavior trend kept similar.

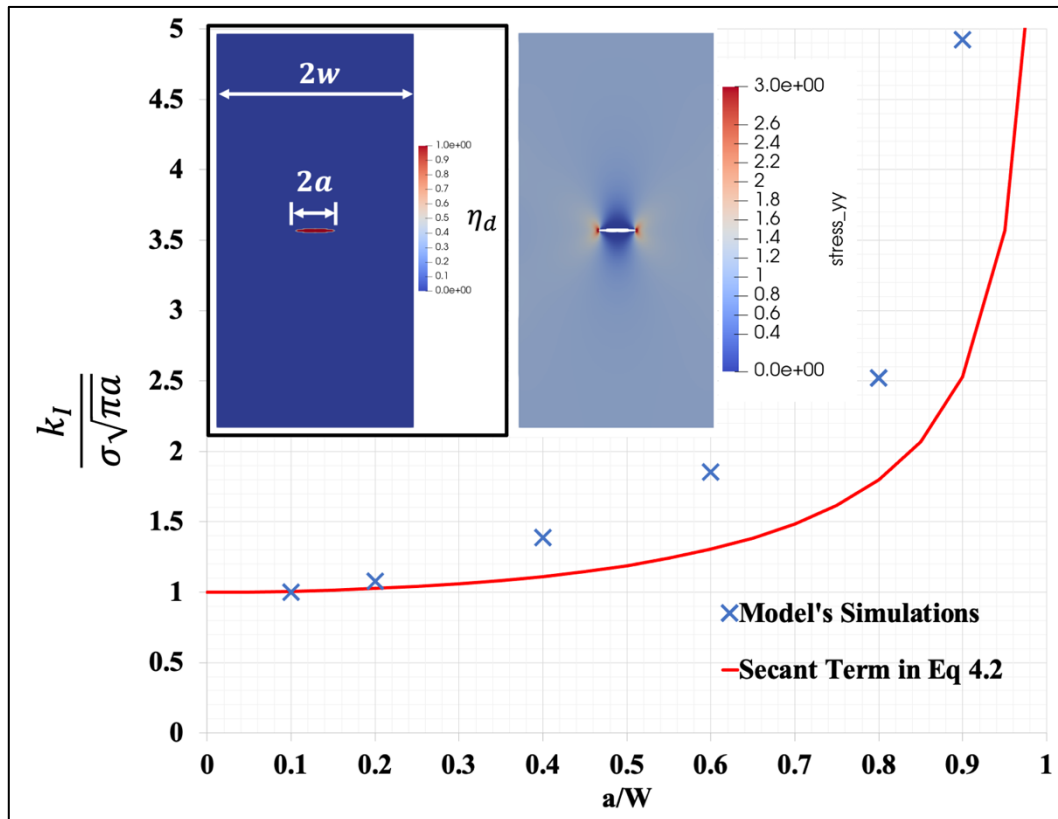


Figure 29 The model simulations well aggregated with the analytical solutions presented in Eq 4.2, particularly the Secant term with a bit deviation from $a/w \sim 0.6$. But the behavior trend remained similar. The figure also shows how the stress is highly concentrated at the crack tip.

4.1.3 Model validation based on Nuclear-grade graphite material parameters

To verify the model's capability to study the microstructure-dependent fracture in nuclear-grade graphite, we compared the preliminary model results with the work from INL, P. Chakraborty, et al., [23]. First, we demonstrate our model capabilities by simulating the single-edge notch tensile (SENT), same as [23]; this test is a considerable benchmarking case. The utilized domain setup and the model parameters are presented in Figure 30 [23]. The model results that compared with the INL work [23] were illustrated in Figure 31. In this benchmark case, the crack propagates due to the applied displacements; see the rapid drop in stress in the stress-strain curve (Figure 31 a & b) after the crack initiations. The failure configuration is shown in Figure 31 c & d. These results demonstrate the capability of our model to capture the brittle crack propagation behavior with a linear stress-strain relationship till exceeding the fracture strength, tailgated by quick unloading.

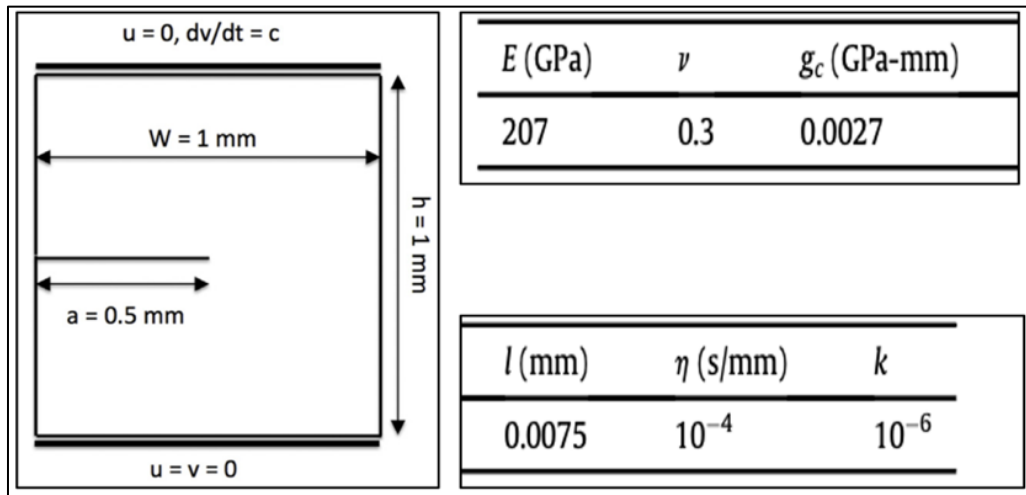


Figure 30 Specimen geometry and boundary conditions along with the model parameters for the SENT test [23].

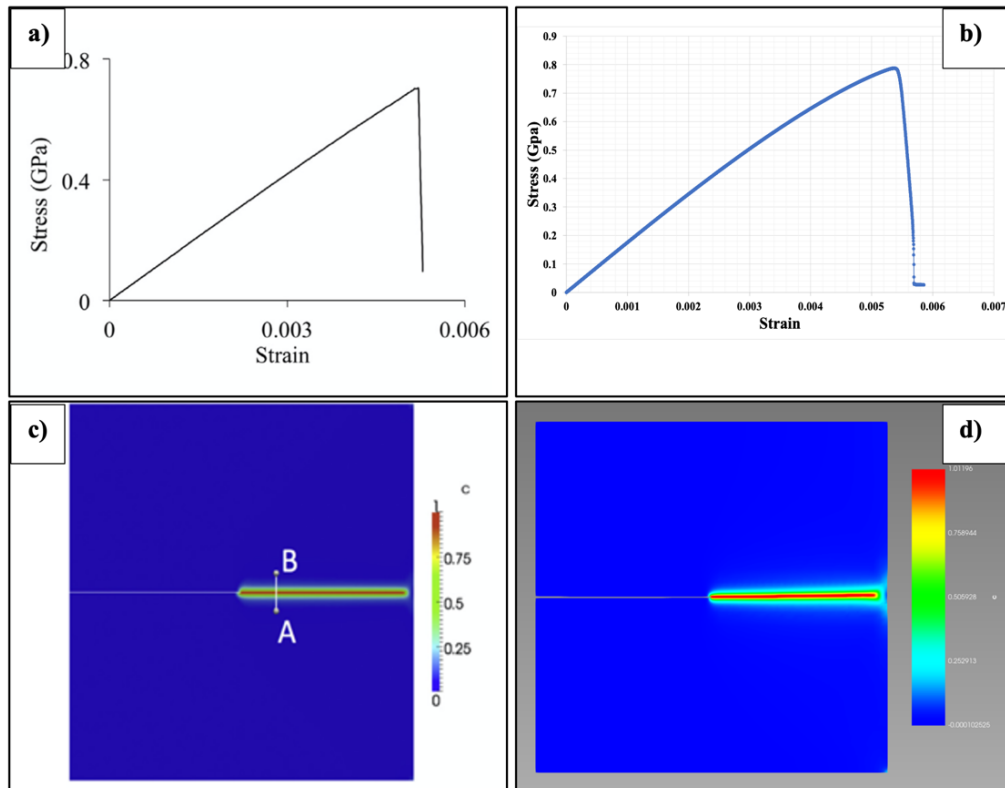


Figure 31 Brittle fracture propagation of Mode I in a single-edge notch tensile case using the phase-field fracture model. The left column is the work by P. Chakraborty et al., [23], while the right column is this work simulation. (a&b) stress-strain along loading direction, (c&d) final configuration colored by the damage order parameter.

4.2 Experimentally validated Multiphysics modeling of fracture induced by thermal shocks in Sintered UO₂ Pellets⁴

In this section, we employed our phase-field fracture model to investigate the fracture behavior of the UO₂ fuel pellet introduced to a thermal shock. The model was utilized to mimic the UO₂ thermal shock experiment as described earlier in Chapter II and detailed in [19]. The fundamental model parameters were calculated based on the UO₂ thermomechanical properties, while the other effective parameters were determined based on a parametric study as briefly described here, and in [19]. Due to the instantaneous temperature drop on the pellet surface, a large jump in the stresses throughout the pellet took place, mainly on the cooling side face. This rapid temperature change and the increased localized stresses are considered the main driving forces for the UO₂ cracking. The model didn't count for the creep effect; we ignored the fission gas release, and the grain growth influences. However, the qualitative effects considered in parametric study calculations for the energy release rate (G_c), as illustrated throughout this section.

4.2.1 Thermal shocking experimental results of UO₂ Sintered fuel Pellet

The UO₂ samples were cut axially through the center and then radially through the middle, illustrated in Figure 13. Numerous optical and SEM images are displayed in

⁴ Reprinted with permission from Elsevier "Experimentally validated Multiphysics modeling of fracture induced by thermal shocks in Sintered UO₂ Pellets" by L. D. McClenny, M. I. Butt, M. Goma Abdoelatef, M. J. Pate, K. L. Yee, R. Harikrishnan, D. Perez-Nunez, W. Jiang, L. H. Ortega, S. M. McDevitt and K. Ahmed, 2022. , Journal of Nuclear Materials. Copyright [2022] by Journal of Nuclear Materials.

Appendix section of the reference [19], representing the final fracture results for each of the pellets, and can be characterized similarly to those shown in Figures 32 and 33.

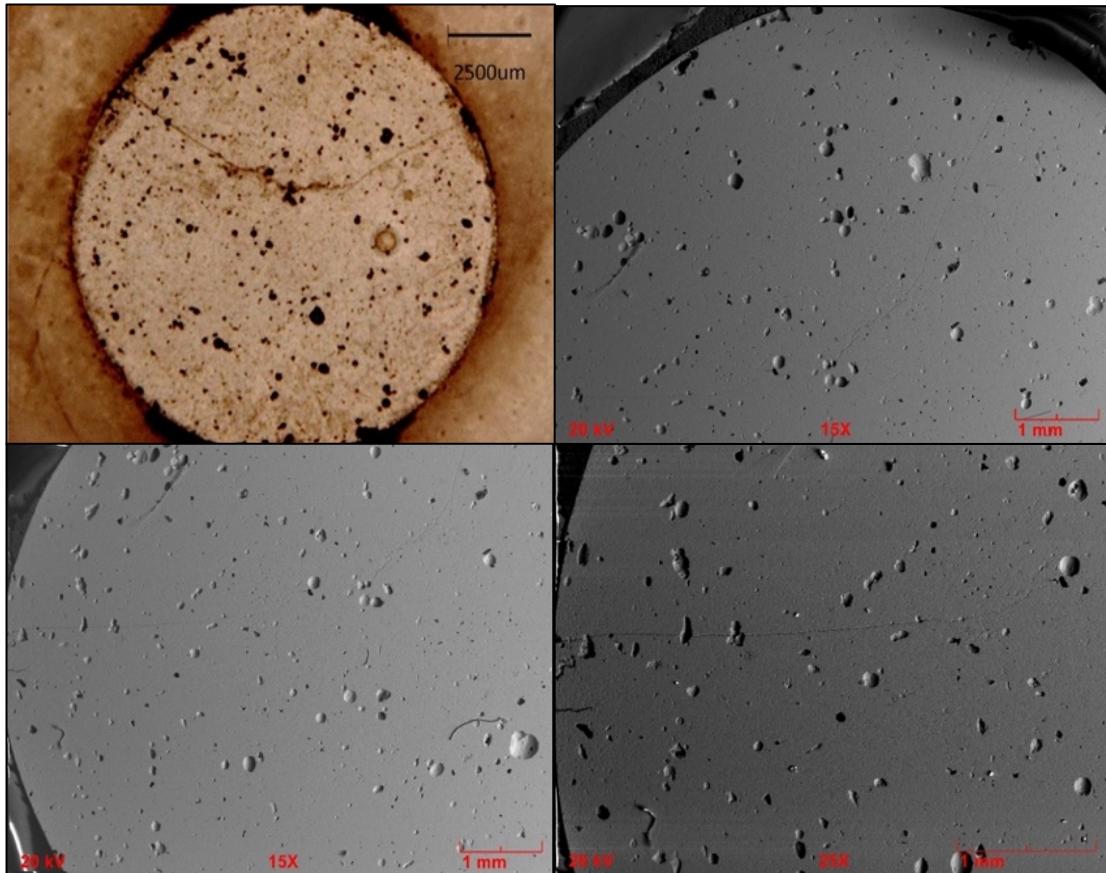


Figure 32 The experimental snapshots of various specimens' microstructures reveal various porosity (number density and sizes) distributions. Some porosities have a few micrometers size, or even less, while bigger ones take ellipsoidal shapes. These larger pores have a size of several tens of micrometers [19].

The pellets were sintered in a mixture of argon and helium gas to prevent oxidation and bakeout was conducted for some pellets to remove any moisture. The pellets were sintered to minimize porosity and the density of the pellets was determined using the

Archimedes method also shown in Table 3. The theoretical density of UO_2 is determined to be approximately 10.96 g/cc [55], leading to the density of the pellets being 80–90% of the theoretical density. The variation in density is due to different sintering times, which leads to a change in porosity. A table of densities for various sintering experiments, the sintering processes used, as well as their subsequent quenching thermal quenching results is included in the author's previous work [19].

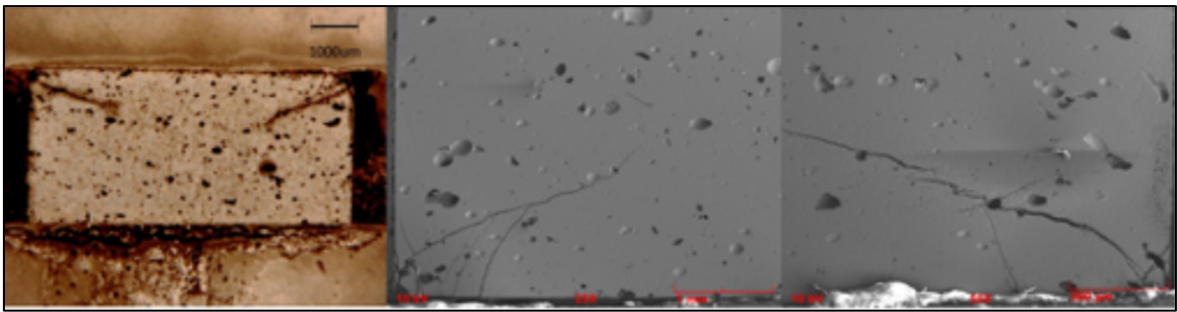


Figure 33 Experimental snapshots of various microstructures reveal various porosity (number density and sizes) distributions as well as subsequent fracture of the pellet. Some porosities are a few micrometers in size or even less, while bigger ones take ellipsoidal shapes. These larger pores have a size of several tens of micrometers. [19].

4.2.2 Model results, validations, and discussion

The fundamental model parameters were calculated based on the UO_2 thermomechanical properties, while the other effective parameters were determined based on a parametric study as described below. Due to the instantaneous temperature drop on the pellet surface, a large jump in the stresses throughout the pellet occurred. This behavior is mainly observed on the cooling side face. The rapid temperature changes as well as the increased localized stresses are considered the main driving forces for the UO_2 fuel cracking. To obtain initial insights while minding computational costs, we only considered

fresh fuel (zero burnup) in this model and then compared these simulated results with the previously described experiment outcomes. The model does not account for creep, fission gas release effects and grain growth influences were also ignored, in the interest of creating a model that is computationally tractable with known and predictable physics. However, the qualitative effects of these phenomena should be considered in parametric study calculations of the energy release rate (G_c) as illustrated throughout this section.

The studied domain consists of a 3D fuel pellet with a 5 mm radius, and the axial direction height was set to 10 mm. The initial temperature condition of the pellet was set to 750 °C. Only the determined “contact region” of the pellet was introduced to the low-temperature, -10 °C, simulating a thermal shock condition. A Dirichlet boundary condition (BC) for temperature was used to set the thermal bath temperature at the contact area, and Zero flux boundary conditions outside. For the displacement field, a traction-free BC was utilized. While the BC for the phase-field evolution was a homogeneous zero flux on the entire boundary of the domain and the crack order parameters. In this study, the swelling and the densification consequence were considered negligibly small as described in Li and Shirvan [72].

The model temperature evolution at the pellet center and right-side points against the experimental thermal shock data to verify the model capability to capture the fracture behavior was compared. This verification was presented in Figure 34, which demonstrates consistency between the computational model and the experimental temperature behavior. Moreover, the model captured the time evolution of the imposed temperature gradient across the pellet correctly, i.e., the outer surface temperature drops immediately to the

temperature of the cold bath while the center temperature reaches the same temperature in 300s. Note that the counter timer in the experimental plot starts after the preheating process at nearly 430 s, as seen in Figure 15(a). The basic UO₂ thermomechanical properties utilized in this work are listed in Table 5.

Table 4 The data used to define the model required parameter for this work simulations [19].

Property	Symbol	Value	Unit	Reference
Young's modulus	E	358	GPa	[24, 96]
Poisson Ratio	ν	0.23		[96]
Thermal Conductivity	k	~5	(W/m-K)	[55]
Heat Capacity	C	~280	J/(g.k)	[19]
Fuel Density	ρ	10.97	g/cm ³	[55]
Energy Release Rate	G_c	80	MPa•mm	[19]
Length scale	ℓ	1×10^{-3}	mm	[19]
viscosity	η	1×10^{-8}	s/mm	[97]

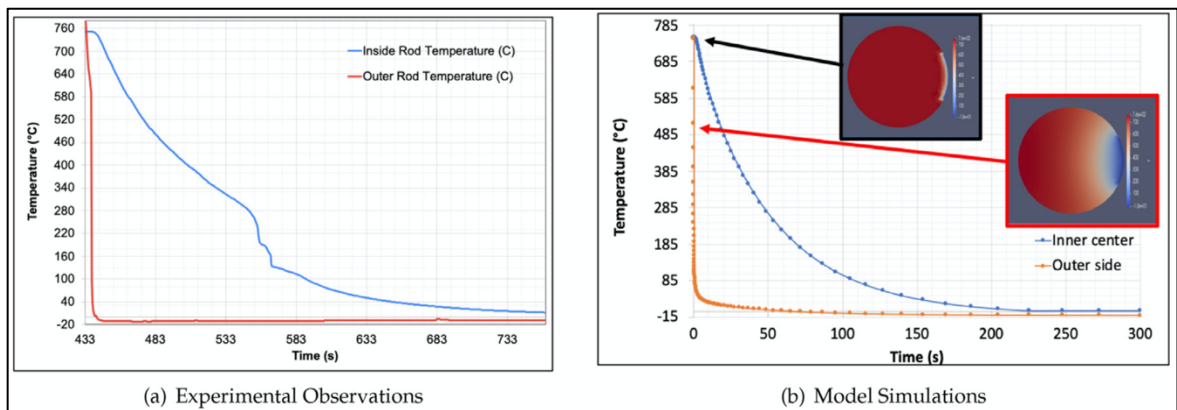


Figure 34 The temperature evolution of the pellet outer surface and inner center points. Note that the counter timer in the experiment plot starts after the preheating process at approximately 430 s. The snapshots in the simulation plot show the temperature distribution (colored mapped from $-10\text{ }^{\circ}\text{C}$, dark blue to $750\text{ }^{\circ}\text{C}$ dark red) at the initial and mid-time steps. The agreement of the temperature distribution and evolution between the model and the experiment results verified the basic model parameter selection [19].

It has previously been shown that the strength of brittle materials, such as UO_2 , is strongly dependent on porosity microstructure [24, 72]. Moreover, the porosity size and distribution may change with grain size variations. This trend is more pronounced for larger pore sizes [98]. The experimental work presented here obtained various microstructures containing micro and macro pores in different UO_2 specimens, as shown in Figures 32 and 33, and the Appendix section in the reference [19]. In some of these specimens, many small spherical pores were almost uniformly distributed in the sample, whereas some exhibited ellipsoidal pores. Since the porosity of the UO_2 specimens undoubtedly affected the fracture mechanics in ways that are not completely understood, various simulations were conducted with different energy release rates (\mathcal{G}_c) until a value was settled upon that resulted in a fracture behavior similar to those found in the experiment. It is worth noting that similar methods were utilized experimentally by Doitrand et al. [44], and Henry et al. [45] to determine the strength and fracture toughness of UO_2 .

Indeed, the energy release rate, \mathcal{G}_c (or equivalently fracture toughness) is microstructure- and size-dependent, and its value is unknown for UO_2 and other nuclear fuels. Its value is difficult to estimate both from experiments and first-principles simulations. Lower-scale, first-principles simulations are limited to small sizes and cannot evaluate the actual value for a realistic microstructure. Even experimental studies cannot extract this number directly. They usually utilize either finite-element simulations or employ a few limiting analytical expressions from the linear elastic fracture mechanics to derive this value from their data [44 – 45]. Here, a set of \mathcal{G}_c and contract areas were able

to capture the overall fracture trend of the corresponding experimental data. In fact, we believe that the phase-field fracture employed here presents a new method for calculating the energy release rate G_c /fracture toughness.

Here, a uniform distribution of porosity is assumed which may not actually be the case but is still a reasonable assumption. A subsequent method could be developed in future works to account for the size, morphology, and distribution of porosity. A sensitivity study carried out in this work demonstrates an accordant prediction of the failure behavior and provides consistent information about material strength, fracture toughness, energy release rate, and other model parameters. The outcome of this sensitivity study, as presented in Table 6 and Figures 35 and 36, is used to determine the corresponding model parameters by directly comparing various forms of the predicted failure behavior to the experimental measurements as well as to determine the energy release rate parameter.

Table 5 Detailed description of simulation test case script for the results provided in this section. 45 total simulations were run according to obtain the well-match G_c [19].

# Test cases	Contact Area fraction	Energy release rate (G_c) range (MPa•mm)
9	Single line	1, 1.5, 5, 10, 30, 50, 80, 100, 150
9	1/6	1, 1.5, 5, 10, 30, 50, 80, 100, 150
9	1/3	1, 1.5, 5, 10, 30, 50, 80, 100, 150
9	2/3	1, 1.5, 5, 10, 30, 50, 80, 100, 150
9	1	1, 1.5, 5, 10, 30, 50, 80, 100, 150
45	Total numbers of test cases	
Selected test case	100% as the experiment contact area	80 MPa•mm

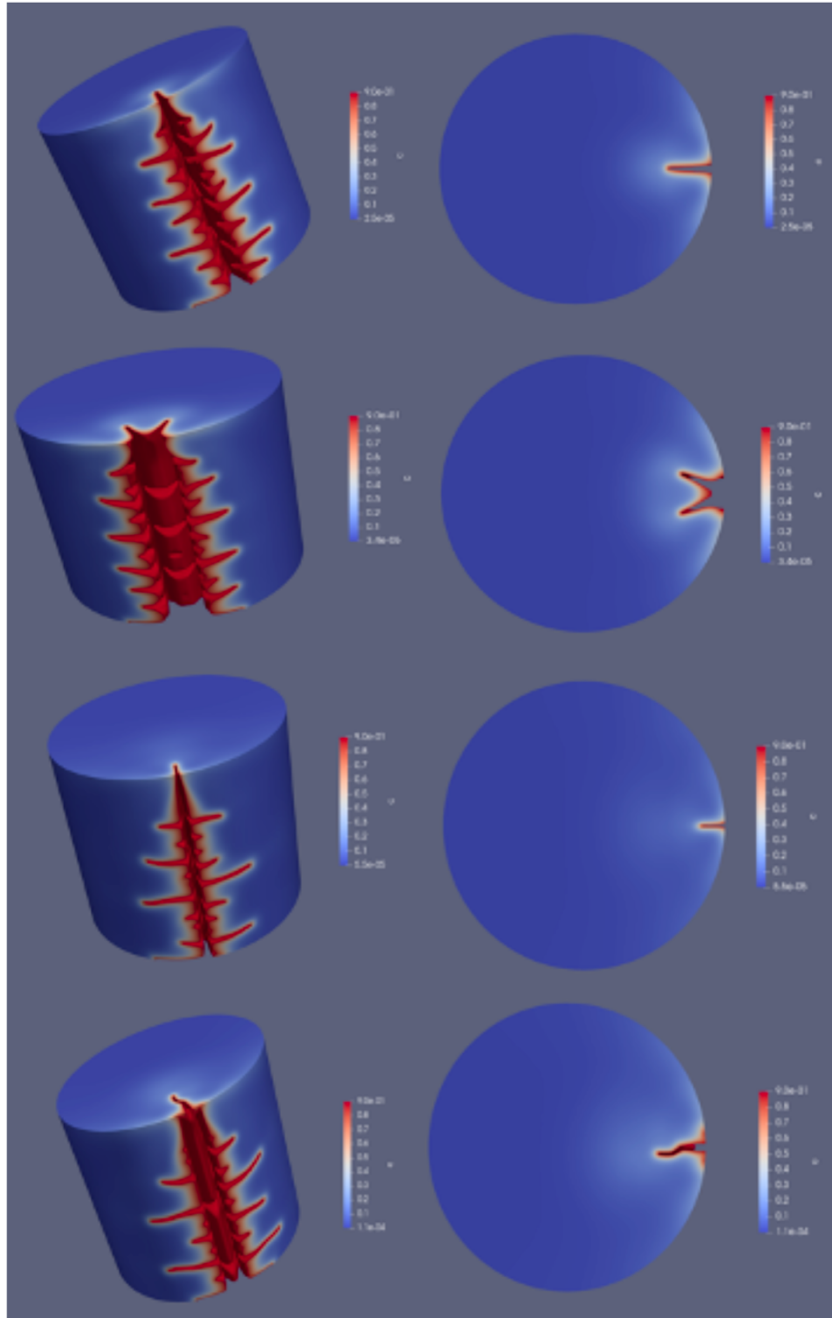


Figure 35 Snapshots of selected test cases simulations present the effect of different G_c and different contact areas on the formation and evolutions of the cracks induced by thermal shock in UO_2 fuel pellets. The first two rows show the cracks behaviors based on $G_c = 10$ MPa-mm and the last two rows at $G_c = 30$ MPa-mm. The first and third rows are simply a single line contact area, while the second and fourth ones are established on a wider contact area, almost 1/6 of the actual experiment contact area [19].

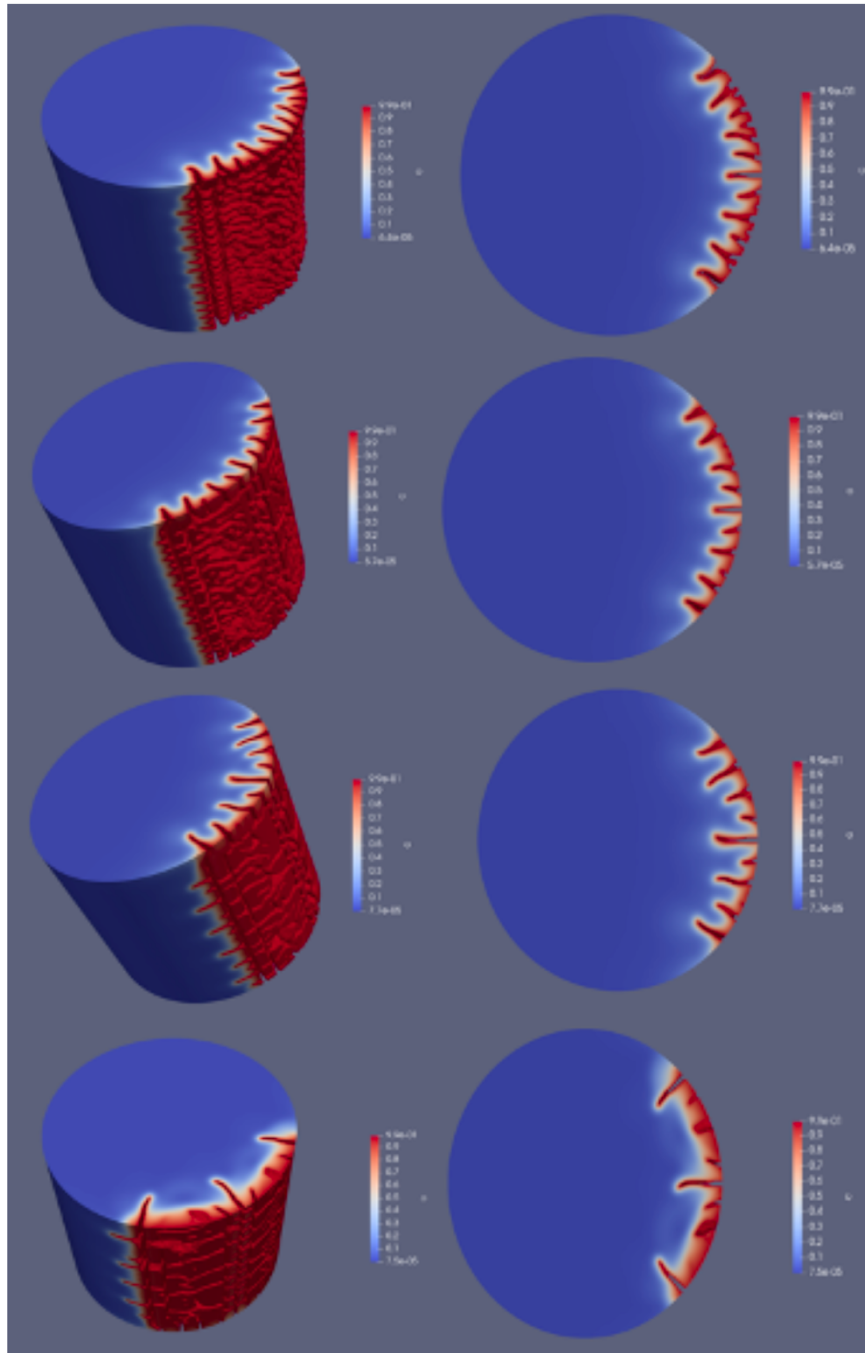


Figure 36 Snapshots of selected test cases simulations manifest the effect of \mathcal{G}_c values, with the case of actual contact area, on the formation and evolutions of the cracks induced by thermal shock in UO_2 fuel pellet. The damage shape evolutions with $\mathcal{G}_c = 10$ MPa-mm was seen in the first row. While the elected evolution with $\mathcal{G}_c = 80$ MPa-mm, which was found to be well-matched with the experimental results, is presented in the last row. The second and third rows show the simulations with $\mathcal{G}_c = 30$ MPa-mm and $\mathcal{G}_c = 50$ MPa-mm, respectively [19].

Some of these contact areas could have varied slightly from those seen in the physical experiments, but these various configurations improve our understanding of the (\mathcal{G}_c) parameter influence on the crack formations and evolutions, as well as account for some level of uncertainty in how large the contact region (cooling side area) truly was in the experiment. Additionally, variations on parameters such as (\mathcal{G}_c) and the contact region were intended to assist in capturing physical inconsistencies in the experiments, such as insulation, etc that were unaccounted for in the computational model. In all cases, we utilized a range of (\mathcal{G}_c) parameters along with the various contact area configurations. Figures 35 and 36 provide a demonstration of simulations based on what is perceived to be the approximate contact region as the experiment with different \mathcal{G}_c values varying from 10 to 80 MPa·mm. Consistent results between the simulations and the experimental results with $\mathcal{G}_c = 80$ MPa·mm was observed, as seen in the last row of Figure 36 and detailed in Figure 37. A reasonable agreement is found between the model prediction of the crack pattern and the thermal shock experiment results, as seen in Figure 37.

The model could interpret the formation and evolution of such cracks induced by a thermal shock, particularly the primary radial cracks. There were two major (longer) radial cracks, as illustrated in the hoop and radial stress formation and evolution process in Figure 38. The cracks formed immediately on the pellet circumferential boundary after the instantaneous drop in the outer temperature (thermal shock). These results demonstrate consistent thermal elastic cracking behavior, wherein the radial cracks are generated by tensile hoop stress. Figure 38 may be referenced for an improved illustration. It can be observed that the cracks do not propagate inward towards the center of the pellet. Such

behavior is anticipated due to the existence of the compression zone that may hinder the cracks propagation, and a similar trend was observed by Li and Shirvan [72].

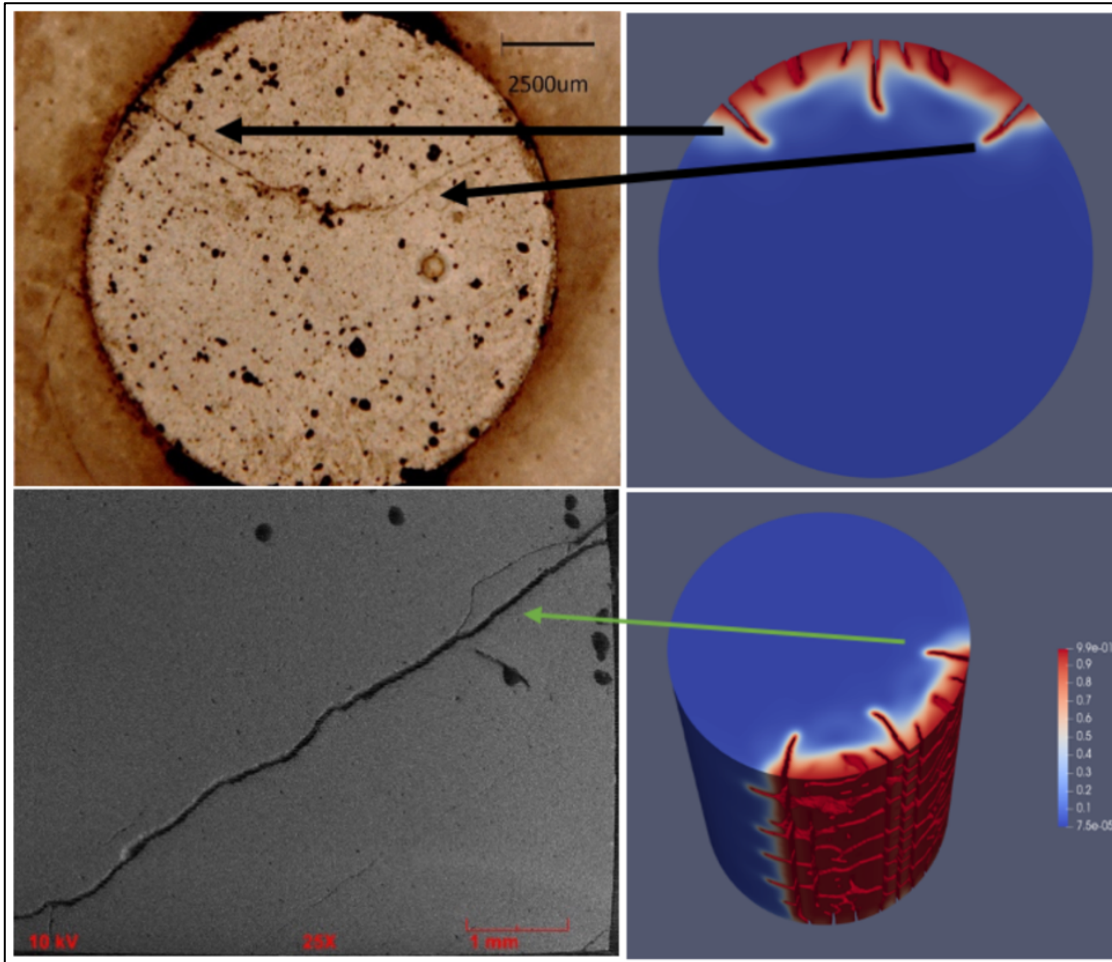


Figure 37 Comparison of final crack patterns induced by thermal shock between this work experiment observations after the thermal shock testing (upper), and (lower) the elected model simulation (colored by the fractured order parameter field distribution). The model could capture the formation and evolution of primary radial cracks. As seen, there are two major (longer) radial cracks that formed immediately on the pellet circumferential boundary after the instantaneous drop in the outer temperature (thermal shock). Moreover, the simulated crack thickness was found to be similar to the experimental observation, as seen in left column. Minor differences between the model and the experiment results were noticed (such as the middle crack shown in the model simulations). These differences can be attributed to the absence of accounting for the effect of underlying microstructure (e.g., size and morphology of pores and grains) in the current model; overcoming such limitations would be the focus of future studies [19].

Compared with the experiment where two major cracks merge in the middle, this discrepancy could be attributed to the porosity of the microstructure causing inconsistent internal compression not anticipated by the computational model, resulting in the crack propagating entirely through the center of the pellet. It is worth noting that some of the tested specimens contain various porosity sizes and distributions and these uncertainties will have an impact on computational fracture predictions. For what is attributed to the same reason, it can be observed that a “middle” crack in the model resulted that did not propagate experimentally. Similarly, it was shown that the crack thickness is consistent with other samples with lower porosity. It is also worth noting that the model correctly reproduces different morphologies of cracks as observed in experiments.

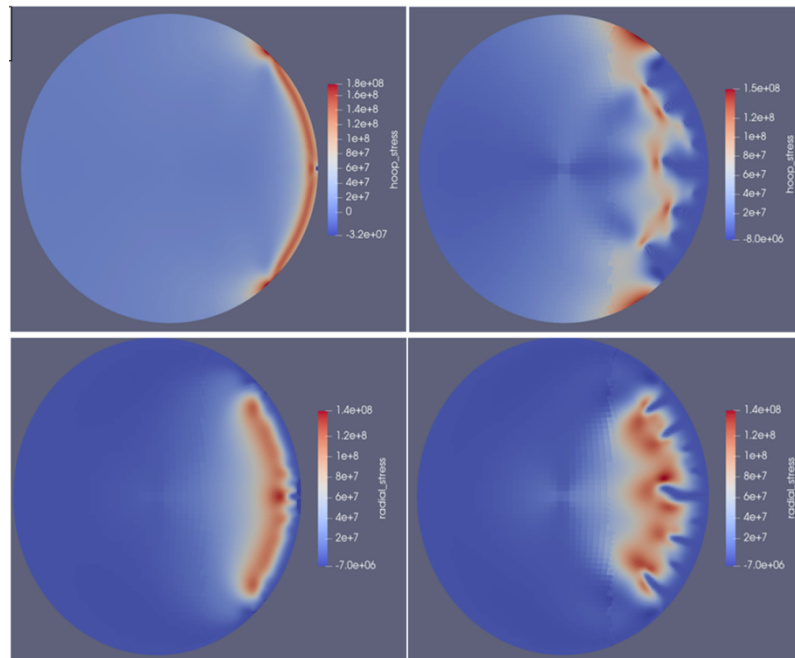


Figure 38 Snapshots illustrate the stresses formation and evolution before and after the cracks initiation and propagation for (upper) hoop stresses (lower) radial stress—the evaluation forms from left to right. The left column represents the stresses formation right after the instantaneous drop in temperature, while the right column shows the stresses evolution at the mid of the simulation time [19].

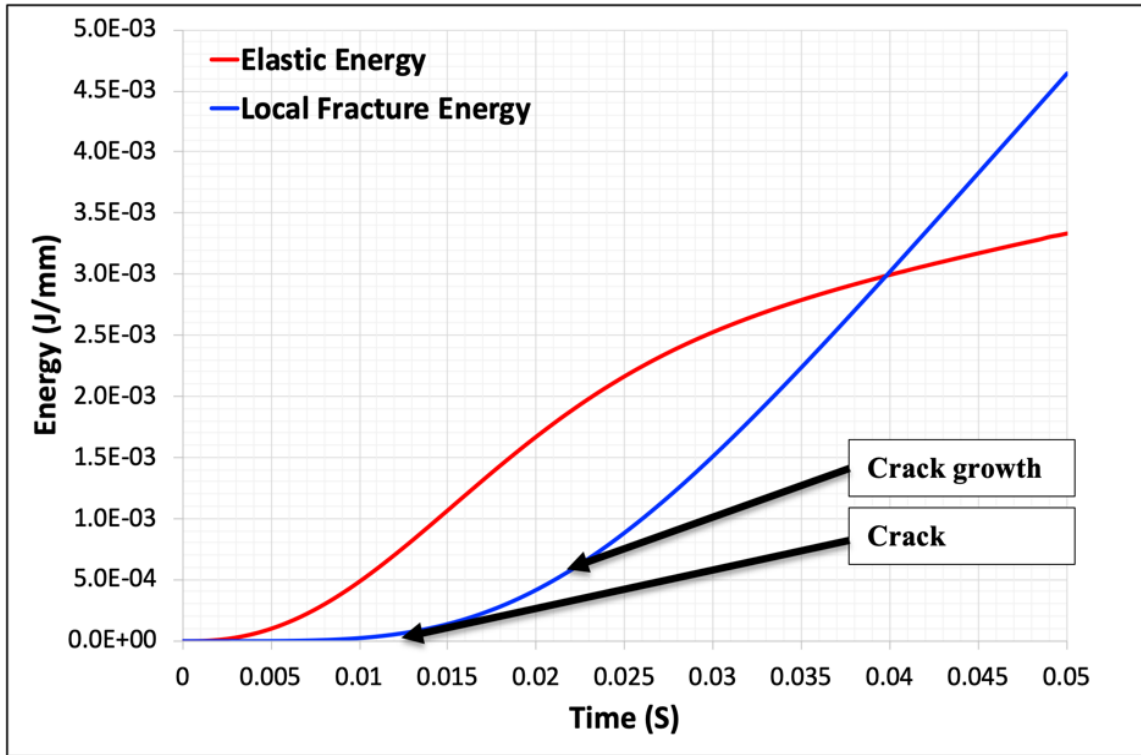


Figure 39 Evolution of elastic strain energy and the formation and growth of the local fracture energy based on fine mesh and length scale parameter of 10^{-3} mm for the elected simulation case; see Figure 37. The elastic strain energy increases with increasing the temperature difference between the inner center and the outer surface (see Figure 34). The cracks immediately initiated on the pellet outer surface at about 10^{-2} s, right after the instantaneous drop in temperature. The elastic strain energy rate decreases with generating new fracture faces [19].

The elastic strain energy and fracture energy behaviors due to the thermal shock fracture were captured and presented in Figure 39. As seen from this Figure, the elastic strain energy rises with increasing the temperature difference between the inner center and outer surfaces (see Figure 34). As understood from this Figure, the cracks immediately appear on the pellet outer surface at about 10^{-2} s right after the instantaneous drop in temperature. After some areas reached a full damage state (fully cracked areas), the rate

of increasing of elastic strain declines as it is employed to generate new fracture surfaces, as described by Griffith [5]. Furthermore, the Figure demonstrates that the local fracture energy increases with crack growth as expected. It is anticipated that this increase in the local fracture energy to be suppressed if the simulations ran long enough to capture the compressive loading in the central region as seen in [72].

4.3 Evaluation of fracture behaviors in porous materials: One-particle analysis.

The random distribution of pores in nuclear materials, including the pores' site, size, and shape, makes the fracture of porous nuclear materials/fuels a challenging problem. We address such parameters' influences herein to understand the fundamentals that lead to the stochastic tearing behavior in nuclear-grade graphite. The same method will be applied to the TRISO buffer layer investigations. Here, we utilized our validated model to understand the effect of porosity (single-particle system) on the stress building up and the fracture behavior. The parameters examined showed that the shape and orientation of the porous particle, concerning the applied load direction, significantly influence the strength and the system fracture behavior. These consequences are more pronounced with increasing the porosity volume fraction.

We started by benchmarking our new model results that examine the stresses building up at different volume fractions against the other models' formulations [28 – 29] that use an external mesh with a predefined hole. The comparison was presented in Figure 40 and showed a good agreement till $\sim +80\%$ volume fraction, where we noticed a bit deviation. These discrepancies are acceptable since all the studied cases lie below that volume fraction value.

4.3.1 Effect of porosity shapes and volume fractions on stress distributions.

Here, the model investigates the effect of single pore particle shape and volume fraction on the stresses building up in nuclear-grade graphite materials. The materials parameters used in these simulations are similar to INL work [23], and listed in Table 7.

In these cases of studies, the particle is assumed to be a void and represented by an order parameter (η_p); the material stiffness is interpolated (see Eq 3.19) to ensure that the stiffness inside the void is zero. The effect of the holes is averaged through the system, which is assumed to be continuous and homogeneous. Figure 41 shows the various investigated voids' shapes and orientations utilized in these test cases. Figure 42 shows the stress building up in the system for each shape with different volume fraction.

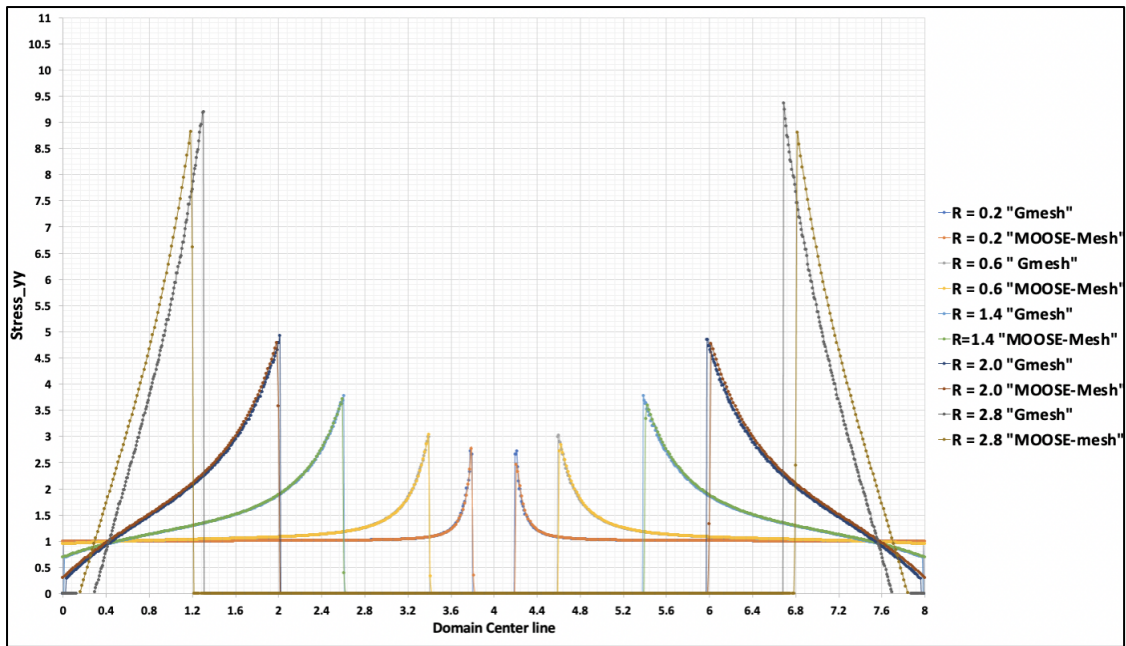


Figure 40 An illustration of the good agreement results while comparing the model-new formation (MOOSE-mesh) with the classical phase-field fracture models [28] [29] that use external meshes with pre-defined holes (Gmesh) at different volume fractions (different Rs). The deviations started to be noticed with a $\sim +80\%$ volume fraction which is acceptable in all of our cases of studies.

Table 6 The nuclear-grade graphite materials' properties similar to [23].

E (GPa)	Poisson ratio (ν)	G_c (GPa · mm)	l (mm)	viscosity ($\frac{s}{mm}$)
207	0.3	0.0027	0.0075	10^{-6}

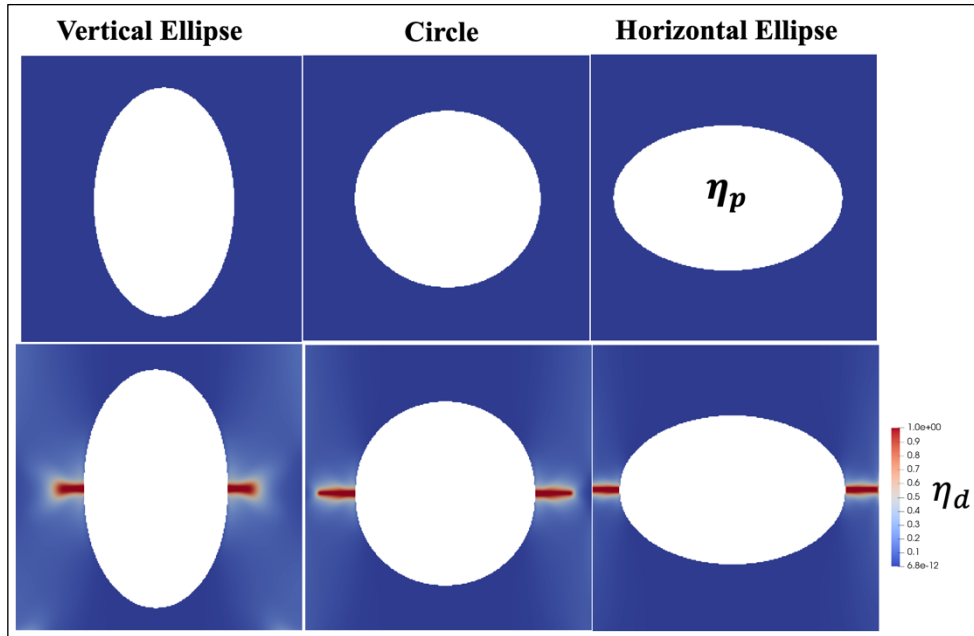


Figure 41 Snapshots illustrate the studies void shapes, η_p (see first row) and the cracking shape (see second row). Note that the damage order parameter (η_d) is mapped by red color. Note that the applied load is in YY-direction. This Figure's snapshots only show a certain volume fraction (30%) but this study investigates various volume fraction, see Figures 42 & 43.

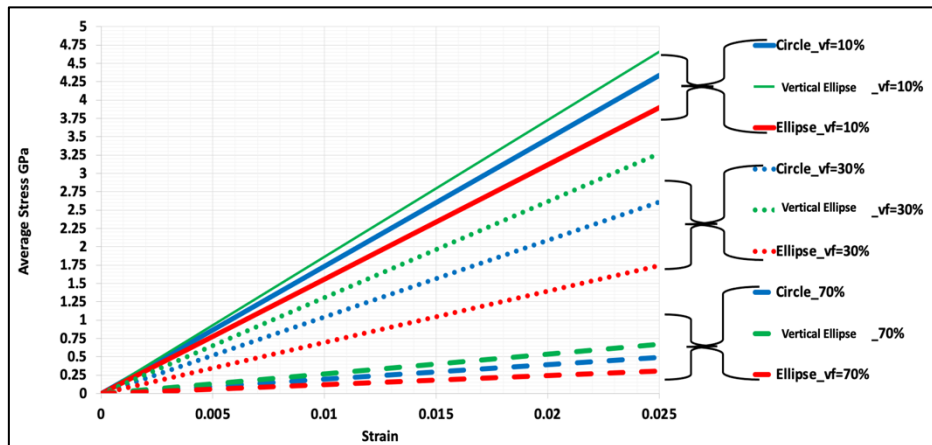


Figure 42 An illustration of the single-particle shape and orientation effect on the stresses building up in a nuclear-grade graphite system. The Figure shows how the vertical ellipse shape (parallel to the applied load direction, stress_{yy}) could withstand better. All the particle shapes related to maximum stress degrade with volume fraction increases.

4.3.2 Effect of porosity shapes and volume fractions on fracture behaviors.

With a YY-direction applied load, the vertical ellipse demonstrates a better behavior for both: (1) applied stress, see Figure 42, and (2) cracking behavior, see Figure 43. These model results are consistent with all the fracture mechanics theories [94] that demonstrate the higher stress and faster fracture will be associated with higher curvature periductular to the applied load directions. Both Figures (42 and 43) shows that the nuclear grade graphite will have a lower strength and hence fractured faster by increasing the void volume fractions, this is because the materials will be less stiff in such cases.

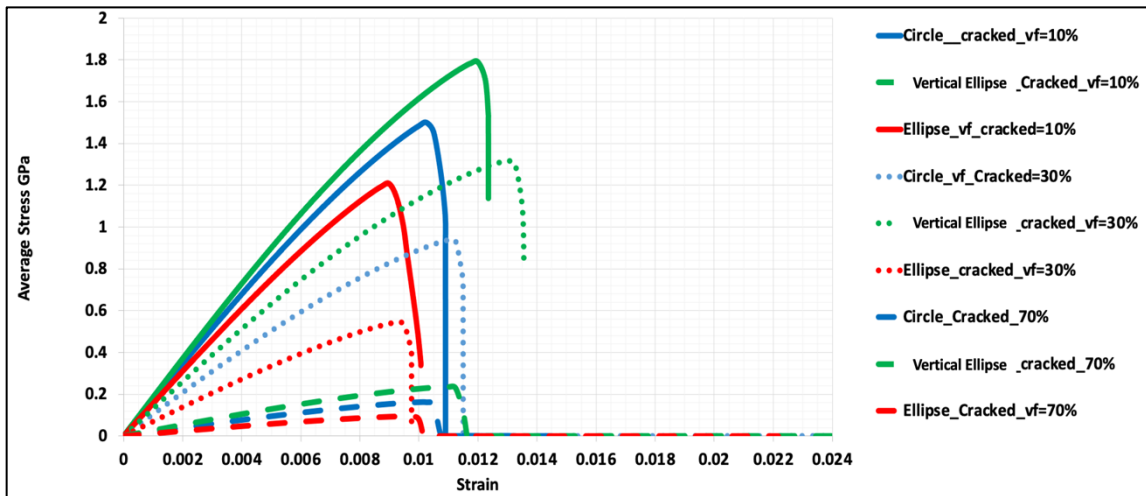


Figure 43 An illustration of the single-particle shape and orientation effect on the cracking behavior in a nuclear-grade graphite system. The Figure shows how the vertical ellipse shape (parallel to the applied load direction, stress_{yy}) could withstand better. Increasing the volume fraction will lead to faster cracks for all the shapes.

4.4 Multi-set Order parameter Novel Phase-field modeling of Fracture: Two-particles-system assessments.

Our novel phase-field fracture model that has been verified using UO₂ and nuclear grade graphite data is implemented here to capture the concurrent microstructure evolution and fracture formation and propagations concurrently. Studying the competition between microstructure evolution and cracking is crucial to understanding the stochastic tearing behavior in nuclear fuels. On the one hand, the crack might be blunt due to the pores interactions resulting in the material's toughness enhancement. On the other hand, the material will be less stiff or weaker due to increased pores volume fraction. This work's model is contributed to investigating such multi-physics complicated phenomena.

Multi-set order parameters describe the concurrent crack formation and propagation along with microstructure evolution (including second phase particles) for the first time in the field. The verified model is first applied to study the stress distribution around voids boundaries in a static two-particle domain, then applied to a heterogeneous nuclear-grade graphite system to determine the effect of void coalescence on the fracture behaviors that changes the effective toughness of the materials; hence influences the mechanical properties.

4.4.1 Static two-particles analysis

Here, we studied static two-particles (voids) inside a nuclear grade-graphite domain. The main objective is to understand how the stress builds up around the boundary of the void once they get closer to each other. This provides much insight into understanding the fracture behavior for the two-particle coalescence case studied in the

following subsection. Figures 44 and 45 illustrate how the stress gets higher at the void inner boundaries once they get closer. Surprisingly, the stresses drop on the voids' internal boundaries and increase on their outer edges once they get touched (the onset of coalescence). Hence, the expectation of the cracking nucleation site will be changed from inner to outer boundaries once the voids coalesce. In contrast, the higher stresses, consequently, the expected cracking nucleation site, will be preferred at the voids' internal boundaries when they get closer to each other.

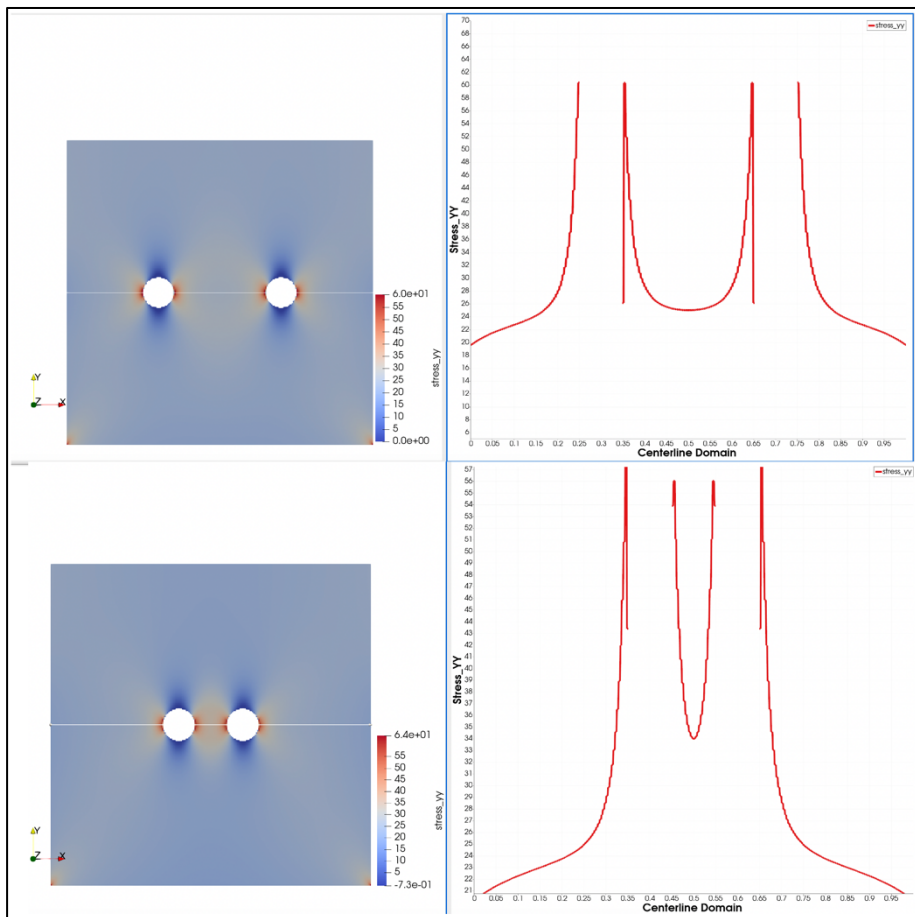


Figure 44 Snapshots of a two-particles (voids) nuclear-grade graphite system show how the stress builds up on the voids' inner and outer boundaries when they get closer in distance.

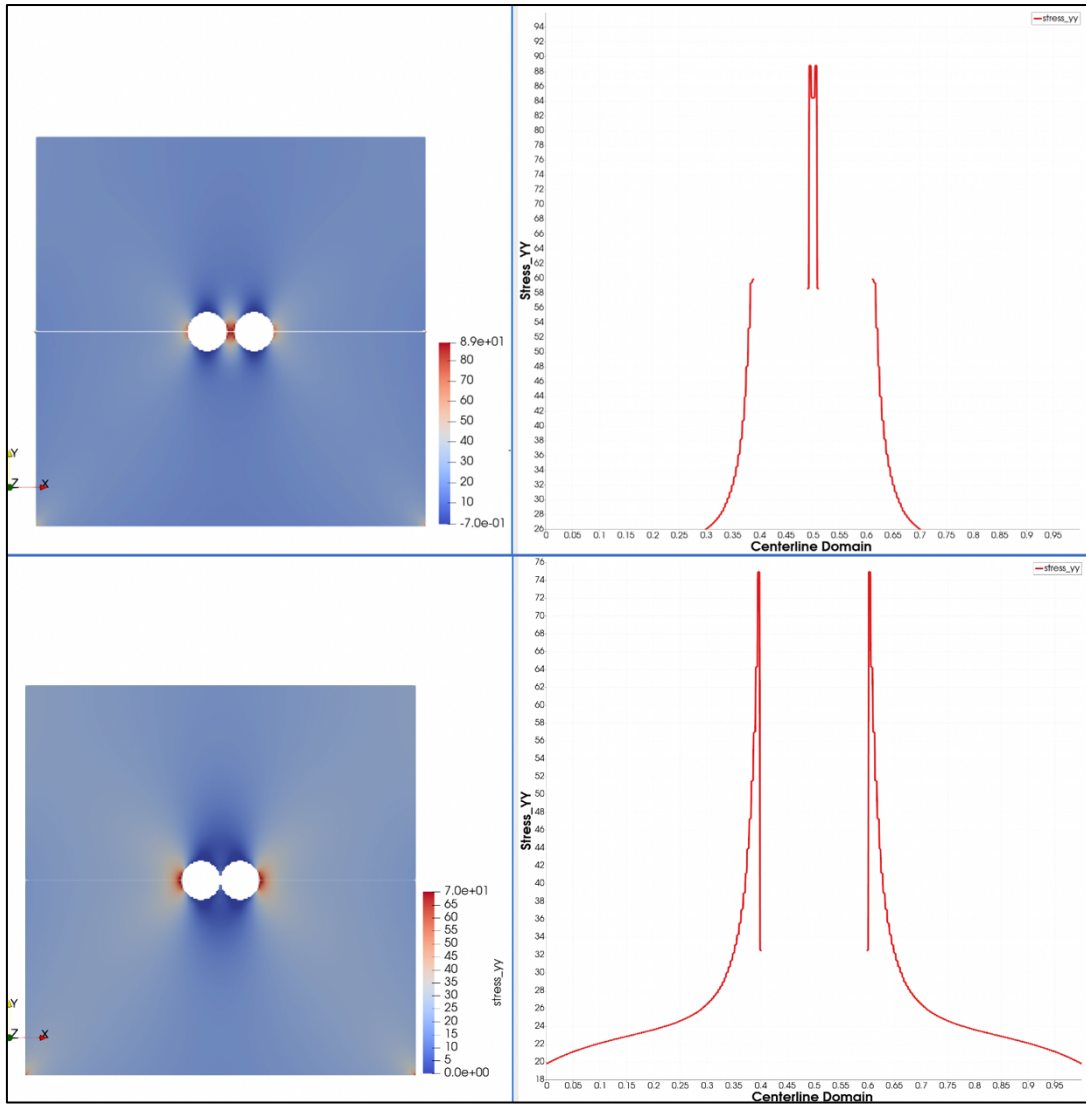


Figure 45 Snapshots of a two-particles (voids) nuclear-grade graphite system show how the stress builds up on the voids' inner and outer boundaries when they get touched (coalescence).

4.4.2 Simulating the concurrent formation of cracks and microstructure evolution

Different sizes of two particles (voids) are brought closer to each other in a middle of a nuclear-grade graphite domain. With an applied load in YY-direction, our Novel Model could capture both: The voids' coalescence and the stresses building up concurrently, as seen in Figure 46. As we concluded in the two-voids static analysis, the stresses increased on the void outer surface once they got in touch.

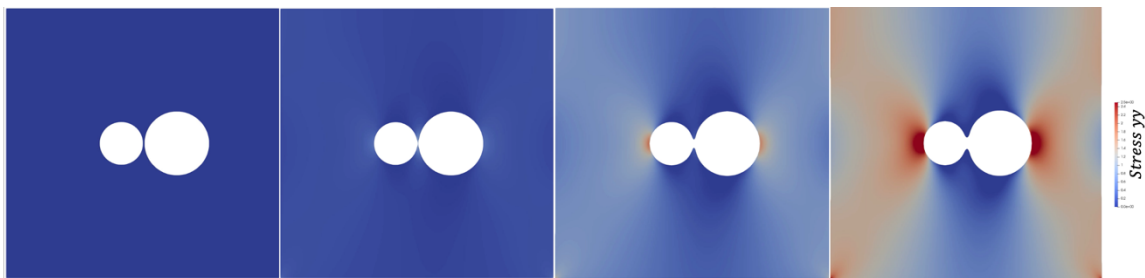


Figure 46 Two voids coalescence and the stresses building up concurrently, watch the evolutions from left to right.

We chose two voids with different radii to show the model's capabilities in capturing the crack nucleation at various preferable sites concurrently with the void coalescence. The model could successfully capture cracking initiation at the higher curvature (smaller radius) first, along with the related stress behavior, see Figure 47. The stress-strain response under uniaxial loading for this investigation system is presented in Figure 48. The crack starts at the higher curvature (left domain side), and the Damage intensification remains confined within right-side regions. This leads to a smooth drop in the system's overall stresses. A complete failure occurs once the crack starts at the lower curvature (domain right side). Hence a sharp reduction in the overall stresses; see the snapshots in Figure 48 for better illustration.

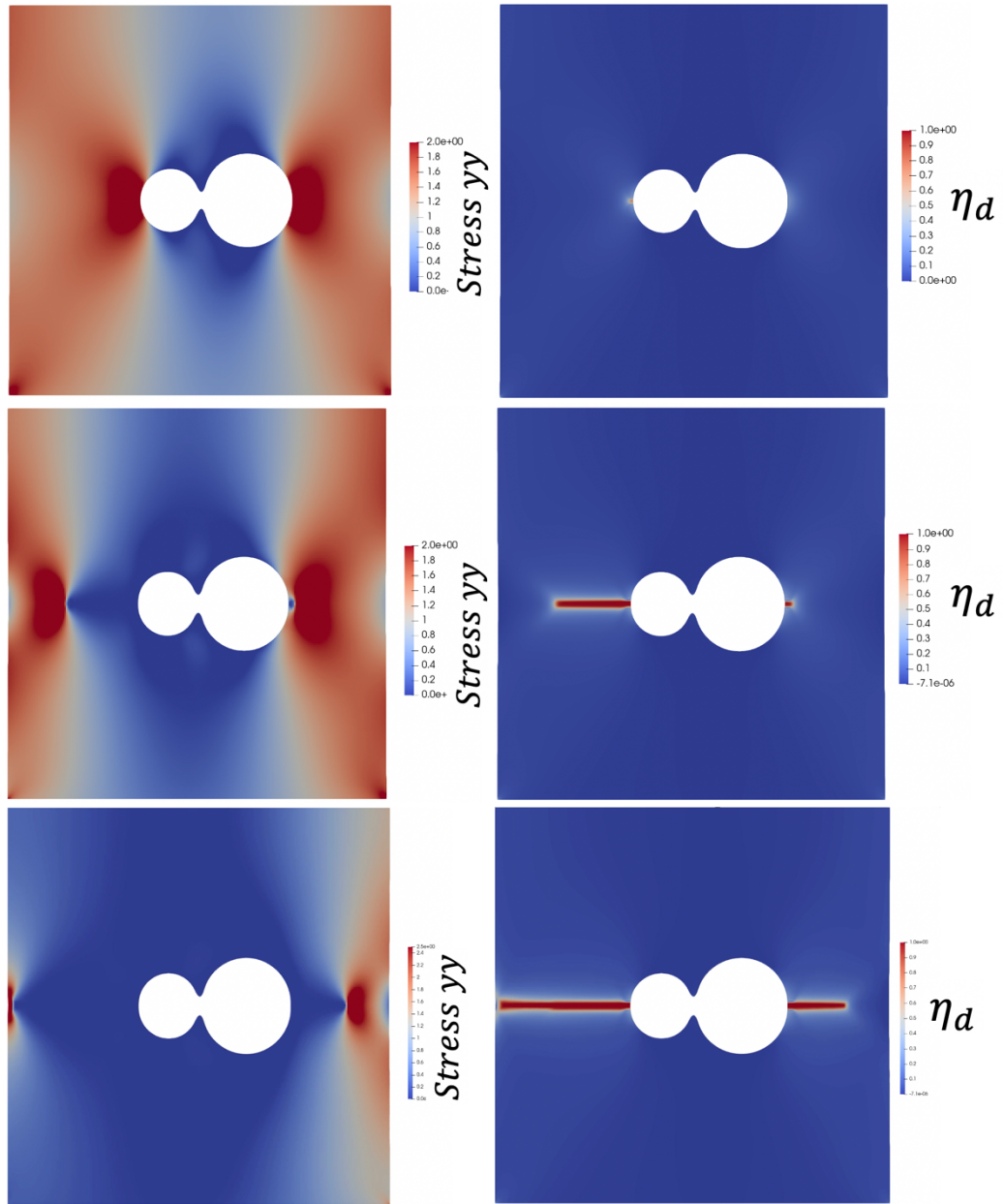


Figure 47 Snapshots illustrate the model's capabilities in capturing the preferable cracking nucleation sites without any ad hoc and the stress distribution concurrently with the voids coalescence.

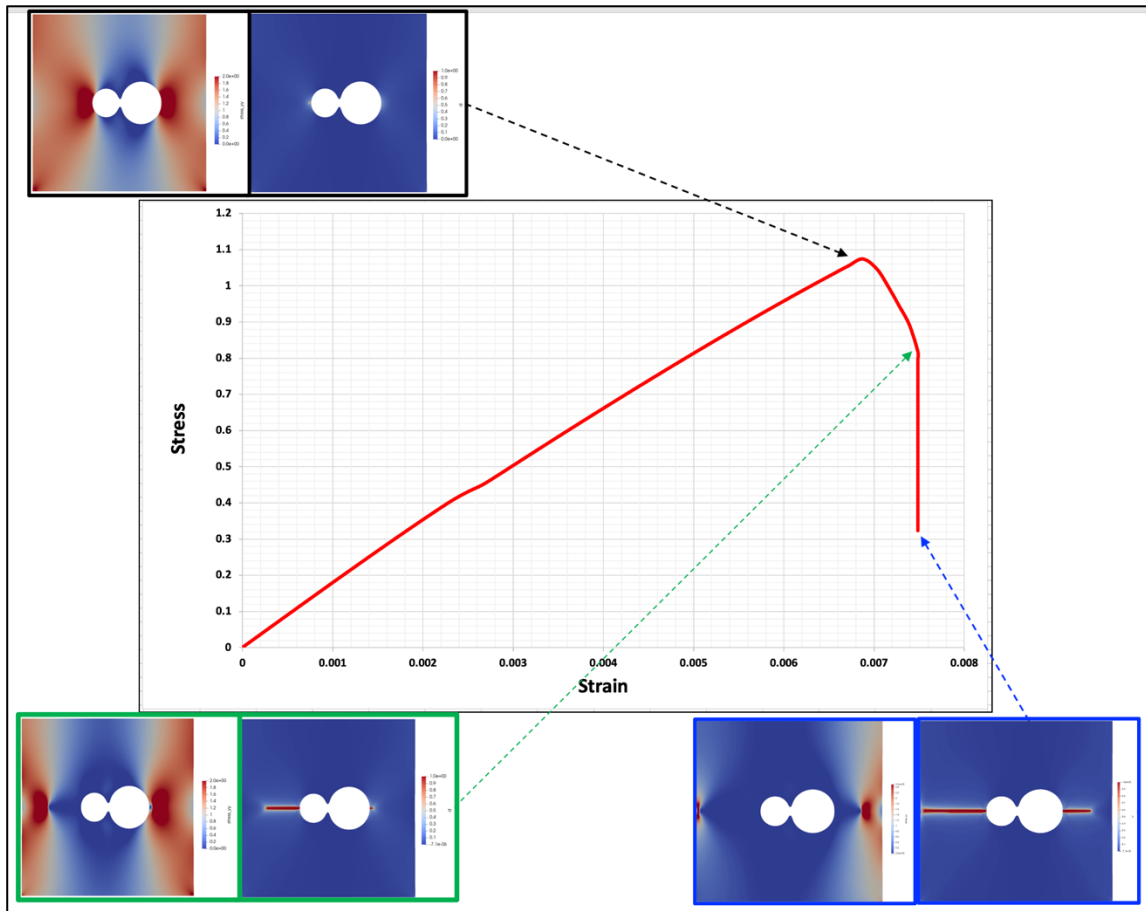


Figure 48 The stress-strain response under uniaxial loading with a magnified snapshot at the onset of unloading (i.e., cracking) points.

This work's Novel phase-field modeling of fracture simulated cracks' initiation rate, size, shape, thickness, and morphology, and the spatial stress formations, distributions, and evolutions throughout the whole system domain without any ad-hoc or prior assumptions. Moreover, our new technique allows studying microstructure evolution and its influences on the cracking and the materials' mechanical properties change.

4.5 Evaluation of fracture behaviors in porous materials: Multi-particles case

The porosity and pore size significantly influence the nuclear-grade graphite fracture. These characterization factors include porosity shape, size, distributions, filler size and density, etc. In INL work [23], the authors studied the effect of pore size and distributions to evaluate the fracture response of nuclear-grade graphite (H-451). To perform this study, they ran various Representative Elementary Volume (RVE) cases. A typical RVE for H-451 and the utilized model parameters are shown in Figure 49, in which the minimum allowed geometrical pore radius is 20 microns.

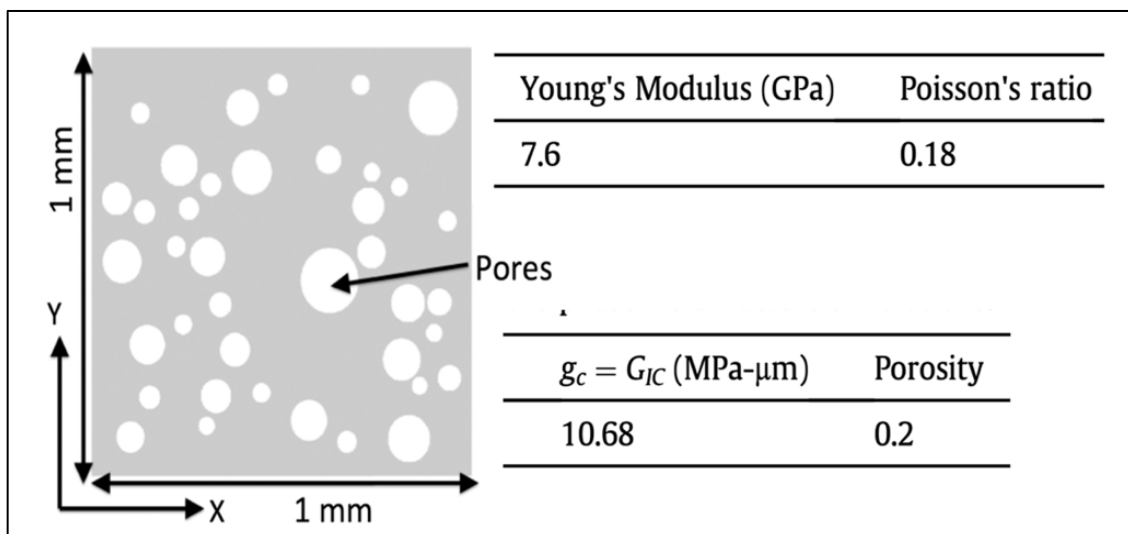


Figure 49 A typical representative volume element along with the utilized model parameter to simulate the H-451, nuclear-grade graphite [23].

To compare our model results with the INL work qualitatively, we used similar model parameters and porosity microstructures. The qualitative comparisons were displayed in figures 50 and 51, which reveals sufficient similarities. The origin of the minor differences is due to the slight difference in model parameters and the porosity

microstructure. In both results (our model and the INL work), we could observe that the bigger pores have a higher probability of initiating micro-cracks. Also, the cracks will propagate in regions with high porous density.

Next, we will use the TRISO-buffer layer mechanical properties obtained by the atomistic and experimental measurements to feed our novel model formulations to quantify the porosity microstructure effects on the stochastic fracture formation and evaluation in the buffer layer.

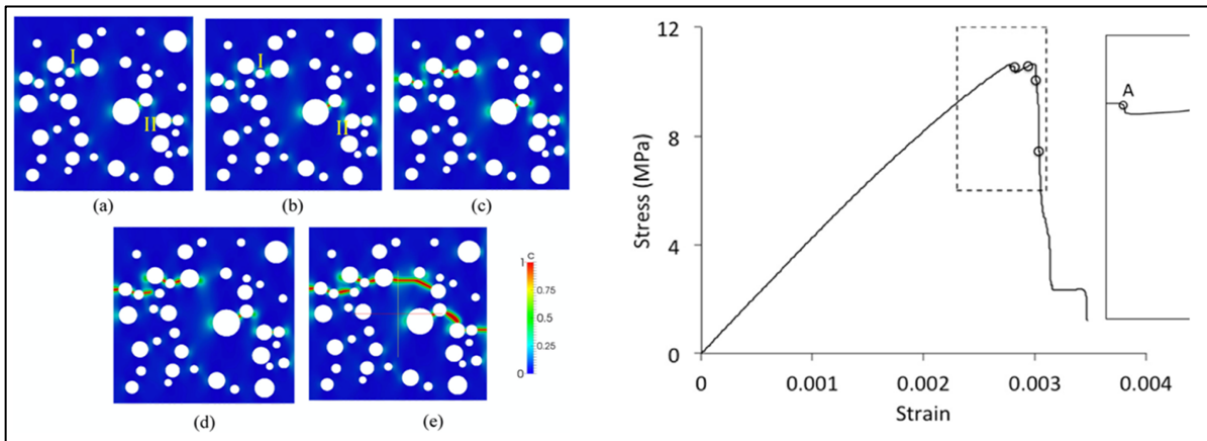


Figure 50 work by P. Chakraborty et al., [23] . The left side is the damaged configurations while the right side is the stress-strain response under uniaxial loading of the representative volume element.

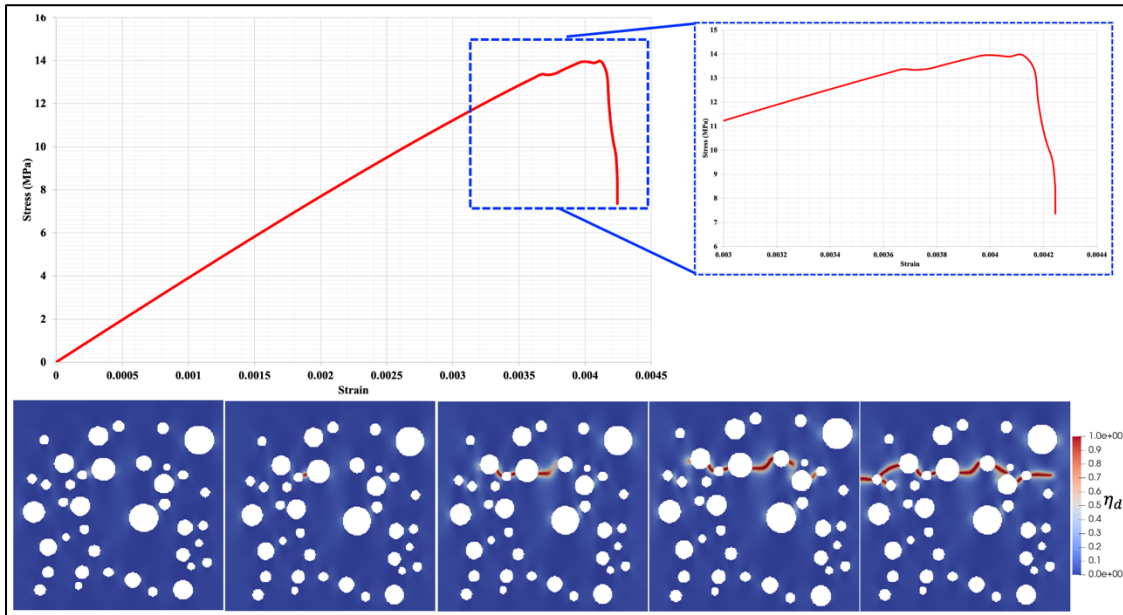


Figure 51 Snapshots of the cracking initiation and evolutions in a porosity microstructure similar to the INL investigated case [23], see Figure 50. Once a crack starts, the Damage intensification remains confined within the damage regions resulting in an observed recovery in strength values as seen in the zoomed-in part of the stress-strain curve. Then the stress dropped sharply once the microstructure fully cracked, see the last snapshot on the right.

CHAPTER V

CONCLUSIONS

This work advances the fundamental understanding of nuclear fuel behavior under normal and transient conditions and provides a predictive modeling tool for deriving physics-based criteria for the fracture behavior of the current and the new nuclear fuel designs. We introduced a new combined experimental and computational approach to investigate thermal shock-induced fracture in UO_2 pellets. First, we briefly reviewed the experimental method to promote thermal fracture in the UO_2 . Second, the experimental data was utilized to parameterize and validate a Multiphysics model of fracture. In contrast to other fracture modeling techniques, our model that employs a phase-field fracture approach can predict the crack nucleation site, growth rate, crack path, size, and morphology given the values of the fracture properties of the material of interest. The energy release rate, \mathcal{G}_c (or equivalently fracture toughness) is microstructure- and size-dependent, and its value is unknown for UO_2 and other nuclear fuels. Its value is difficult to estimate both from experiments and first-principles simulations. Lower-scale, first-principles simulations are limited to small sizes and cannot evaluate the actual value for a realistic microstructure. Even experimental studies cannot extract this number directly. They usually utilize either finite-element simulations or employ a few limiting analytical expressions from the linear elastic fracture mechanics to derive this value from their data [44 – 45]. Here, a set of \mathcal{G}_c and contract area were able to capture the overall fracture trend of the corresponding experimental data. In fact, we believe that the phase-field

fracture employed here presents a new method for calculating the energy release rate of \mathcal{G}_c /fracture toughness.

The model results were obtained by solving the coupled equations using the finite element method implemented in MOOSE. The model predictions demonstrate its capability to simulate the formation and the following growth of the cracks. The model was able to reproduce the experimental temperature profile (see Figure 34), similar crack morphologies (see Figure 37), the expected stresses of formation and evolution (see Figure 38), and the behaviors of elastic and fracture energies predicted by Griffith's [5] (see Figure 39). The importance of the UO_2 fuel pellets microstructure (e.g., porosity) on the overall kinetics of the fracture formation and evolution were examined qualitatively.

Furthermore, we introduced a novel phase-field fracture model that has been verified using UO_2 and nuclear grade graphite data to capture the concurrent microstructure evolution and fracture formation and propagations. Studying the competition between microstructure evolution and cracking is crucial to understanding the stochastic tearing behavior in nuclear fuels. For the first time, we employed a multi-set order parameters to describe the concurrent crack formation and propagation along with microstructure evolution including second phase particles formation and evolution (e.g., coalescence). The verified model was first applied to study the stress distribution around voids boundaries in a static two-particle domain, then applied to a heterogeneous nuclear-grade graphite system to determine the effect of void coalescence on the fracture behaviors that changes the effective toughness of the materials; hence influences the mechanical properties. This new technique allows studying microstructure evolutions and their

influences on fracture behavior and validated against previous INL work [23]. The presented results are very promising, and we are planning further investigations and parametric studies to quantify the uncertainty.

5.1 Future Directions

In the next stage, a 3D experimental characterization and atomistic scale modeling will be utilized to inform and further validating our model. The model will be adopted to account for the change of the TRISO buffer layer's elastic and fracture properties. A more detailed investigation of the effect of porosity microstructure on macroscopic cracks formation and evolution will be the subject of future studies. Furthermore, the change of elastic and fracture properties with microstructure, temperature, and irradiation conditions will also be accounted for in upcoming investigations. This can be accomplished via coupling our novel model with the phase-field models of irradiation-induced microstructure evolution [12, 15].

CHAPTER VI WORKS CITED

- [1] H. Kobayashi and H. Onoue, "Brittle fracture of liberty ships," Failure Knowledge Database, Oregon State, USA, 1943.
- [2] N. Zimmermann and P. Hao Wang, "A review of failure modes and fracture analysis of aircraft composite materials," *Engineering Failure Analysis*, vol. 115, p. 104692, 2020.
- [3] B. Cotterell, "The past, present, and future of fracture mechanics," *Engineering Fracture Mechanics*, vol. 96, no. 5, pp. 533-553, 2002.
- [4] C. E. Inglis, "Stresses in a plate due to the presence of cracks and sharp corners," *Institution of Naval Architects (London)*, vol. 55, pp. 219-230, 1913.
- [5] A. A. Griffith, "The phenomena of rupture and flow in solids," *PHILOSOPHICAL TRANSACTIONS OF THE ROYAL SOCIETY A MATHEMATICAL, PHYSICAL AND ENGINEERING SCIENCES*, pp. 163-198, 1921.
- [6] G. R. Irwin, "Fracture dynamics," in *ASM Symposium on Fracturing of Metals*, Cleveland (Oh), 1948.
- [7] J. Williams, "Introduction to linear elastic fracture mechanics," *European Structural Integrity Society*, vol. 28, pp. 3-10, 2001.
- [8] J. Newman Jr. and I. Raju, "An empirical stress-intensity factor equation for the surface crack," *Engineering Fracture Mechanics*, vol. 15, no. 1-2, pp. 185-192, 1981.
- [9] R. J. NUISMER, "An energy release rate criterion for mixed mode fracture," *International Journal of Fracture*, vol. 11, pp. 245-250, 1975.
- [10] N. Adams, S. Garwood and J. Robinson, "Elasto-plastic fracture mechanics applied to the safety assessment of nuclear power stations," *International Journal of Pressure Vessels and Piping*, vol. 9, no. 1, pp. 27-39, 1981.

- [11] K. Chung and M.-G. Lee, *Basics of Continuum Plasticity*, Seoul, South Korea: Springer, 2018.
- [12] M. G. Abdoelatef, F. Badry, D. Schwen, C. Permann, Y. Zhang and K. Ahmed, "Mesoscale Modeling of High Burn-Up Structure Formation and Evolution in UO₂," *The Journal of The Minerals, Metals & Materials Society (JOM)*, vol. 71, p. 4817–4828, 2019.
- [13] M. P. Short and S. Yip, "Materials aging at the mesoscale: Kinetics of thermal, stress, radiation activations," *Current Opinion in Solid State and Materials Science*, vol. 19, pp. 245-252, 2015.
- [14] B. B. a. P. W. Nele Moelans, "An introduction to phase-field modeling of microstructure evolution," *Calphad*, vol. 32, no. 2, pp. 268-294, 2008.
- [15] K. Ahmed and A. El-Azab, "Phase-Field Modeling of Microstructure Evolution in Nuclear Materials," in *Handbook of Materials Modeling*, Cham., Springer, , 2020, pp. 2313-2334.
- [16] L.-Q. Chen, "Phase-Field Models for Microstructure Evolution," *Annual Review of Materials Research*, vol. 32, pp. 133-140, 2002.
- [17] R. A. Meserve, , "Global warming and nuclear power," *American Association for the Advancement of Science*, vol. 303, no. 5657, 2004.
- [18] P. L. Joskow, , "The future of nuclear power in the United States : economic and regulatory challenges," MIT Center for Energy and Environmental Policy Research, Massachusetts, 2006.
- [19] L. D. McClenny, M. I. Butt, M. G. Abdoelatef, M. J. Pate, K. L. Yee, R. Harikrishnan, D. Perez-Nunez, W. Jiang, L. H. Ortega, S. M. McDeavitt and K. Ahmed, "Experimentally validated Multiphysics modeling of fracture induced by thermal shocks in Sintered UO₂ Pellets," *Journal of Nuclear Materials*, vol. 565, p. 153719, 2022.
- [20] S. A. Ploger, P. A. Demkowicz, J. D. Hunn and J. S. Kehn, "Microscopic analysis of irradiated AGR-1 coated particle fuel compacts," *Nuclear Engineering and Design*, vol. 271, pp. 221-230, 2014.

- [21] J. D. Hunn, C. A. Baldwin, T. J. Gerczak, F. C. Montgomery, R. N. Morris, C. M. Silva, P. A. Demkowicz, J. M. Harp and S. A. Ploger, "Detection and analysis of particles with failed SiC in AGR-1 fuel compacts," *Nuclear Engineering and Design*, vol. 306, pp. 36-46, 2016.
- [22] F. Rice, J. Stempien and P. Demkowicz, "Ceramography of irradiated TRISO fuel from the AGR-2 experiment," *Nuclear Engineering and Design*, vol. 329, pp. 73-81, 2018.
- [23] P. Chakraborty, P. Sabharwall and M. C. Carroll, "A phase-field approach to model multi-axial and microstructure dependent fracture in nuclear grade graphite," *Journal of Nuclear Materials*, vol. 475, pp. 200-208, 2016.
- [24] W. Jiang, T. Hu, L. K. Aagesen and Y. Zhang, "Three-dimensional phase-field modeling of porosity dependent intergranular fracture in UO₂," *Computational Materials Science*, vol. 171, p. 109269, 2020.
- [25] L. Zhao, D.-h. Han, Q. Yao, F. Yan and M. Nasser, "Modeling the effect of pore and crack interactions on the effective elastic properties of fractured porous rocks," *SEG Technical Program Expanded Abstracts*, pp. 2900-2904, 2013.
- [26] J. A. Hudson, E. Liu and S. Crampin, "The mechanical properties of materials with interconnected cracks and pores," *Geophysical Journal International*, vol. 124, p. 105–112, 1996.
- [27] H. Zhang , H. Toda, M. Kobayashi, T. Kobayashi, D. Sugiyama, N. Kuroda and K. Uesugi, "Three-Dimensional Visualization of the Interaction between Fatigue Crack and Micropores in an Aluminum Alloy Using Synchrotron X-Ray Microtomography," *Metallurgical and Materials Transactions* , vol. 38, p. 1774–1785 , 2007.
- [28] C. Miehe, F. Welschinger and M. Hofacker, "Thermodynamically consistent phase-field models of fracture: Variational principles and multi-field FE implementations," *INTERNATIONAL JOURNAL FOR NUMERICAL METHODS IN ENGINEERING*, vol. 83, pp. 1273-1311, 2010.
- [29] C. Miehe, M. Hofacker and F. Welschinger, "A phase field model for rate-independent crack propagation: Robust algorithmic implementation based on

- operator splits," *Computer Methods in Applied Mechanics and Engineering*, vol. 199, pp. 45-48, 2010.
- [30] I. Babuška and J. Melenk, "The partition of unity method," *INTERNATIONAL JOURNAL FOR NUMERICAL METHODS IN ENGINEERING*, vol. 40, pp. 727-758, 1997.
- [31] N. Moës, J. Dolbow and T. Belytschko, "A finite element method for crack growth without remeshing," *INTERNATIONAL JOURNAL FOR NUMERICAL METHODS IN ENGINEERING*, vol. 46, pp. 131-150, 1999.
- [32] M. Kamaya, Y. Kawamura and T. Kitamura, "Three-dimensional local stress analysis on grain boundaries in polycrystalline material," *International Journal of Solids and Structures*, vol. 44, no. 10, pp. 3267-3277, 2007.
- [33] M. Kamaya and M. Itakura, "Simulation for intergranular stress corrosion cracking based on a three-dimensional polycrystalline model," *Engineering Fracture Mechanics*, vol. 76, no. 3, pp. 386-401, 2009.
- [34] N. Sukumar, D. Srolovitz, T. J. Baker and J. H. Prévost, "Brittle fracture in polycrystalline microstructures with the extended finite element method," *International Journal for Numerical Methods in Engineering*, vol. 56, no. 14, pp. 2015-2037, 2003.
- [35] A. Needleman, "Micromechanical modelling of interfacial decohesion," *Ultramicroscopy*, vol. 40, no. 3, pp. 203-214, 1992.
- [36] M. Ortiz and A. Pandolfi, "Finite-deformation irreversible cohesive elements for three-dimensional crack-propagation analysis," *International Journal for Numerical Methods in Engineering*, vol. 44, no. 9, pp. 1267-1282, 1999.
- [37] A. Karma, D. A. Kessler and H. Levine, "Phase-field model of mode III dynamic fracture," *PHYSICAL REVIEW LETTERS*, vol. 87, no. 4, p. 045002, 2001.
- [38] A. Karma and A. E. Lobkovsky, "Unsteady Crack Motion and Branching in a Phase-Field Model of Brittle Fracture," *PHYSICAL REVIEW LETTERS*, vol. 92, p. 245510, 2004.

- [39] H. Henry and H. Levine, "Dynamic instabilities of fracture under biaxial strain using a phase field model," *PHYSICAL REVIEW LETTERS*, vol. 93, no. 10, p. 105504, 2004.
- [40] M. j. Borden, C. V. Verhoosel, M. A. Scott, T. J. Hughes and L. Chad M., "A phase-field description of dynamic brittle fracture," *Computer Methods in Applied Mechanics and Engineering*, Vols. 217-220, pp. 77-95, 2012.
- [41] G. A. Francfort and J.-J. Marigo, "Revisiting brittle fracture as an energy minimization problem," *Journal of the Mechanics and Physics of Solids*, vol. 46, no. 8, pp. 1319-1342, 1998.
- [42] B. Bourdin, G. A. Francfort and J.-J. Marigo, "Numerical experiments in revisited brittle fracture," *Journal of the Mechanics and Physics of Solids*, vol. 48, no. 4, pp. 797-826, 2000.
- [43] S. Zhang, W. Jiang and M. R. Tonks, "A new phase field fracture model for brittle materials that accounts for elastic anisotropy," *Computer Methods in Applied Mechanics and Engineering*, vol. 358, p. 112643, 2020.
- [44] A. Doitrand, R. Henry, I. Zacharie-Aubrun, J.-M. Gatt and S. Meille, "UO₂ micron scale specimen fracture: Parameter identification and influence of porosities," *Theoretical and Applied Fracture Mechanics*, vol. 108, p. 102665, 2020.
- [45] R. Henry, I. Zacharie-Aubrun, T. Blay, S. Chalal, J.-M. Gatt, C. Langlois and S. Meille, "Fracture properties of an irradiated PWR UO₂ fuel evaluated by micro-cantilever bending tests," *Journal of Nuclear Materials*, vol. 538, p. 152209, 2020.
- [46] I. Zacharie-Aubrun, R. Henry, T. Blay, L. Brunaud, J. Gatt, J. Noirot and S. Meille, "Effects of irradiation on mechanical properties of nuclear UO₂ fuels evaluated by Vickers indentation at room temperature," *Journal of Nuclear Materials*, vol. 547, p. 152821, 2021.
- [47] S. Patnaik, D. Lopes, B. Spencer, T. Besmann, E. Roberts and T. Knight, "Evaluation of ceria as a surrogate material for UO₂ in experiments on fuel cracking driven by resistive heating," *Nuclear Engineering and Design*, vol. 384, p. 111482, 2021.

- [48] T. Anderson, *FRACTURE MECHANICS Fundamentals and Applications*, New York: Taylor & Francis, 2017.
- [49] W. Hoffelner, "Irradiation Damage," in *Materials for Nuclear Plants*, London, Springer, 2013, pp. 4471-2915.
- [50] M. Short, "22.01 Introduction to Nuclear Engineering and Ionizing Radiation.," Massachusetts Institute of Technology: MIT OpenCourse, Massachusetts, 2016.
- [51] W. S. GARY , *Fundamentals of Radiation Materials Science: Metals and Alloys*, New York: Springer Berlin, 2017.
- [52] J.-Y. Wu, V. P. Nguyen, C. T. Nguyen, D. Sutula, S. Sinaie and S. Bordas, "Phase-field modelling of fracture," *Advances in Applied Mechanics*, vol. 53, pp. 1-183, 2020.
- [53] V. I. Levitas, H. Jafarzadeh, G. H. Farrahi and M. Javanbakht, "Thermodynamically consistent and scale-dependent phase Field approach for crack propagation allowing for surface stresses," *International Journal of Plasticity*, vol. 111, pp. 1-35, 2018.
- [54] E. Tanné, T. Li, B. Bourdin, J.-J. Marigo and C. Maurini, "Crack nucleation in variational phase-field models of brittle fracture," *Journal of the Mechanics and Physics of Solids*, vol. 110, pp. 80-99, 2018.
- [55] F. Badry, R. Brito, M. G. Abdoelatef, S. McDeavitt and K. Ahmed, "An Experimentally Validated Mesoscale Model of Thermal Conductivity of a UO₂ and BeO Composite Nuclear Fuel," *The Journal of The Minerals, Metals & Materials Society (JOM)*, vol. 71, p. 4829–4838, 2019.
- [56] M. G. Abdoelatef, "MESOSCALE MODELING OF GRAIN REFINEMENT IN SOLIDS," Texas A&M University., College Station, 2019.
- [57] B. Spencer, N. Woolstenhulme, L. Emerson, J. Yeh, D. Imholte, C. Hill, D. Chapman, C. Jensen, T. Knight, S. Patnaik, S. McDeavitt, L. Ortega, D. Perez-Nunez and H. Ban, "Separate-effects validation experiments for models of fracture in ceramic nuclear fuel," Idaho National Laboratory (INL), Idaho, 2019.

- [58] L. Ortega, K. Yee, D. Perez-Nunez, S. McDeavitt, C. Steinman, R. Schultz, M. Dunzik-Gougar and B. Spencer, "Thermal-shock experiments for separate-effects validation of UO₂ fuel fracture models," *Journal of Nuclear Materials*, vol. To be Published in, 2022.
- [59] J. D. Hales, R. L. Williamson, S. R. Novascone, D. M. Perez, B. W. Spencer and G. Pastore, "Multidimensional multiphysics simulation of TRISO particle fuel," *Journal of Nuclear Materials*, vol. 443, p. 531–543, 2013.
- [60] C. W. Forsberg, P. F. Peterson and P. S. Pickard, "Molten-Salt-Cooled Advanced High-Temperature Reactor for Production of Hydrogen and Electricity," *Nuclear Technology*, vol. 144, pp. 289-302, 2003.
- [61] C. Tang, J. Zhu, Y. Tang, Y. Zou, J. Li and X. Ni, "Design and manufacture of the fuel element for the 10 MW high temperature gas-cooled reactor," *Nuclear Engineering and Design*, vol. 218, pp. 91-102, 2002.
- [62] I. Dulera and R. Sinha, "High temperature reactors," *Journal of Nuclear Materials*, vol. 383, pp. 183-188, 2008.
- [63] M. Price, "The Dragon Project origins, achievements and legacies," *Nuclear Engineering and Design*, pp. 60-68, 2012.
- [64] I. Steinbach, "Phase-field models in materials science," *MODELLING AND SIMULATION IN MATERIALS SCIENCE AND ENGINEERING*, vol. 17, 2009.
- [65] S. S. a. M. Haataja, "Recrystallization kinetics A coupled coarse-grained dislocation density and phase-field approach," *PHYSICAL REVIEW*, vol. 76, 2007.
- [66] B. Z. a. M. Militzer, "3D phase field modelling of recrystallization in a low-carbon steel," *Modelling Simul. Mater. Sci. Eng.*, vol. 20, p. 17, 2012.
- [67] B. G. M. L. L.-Q. C. Yanzhou Ji, "Phase-field modeling of θ' precipitation kinetics in 319 aluminum alloys," *Computational Materials Science*, vol. 151, pp. 84-94, 2018.

- [68] Z. D. Y. W. K. S. J. G. Y. W. W.J. Zheng, "Phase field investigation of dendrite growth in the welding pool of aluminum alloy 2A14 under transient conditions," *Computational Materials Science*, vol. 82, pp. 525-530, 2014.
- [69] Z.-G. M. a. A. M. Y. Linyun Liang, "Fission-induced recrystallization effect on intergranular bubble-driven swelling in U-Mo fuel," *Computational Materials Science*, vol. 138, pp. 16-26, 2017.
- [70] M. G. Abdoelatef, F. Badry, D. Schwen, C. Permann, Y. Zhang and K. Ahmed, "Mesoscale Modeling of High Burn-Up Structure Formation and Evolution in UO₂," *The Journal of The Minerals, Metals & Materials Society (TMS)*, vol. 71, p. 4817-4828, 2019.
- [71] Z.-G. M. Y. S. K. B. Y. G. H. M. A. a. A. M. Y. Linyun Liang, "Mesoscale model for fission-induced recrystallization in U-7Mo alloy," *Computational Materials Science*, vol. 124, pp. 228-237, 2016.
- [72] W. Li and K. Shirvan, "Multiphysics phase-field modeling of quasi-static cracking in uranium ceramic nuclear fuel," *Ceramics International*, pp. 793-810, 2021.
- [73] D. B. Mumford and J. Shah, "Optimal Approximations by Piecewise Smooth Functions and Associated Variational Problems," *Communications on Pure and Applied Mathematics*, vol. 42, no. 5, pp. 577-685, 1989.
- [74] L. Ambrosio and V. M. Tortorelli, "Approximation of functional depending on jumps by elliptic functional via Γ -convergence," *Communications on Pure and Applied Mathematics*, vol. 43, no. 8, pp. 999-1036, 1990.
- [75] H. Amor, J.-J. Marigo and C. Maurini, "Regularized formulation of the variational brittle fracture with unilateral contact: Numerical experiments," *Journal of the Mechanics and Physics of Solids*, vol. 57, no. 8, pp. 1209-1229, 2009.
- [76] J. D. Clayton and J. Knap, "Phase field modeling of directional fracture in anisotropic polycrystals," *Computational Materials Science*, vol. 98, pp. 158-169, 2015.

- [77] S. Teichtmeister, D. Kienle, F. Aldakheel and M.-A. Keip, "Phase field modeling of fracture in anisotropic brittle solids," *International Journal of Non-Linear Mechanics*, vol. 97, pp. 1-21, 2017.
- [78] I. N. Lab, "MOOSE: Multiphysics Object Oriented Simulation Environment," Idaho National Lab, 2014. [Online]. Available: <https://mooseframework.inl.gov/>.
- [79] M. Gururajan and T. Abinandanan, "Phase field study of precipitate rafting under a uniaxial stress," *Acta Materialia*, vol. 55, no. 15, pp. 5015-5026, 2007.
- [80] N. Zhou, C. Shen, M. Mills and Y. Wang, "Phase field modeling of channel dislocation activity and γ' rafting in single crystal Ni–Al," *Acta Materialia*, vol. 55, no. 16, pp. 5369-5381, 2007.
- [81] R. Mukherjee, T. Abinandanan and M. Gururajan, "Phase field study of precipitate growth: Effect of misfit strain and interface curvature," *Acta Materialia*, vol. 57, no. 13, pp. 3947-3954, 2009.
- [82] L. Thuinet, A. D. Backer and A. Legris, "Phase-field modeling of precipitate evolution dynamics in elastically inhomogeneous low-symmetry systems: Application to hydride precipitation in Zr," *Acta Materialia*, vol. 60, no. 13-14, pp. 5311-5321, 2012.
- [83] C. Shen and Y. Wang, "Coherent Precipitation — Phase Field Method," in *Handbook of Materials Modeling*, Dordrecht, Springer, 2005.
- [84] J. Han, S. Matsubara, S. Moriguchi, M. Kaliske and K. Terada, "Crack phase-field model equipped with plastic driving force and degrading fracture toughness for ductile fracture simulation," *Computational Mechanics*, 2021.
- [85] Y. Yu, X. Zheng, P. Li, Z. Zhang and J. Xiao, "Evaluation of mechanical and energy properties for the phase field modeling of failure," Northwestern Polytechnical University, China , 2021.
- [86] J. W. Cahn, "On spinodal decomposition," *Acta Metallurgica*, vol. 9, no. 9, pp. 795-801, 1961.

- [87] N. Moelans, "A quantitative and thermodynamically consistent phase-field interpolation function for multi-phase systems," *Acta Materialia*, vol. 59, no. 3, pp. 1077-1086, 2011.
- [88] A. Ozturk, M. Gencturk and K. Ahmed, "Surface and Size Effects on the Behaviors of Point Defects in Irradiated Crystalline Solids," *Frontiers Materials*, 2021.
- [89] K. A. a. A. El-Azab, "Phase-field modeling of microstructure evolution in nuclear materials," in *Handbook of Materials Modeling*, Cham, Springer, 2018.
- [90] N. P. a. K. Elder, *Phase-Field Methods in Materials Science and Engineering*, Weinheim, Germany: Wiley-VCH, 2010.
- [91] N. M. a. B. B. P. Wollants, "Quantitative analysis of grain boundary properties in a generalized phase field model for grain growth in anisotropic systems," *PHYSICAL REVIEW*, vol. 78, no. 2, p. 024113, 2008.
- [92] J. P. T. A. ., a. A.-A. Karim Ahmed, "Phase field simulation of grain growth in porous uranium dioxide," *Journal of Nuclear Materials*, vol. 446, no. 13, pp. 90-99, 2014.
- [93] C. A. Y. A. S. T. A. a. A. E.-A. K Ahmed, "Phase field modeling of the effect of porosity on grain growth kinetics in polycrystalline ceramics," *Modelling and Simulation in Materials Science and Engineering*, vol. 21, p. 23, 2013.
- [94] T. Anderson, *FRACTURE MECHANICS Fundamentals and Applications*, New York, USA: Taylor and Francis Group, 2005.
- [95] H. Tada, P. Paris and G. Irwin, *The Stress Analysis of Cracks Handbook*, Louis, MO: Paris Productions, 1985.
- [96] K. Govers, S. Lemehov, M. Hou and M. Verwerft, "Comparison of interatomic potentials for UO₂.Part I: Static calculations," *Journal of Nuclear Materials* , vol. 366, no. 1-2, pp. 161-177, 2007.
- [97] C. Miehe, F. Welschinger and M. Hofacker, "Thermodynamically consistent phase-field models of fracture: Variational principles and multi-field FE

implementations," *International Journal for Numerical Methods in Engineering*, no. 10, pp. 1273-1311, 2010.

[98] M. OGUMA, "Microstructure Effects on Fracture Strength of UO₂ Fuel Pellets," *Journal of Nuclear Science and Technology*, vol. 19, no. 12, 1982.